Inclusive Jet Cross Sections in Neutral Current Deep Inelastic Scattering in the Breit Frame at ZEUS

Inauguraldissertation

zur Erlangung des Doktorgrades

der Fakultät für Physik

der

Albert-Ludwigs-Universität

Freiburg im Breisgau

vorgelegt von

Henning Raach

geb. in Saarlouis

Juni 2001

Contents

Introduction **1**

1 The ZEUS Experiment at HERA **3**
1.1 The Storage Ring HERA . . . 3
1.2 The ZEUS Detector . . . 5
1.2.1 Overview . . . 5
1.2.2 The Central Tracking Detector (CTD) . . . 7
1.2.3 The Uranium Calorimeter . . . 9
1.2.4 Trigger . . . 12

2 Kinematic Variables **14**
2.1 Definition . . . 14
2.2 Reconstruction . . . 16

3 Theory **19**
3.1 QCD and DIS . . . 19
3.1.1 Fundamentals of QCD . . . 19
3.1.2 The Renormalization Scale . . . 20
3.1.3 Structure Functions . . . 22
3.1.4 The Factorization Scale . . . 24
3.2 Jets . . . 26
3.3 The Breit Frame . . . 30
3.4 The Azimuthal Asymmetry . . . 31

4 Monte Carlo Simulation **34**
4.1 Leading-order MC Simulation . . . 35
4.1.1 The Parton Shower Model . . . 35
4.1.2 The Colour Dipole Model . . . 37
4.1.3 String Fragmentation . . . 38
4.1.4 Cluster Fragmentation . . . 40
4.1.5 QED Corrections . . . 41
4.1.6 The Detector Simulation . . . 42
4.1.7 The Used Event Generators . . . 42
4.2 Next-to-leading-order MC Simulation . . . 43
4.2.1 The Phase Space Slicing Method . . . 43
4.2.2 The Subtraction Method . . . 43

5 Event Selection **45**
5.1 Positron Reconstruction 45
5.2 Preselection 47
5.3 Kinematic Region and Jet Selection 47
5.4 Cleaning Cuts 51

6 The Analysis **55**
6.1 Noise Suppression and Global Energy Correction 55
6.2 The Jet Energy Correction 55
6.3 Comparison of Data and LO Monte Carlos 57
6.4 Efficiencies and Purities 61
6.5 Correction Factors 66
6.6 Systematic Studies 72
6.7 The Azimuthal Asymmetry 75
6.8 NLO Calculations 76

7 Results **79**
7.1 Inclusive Jet Cross Sections 79
7.2 Determination of α_s 87
7.3 Comparison with H1 92

Conclusion **96**

Bibliography **98**

Acknowledgments **102**

List of Figures

1.1 The HERA accelerator . . . 3
1.2 ZEUS detector: side view . . . 5
1.3 ZEUS detector: view along the beam line . . . 6
1.4 A CTD octant . . . 8
1.5 A FCAL module . . . 10
1.6 The geometry of the UCAL . . . 12
1.7 The ZEUS trigger system . . . 13

2.1 Sketch of a deep inelastic scattering event for the introduction of the kinematic variables . . . 14
2.2 The measured quantities for the reconstruction of the kinematic variables . . . 16
2.3 Contour lines of fixed electron energy and angle, and fixed current jet energy and angle in the (x, Q^2) plane . . . 18

3.1 Feynman diagrams for the leading-order DGLAP splitting functions. . . . 26
3.2 Feynman diagrams of the Born process, Boson-Gluon Fusion and QCD-Compton. . . . 27
3.3 Event display of two current jets. . . . 28
3.4 Feynman diagrams of the Born process, Boson-Gluon Fusion and QCD-Compton in the Breit frame. . . . 30
3.5 The definition of the azimuthal angle in the Breit frame. . . . 32
3.6 Different distributions of ϕ^{Breit} for BGF and QCDC. . . . 33

4.1 The various steps of an event generator. . . . 34
4.2 Feynman diagrams for QED corrections. . . . 41

5.1 Different methods for electron identification . . . 46
5.2 UCAL cell structure in the Breit frame (1) . . . 48
5.3 UCAL cell structure in the Breit frame (2) . . . 49
5.4 Comparison of $\cos\gamma$ on detector and hadron level . . . 49
5.5 Correlation between η^L and η^B. . . . 50
5.6 The accepted data sample in the (x, Q^2)-plane. . . . 54

6.1 Correlation between the jets' transverse energy on detector and hadron level. . . . 56
6.2 Comparison between data and LO Monte Carlos (1). . . . 58

6.3 Comparison between data and LO Monte Carlos (2). 59
6.4 Comparison between data and LO Monte Carlos (3). 60
6.5 Purities for differential jet cross sections. 62
6.6 Efficiencies for differential jet cross sections. 63
6.7 Purities for double differential jet cross sections. 64
6.8 Efficiencies for double differential jet cross sections. 65
6.9 Factors to correct the data to hadron level for the differential jet cross sections. 68
6.10 Factors to correct the data to hadron level for the double differential jet cross sections. 69
6.11 Hadronization corrections for the differential jet cross sections. . 70
6.12 Hadronization corrections for the double differential jet cross sections. 71
6.13 Systematic uncertainties for $d\sigma/dE_{t,Breit}$. 73
6.14 Systematic uncertainties for $d\sigma/dQ^2$. 74
6.15 Studies with a Monte Carlo without azimuthal asymmetry. . . . 75
6.16 Comparison of the NLO results for two different choices for the renormalization scale. 77

7.1 The inclusive differential jet cross sections $d\sigma/dQ^2$. 80
7.2 The inclusive differential jet cross sections $d\sigma/dE_{t,Breit}$. 81
7.3 The inclusive differential jet cross sections $d\sigma/d\eta^{Breit}$. 82
7.4 The inclusive differential jet cross sections $d\sigma/d\eta^{Lab}$. 83
7.5 The inclusive differential jet cross sections $d\sigma/d\phi^{Breit}$. 84
7.6 The inclusive differential jet cross sections $d\sigma/dE_{t,Breit}$ in different regions of Q^2. 85
7.7 Comparison between the data and NLO QCD for $d\sigma/dE_{t,Breit}$ in different regions of Q^2. 86
7.8 The values of α_s from $d\sigma/dQ^2$. 89
7.9 The values of α_s from $d\sigma/dE_{t,Breit}$. 90
7.10 The values of α_s from combining values from Fig. 7.8 and Fig. 7.9. 91
7.11 Comparison between data and NLO QCD for an analysis similar to one of H1. 93
7.12 Comparison with the results of Markus Wobisch. 94

List of Tables

3.1 The properties of the six quarks. 19

5.1 The effect of the various cuts on the data. 53

6.1 Results of the straight line fits to determine the parameters of the jet energy correction. 57

Introduction

At the collider HERA in Hamburg, Germany, the scattering of an electron off a proton is examined. For this purpose, the ZEUS detector has been built, which measures quantities like the place and time of a scattering event and the momenta and energies of the final state particles.

The theoretical picture of a neutral current deep inelastic event at HERA can be outlined as follows. The electron emits a virtual boson, which can be a photon or a Z boson. This virtual boson transfers a high four-momentum to a quark in the proton. This quark may radiate gluons, which can split into quark-antiquark pairs. At the end of this phase, there are quarks, antiquarks and gluons, which can not be observed as free entities. They fragment into hadrons. If a particle is electrically charged, it gives rise to a track inside of the detector. Furthermore the final state particles are absorbed in a calorimeter, which measures energy deposits in its cells. How can a statement be made about the primary fundamental process after so many evolutionary steps?

A possibility to establish an approximate relation between the detector signals and the primary fundamental process is the usage of jets. The intuitive picture of a jet is a collimated spray of particles. A jet algorithm groups together particles that have a small distance between one another. So-called jet observables are defined which are expected not to change so much in the course of the several evolutionary steps. For this thesis, the jet search is performed in the Breit frame, a special reference frame. The jet observables mainly considered are the transverse energy, $E_{t,Breit}$, the pseudorapidity, η^{Breit}, the azimuthal angle, ϕ^{Breit}, all measured in the Breit frame, and the pseudorapidity in the Laboratory frame, η^{Lab}. The transverse energy is defined by $E_t = E \sin\theta$, where E is the energy and θ is the polar angle of a jet. The pseudorapidity is a measure for the polar angle.

For this thesis, only jets are selected with a high value of $E_{t,Breit}$. Since the net transverse energy of the hadronic final state in the Breit frame is zero, there must be at least two jets in an event with balancing transverse energy. Such events are considered to arise from processes involving the strong interaction.

For the theoretical predictions a Monte Carlo program has been used which takes into account processes up to $O(\alpha_s^2)$, where α_s is the strong coupling constant. Next-to-leading order (NLO) QCD calculations are expected to give a sufficient description of the data with theoretical uncertainties much smaller than those of leading order predictions. Thus the measurement of inclusive jet cross sections serves as a test of the validity of NLO QCD.

The comparison of the measured data with NLO QCD is not straight forward, since the NLO QCD predictions are obtained on the fundamental level of quarks and gluons. To correct the data for detector effects two additional Monte Carlo programs are used. For the determination of hadronisation effects, the average of three Monte Carlo programs is taken into account.

Furthermore, the study of jet production in the Breit frame allows to measure the non-trivial dependence of the cross section on ϕ^{Breit}.

In this thesis a very large Q^2-range is covered, where Q^2 is the virtuality of the exchanged boson. A detailed view of the jet production depending on this kinematical variable will be given.

Since the theoretical values for the inclusive jet cross sections depend on α_s, the measurements have also been used to determine this parameter of QCD. It is the first time at ZEUS, that inclusive jet cross sections are used for this purpose.

Finally, this thesis will refer to an earlier publication of the H1 collaboration, which also investigate electron-proton scattering at HERA. Although their selection criteria are different from the ones applied for this thesis, a check of their results for inclusive jet cross sections is feasible.

To understand what an inclusive jet cross section is consider, as an example, the inclusive differential jet cross section

$$\left(\frac{d\sigma}{dE_{t,Breit}}\right)_i (E_{t,Breit}) = \frac{1}{L}\frac{\Delta_i N}{\Delta_i E_{t,Breit}}(E_{t,Breit}) \quad .$$

In this expression L denotes the luminosity, i a certain bin, $\Delta_i E_{t,Breit}$ the bin width and $\Delta_i N$ the number of jets. Assume an event is selected with two jets. Then each jet contributes to the inclusive jet cross section with one entry according to its $E_{t,Breit}$. Thus a short definition for the inclusive jet cross section could be: "For each selected jet there is one entry."

The first chapter describes the HERA storage ring and the ZEUS detector. In Chapter 2 the kinematical variables and the methods for their reconstruction are introduced. Chapter 3 is on the theoretical aspects. Here the reader finds the definition of the applied jet algorithm and of the Breit frame. An overview of the Monte Carlo programs is given in Chapter 4. The selection criteria are described in Chapter 5. Information on important issues of the analysis is given in Chapter 6. Here the correction factors, efficiencies and purities are shown. Finally, in Chapter 7, the results are displayed, i.e. measured cross sections, the values for α_s determined from the measurements and a comparison with the results of the H1 collaboration.

Chapter 1

The ZEUS Experiment at HERA

1.1 The Storage Ring HERA

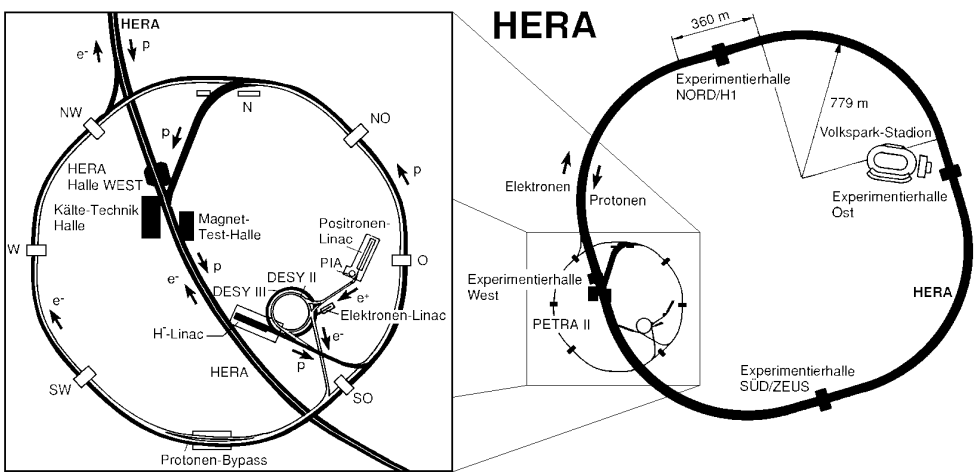

Figure 1.1: The HERA accelerator complex at DESY, Hamburg.

The storage ring HERA (**H**adron-**E**lektron-**R**inga**n**lage) at DESY (**D**eutsches **E**lektronen-**Sy**nchrotron) in Hamburg, Germany, is the world's first lepton-nucleon-collider. In two beampipes, located in a 6.3 km long tunnel 10 - 25m beneath the surface, electron and proton bunches circulate in opposite directions. The beams are guided and focussed by two independent magnet systems. The nominal beam energies are 30 GeV for the elctrons and 820 GeV for the protons. Since 1998 the proton beam energy has been 920 GeV. The term electron is often used in this thesis to label either the colliding electron or positron. In fact, in the years 1996 and 1997, of which data this thesis is based on, HERA operated with positrons. Their energy was about 27.5 GeV.

Before the beam particles are injected into HERA they undergo pre-acceler-

ation as now detailed. The proton injection starts with negative hydrogen ions (H^-) from the 50 MeV Proton LINAC, which are injected into the sychrotron DESY III. The ions pass through a thin foil, by which the electrons are stripped off. After the protons have reached an energy of 7.5 GeV, they are transferred via PETRA at an energy of 40 GeV to the HERA proton storage ring. The electrons or positrons are pre-accelerated first in a linear accelerator, LINAC I (220 MeV, e^-) or LINAC II (450 MeV, e^+) and at DESY II to 7.5 GeV . Then the particles are injected via PETRA at an energy of 14 GeV into the HERA electron storage ring.

HERA is designed to operate with 210 bunches of both protons and electrons spaced such that a crossing of a pair of bunches under zero crossing angle occurs in the intersection areas every 96 ns. In practice, there are unpaired bunches, called pilot bunches, which are used to estimate beam related background. There are also empty bunches, which allow one to study background from cosmic rays.

The particles are guided through the arcs of the storage ring by dipole magnets with a field of 0.165 Tesla for the electrons and 4.65 Tesla for the protons. Focussing of the beams is mainly done by quadrupole magnets. This type of magnet focusses only in one (for example horizontal) direction and defocusses in the other (vertical) direction. Like a light ray is focussed by an alternating arrangement of convex and concave lenses, the particle beam is kept together by quadrupole magnets of alternating focussing properties. The magnets of the electron storage ring are normal conducting operating at room temperature, whereas those for the protons are superconducting. They are cooled by helium down to a temperature of about 4 K. The particles are accelerated by electric fields in radio frequency (r.f.) cavities. After having reached the final beam energies, the r.f. system is especially needed to compensate the energy loss due to sychrotron radiation. As the radiated power is proportional to $\frac{E^4}{m^4}$ this affects the electron beam, whereas the effect on the proton beam can be neglected. However synchrotron radiation also has a stabilizing effect on the electron beam, since the momenta perpendicular to the ideal orbit are reduced and the acceleration is only longitudinal.

Since 1992, electron-proton-scattering is studied by multipurpose detectors of the international collaborations H1 and ZEUS. In one of the additional experimental zones of HERA, the HERMES experiment uses the electron beam, polarized by spin rotators, and a polarized gas target to measure the spin structure of the nucleons. A fourth experiment, HERA-B, uses wire targets in the proton beam to study the production and decay of hadrons that contain heavy quarks.

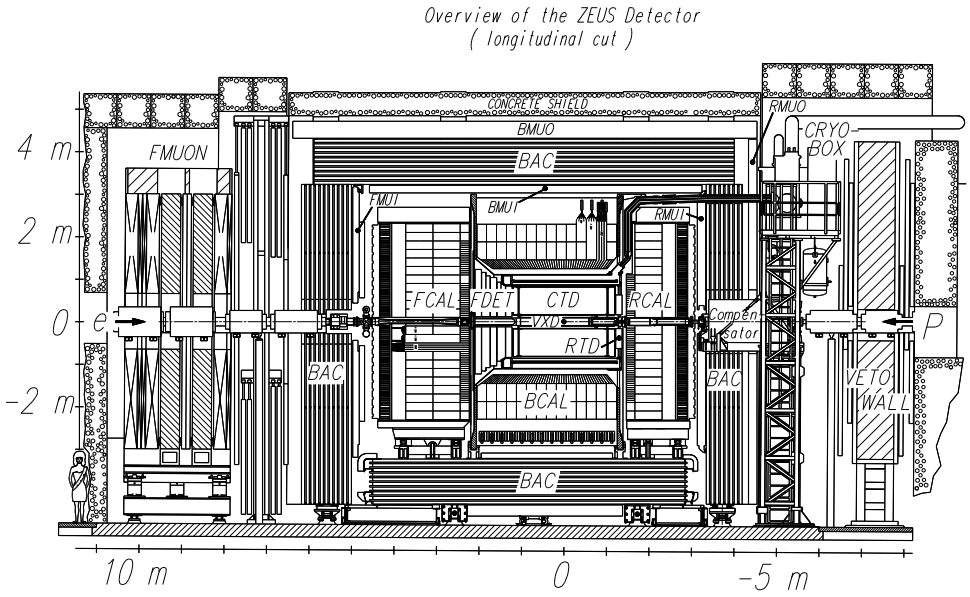

Figure 1.2: Side view of the ZEUS detector

1.2 The ZEUS Detector

1.2.1 Overview

The ZEUS detector is a multipurpose detector to measure events from electron-proton scattering. As can be seen from Fig. 1.2, the detector is asymmetric in order to accomodate the energy asymmetry due to the moving centre-of-mass system.

The ZEUS coordinate system is defined in the nominal interaction point. The Z axis is pointing in the direction of the proton beam, often referred to as *forward direction*. The Y axis points upwards and the X axis towards the middle of the storage ring. The polar angle θ is measured with respect to the positive Z axis. The polar angle is often transferred into pseudorapidity, η, by the formula $\eta = -\ln\tan\frac{\theta}{2}$. The azimuthal angle ϕ is measured with respect to the positive X axis.

Apart from some components which are further up- and downstream near the beampipe, the dimensions of the ZEUS detector are 11.6m x 10.8m x 20.0m (X, Y, Z) and its total weight is about 3600 tonnes. A detailed description of the detector can be found elsewhere [1].

In the centre around the interaction point are the tracking detectors. In the middle there is the Central Tracking Detector (CTD), which is described seperately in a subsection below. The CTD is surrounded by a superconducting magnet which provides an axial field of 1.43 T. For charged particles in the forward and rear direction there are the Forward Tracking Detector (FTD) and the Rear Tracking Detector (RTD). The FTD consists of three planar

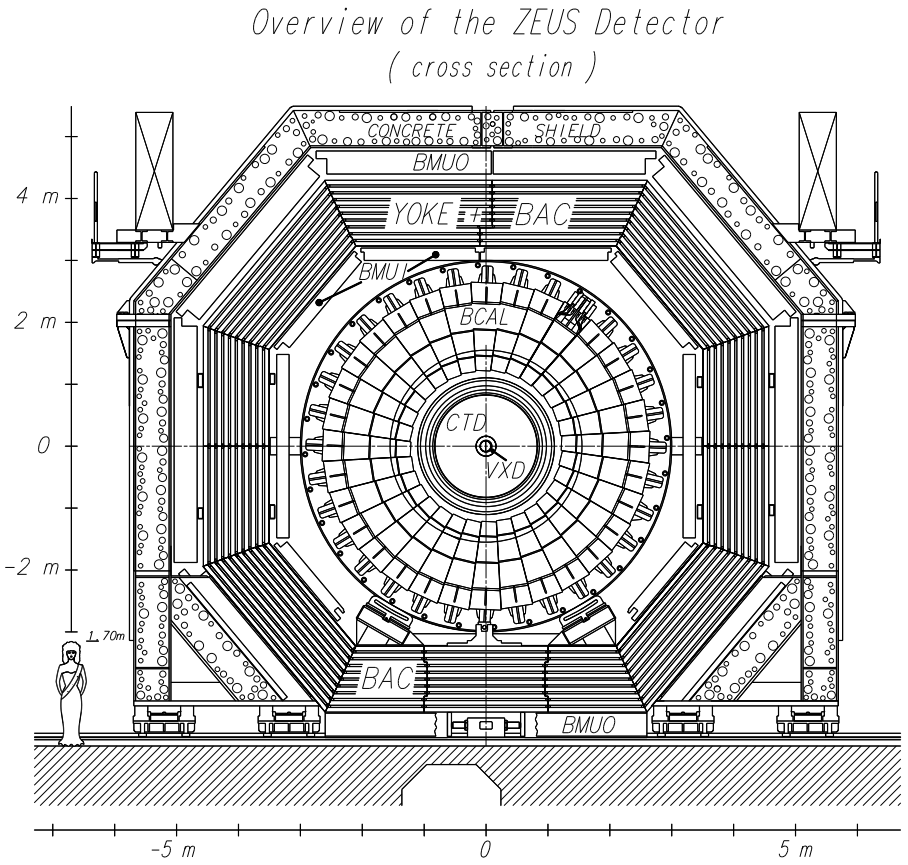

Figure 1.3: View of the ZEUS detector along the beam line

drift chambers, which are interleaved with two Transition Radiation Detectors (TRD). The RTD consists only of one drift chamber. The Vertex Detector (VXD) was removed during the winter shutdown 1995/96. A micro vertex detector (μVTX) is to be installed during the winter shutdown 2000/01. Also during this shutdown, a Straw Tube Tracker (STT) replaces the TRD.

The next layer of the ZEUS detector consists of the Uranium Calorimeter (UCAL), which is divided into three parts; a forward (FCAL), a barrel (BCAL), and a rear calorimeter (RCAL). It is the primary device to measure the energy of particles at medium and high energy and will be described in more detail further below. Since installation, several subdetectors have been added to improve the detector performance. In 1994, ouside the UCAL at $Z = 5.1$ m, the Proton Remnant Tagger (PRT) was installed. It allows one to obtain information about the hadronic final state in the forward direction at pseudorapidities of $4.3 < \eta < 5.8$ and is used to tag diffractive events. For the 1994 run period, the Small angle Rear Tracking Detector (SRTD) was added to the RCAL to improve the spatial resolution in the measurement of

the scattering angle of electrons near the beam pipe. It is mounted in front of the RCAL, where it covers a radius of about 34 cm and consists of two layers of 1 cm wide scintillating strips. At a longitudinal depth of 3 X_0 in the RCAL, the Hadron-Electron Seperator (RHES), consisting of 3 x 3 cm^2 silicon diodes, was installed prior to 1995. It is used to distinguish between electromagnetic and hadronic showers originating from low energy particles (< 5 GeV). A counterpart in the FCAL (FHES) became operational in 1998. Since 1995, the Presampler detectors (F/RPRES), consisting of a single layer of 20 x 20 cm^2 scintillator tiles, allow the correction of the scattered electron energy if the electron showers before enetring FCAL or RCAL. A presampler detector in front of the BCAL (BPRES) started operation in 1998. In 1995, the Beam Pipe Calorimeter (BPC) was added near the beam pipe in the beam hole of the RCAL. Finally, the Forward Plug Calorimeter (FPC) started operation in 1998 narrowing the beam hole of FCAL from 20 x 20 cm^2 to a radius of about 2.5 cm [2]. In 1996, the author of this thesis wrote a diploma thesis which investigated the consequences of this extension of the acceptance for diffractive scattering [3]. The FPC and the BPC are to be removed from the detector in the shutdown 2000/01.

The UCAL is surrounded by an iron yoke, which serves as a return path for the magnetic flux. It is instrumented with proportional chambers and thus used as the Backing Calorimeter (BAC) to measure the energy of particles leaking from the UCAL. Inside and outside of the iron yoke are streamer tubes by which the momenta of muons can be determined.

The luminosity is measured using bremsstrahlung photons from the Bethe-Heitler process $ep \rightarrow e\gamma p$. The cross section of this process is known from QED to an accuracy of 0.5%. Photons with $\theta_\gamma < 0.5$ mrad are measured in a small lead-scintillator calorimeter at Z = -107 m. Two layers of 1 cm wide crossing scintillator strips are installed at a depth of 7 X_0 to provide a position resolution of 0.2 cm [4]. At Z = -35 m another lead-scintillator calorimeter for electrons is installed, which is used to tag the scattered electron in a photoproduction event. At Z = -8 m and Z = -44 m tungsten-scintillator calorimeters were added to extend the acceptance for electron tagging.

In the forward direction, located between Z =26 and 96 m, six stations of silicon strip detectors are mounted very close to the beam line. This Leading Proton Spectrometer (LPS) measures very forward scattered protons at a transverse momentum of $p_t < 1$ GeV/c. At Z = 105.6 m the Forward Neutron Calorimeter (FNC), a lead-scintillator calorimeter, detects very forward produced neutrons.

1.2.2 The Central Tracking Detector (CTD)

The CTD is a cylindrical drift providing a precise measurement of the direction and momentum of charged particles. In addition, particles can be identified via the estimate of the energy loss, dE/dx.

In a drift chamber the traversing charged particle ionises gas atoms. The

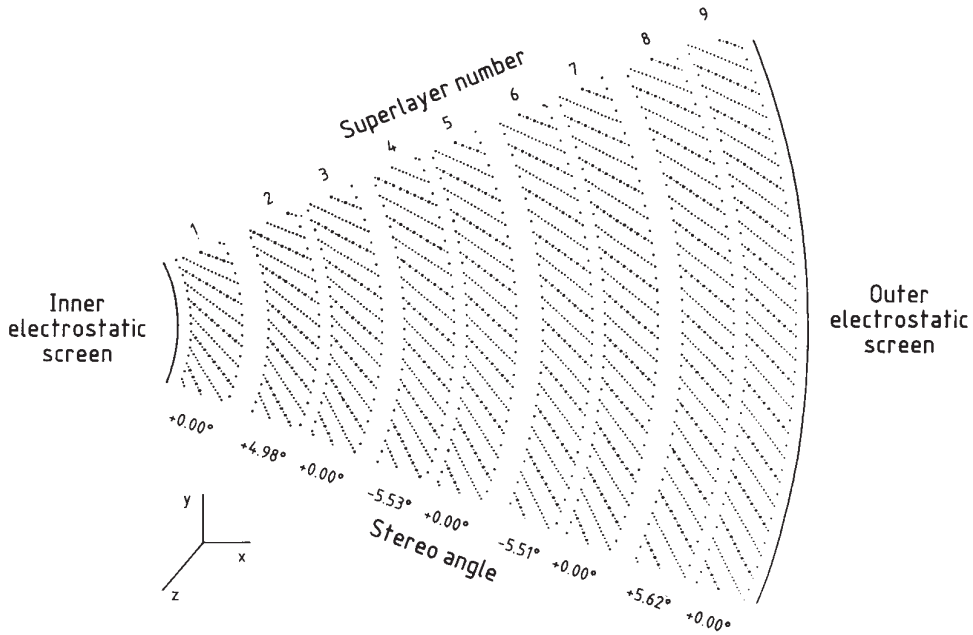

Figure 1.4: CTD octant with sense and field wires.

electric field between the wires is mostly homogeneous leading to a constant velocity of the electrons to the anode wires. Very close to a wire the field increases rapidly resulting in an avalanche of further electrons. Thus a pulse can be measured.

The CTD is 205 cm long with an inner radius of 18.2 cm and an outer radius of 79.4 cm. The covered polar angle extends from $\theta = 15°$ to 164°. It is filled with a gas mixture of argon, CO_2 and ethane. The drift velocity is $\omega \simeq 50\mu$m/ns.

The CTD is equipped with 4608 thin sense wires and 19584 thick field-shaping wires. The wires are arranged in 72 radial drift layers organised in 9 superlayers as can be seen in figure 1.4, which shows a CTD octant. The odd superlayers are *axial* layers with the sense wires arranged parallel to the beam axis. The even superlayers are called *stereo* layers. Here the sense wires are inclined at angles of about 5° with respect to the beam axis to allow the determination of the Z position of the tracks. In addition, the Z position is detemined from the difference in the arrival time of the pulse at the ends of the chamber. Only the inner three axial superlayers are equipped by this so-called Z-by timing system ($\sigma_Z \simeq 4$cm).

The transverse momentum resolution for full-length tracks is $\sigma(p_t)/p_t = 0.0058 \cdot p_t \oplus 0.0065 \oplus 0.0014/p_t$ (p_t in GeV/c). The interaction vertex is measured with a typical longitudinal (transverse) resolution of 0.4 cm (0.1 cm).

1.2.3 The Uranium Calorimeter

The Uranium Calorimeter (UCAL) is a compensating sandwich sampling calorimeter [5]. As it is the primary device used in this thesis, it will be described in more detail. First, there will be some remarks on the basics of calorimetry in high energy physics. Then peculiarities of the UCAL will be given. Finally, some methods for calibration will be mentioned.

A calorimeter is a device to measure the energy of particles. The particles are absorbed in the calorimeter, which in the case of the UCAL results in an amount of photons which is proportional to the energy of the incident particles. When a particle passes matter, part of the particle's energy comes up for the creation of new particles, which can also produce secondary particles. Thus a cascade is created, which is called *shower*. The shower terminates when the energy of the particles are too small for the creation of further particles and absorption is dominant. Due to their different nature, showers initiated by photons, electrons, or positrons are called *electromagnetic showers*, and those initiated by hadrons are called *hadron showers*.

When a high energy electron traverses matter, it loses energy by emitting a bremsstrahlung gamma in the electric field of a nucleus. The gamma, also in the field of a nucleus, can create an electron-positron pair. Either electron and positron can be slowed down by bremsstrahlung and so on. This proliferation of particles stops when the electrons and positrons have approximately an energy of the order of the *critical energy* E_c. E_c is defined as the energy at which an electron or positron loses the same amount of energy by bremsstrahlung or ionisation. Processes that mainly occur at lower energies are Compton scattering and the photoeffect, in the case of photons, and ionisation and excitation, in the case of electrons and positrons. An electromagnetic shower is described in terms of the *radiation length* X_0. X_0 depends on the material and is the distance at which, on average, a high energy electron looses energy by a factor of e because of bremsstrahlung.

In the UCAL charged particles produce light in the scintillating layers. For the sake of compactness, these layers are interleaved with layers of depleted uranium as passive, absorbent material. The production of charged particles is a statistical process causing *intrinsic fluctuations*. As the fraction of particles that pass the scintillator varies, there are also *sampling fluctuations*.

When a high energy hadron enters matter, it causes a shower because of inelastic reactions with the nuclei. In the case of energies above 50 MeV, the incident hadron can cause spallation [6]. Spallation can be described in two steps. In the first step the primary hadron pierces a nucleus und causes a *intranuclear cascade* due to elastic and inelastic scattering with the nucleons. The affected nucleons can absorb energy, traverse the nucleus and interact with other nucleons. If the energy is sufficiently high, secondary particles, e.g. pions, can be produced. At the boundary of the nucleus a particle can leave the nucleus if its energy is higher than the binding energy. Otherwise, its energy is distributed among the constituents. In the second step of spallation,

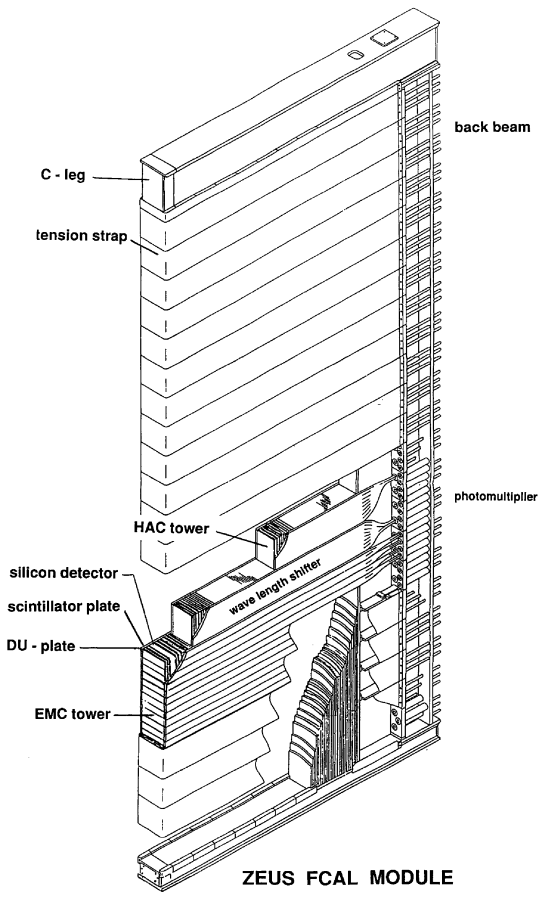

Figure 1.5: Three-dimensional view of a FCAL module

the liberated particles hit further nuclei along the shower axis. This phase is called the *internuclear cascade*. After the intranuclear cascade the nucleus is mostly excited and can evaporate particles. Highly energetic pions, protons and neutrons can also cause nuclear fission. Either by evaporation or fission, photons and neutrons are produced with an energy in the order of a few MeV. Neutral pions are a considerable component in a hadron cascade constituting about a third of the produced pions increasing with the energy of the primary particle. The number of neutral pions in a hadron strongly fluctuates and is mostly dependent on the first inelastic reaction [7]. Neutral pions decay rapidly ($\approx 10^{-16}$s) into two photons and thus cause an electromagnetic subshower. A measure for the dimensions of a hadron shower is the *nuclear absorption length* λ which is much larger than X_0 for most materials. A large amount of the energy of the primary particle remains invisible in the calorimeter. In nuclear fission or when secondary particles leave a nucleus the energy of the final state is reduced by the binding energy. In most cases the heavy fragments of a

nucleus do not reach an active layer of the sampling calorimeter. The muons from the decay of charged pions leave only a weak signal in the calorimeter. The neutrinos from such decays generally cause no signal. Special care has to be taken to measure the energy of slow neutrons.

In order to achieve a good energy resolution it is important to have the signal, e, of a photon, electron or positron equal to the signal, h, of a hadron of the same incident energy. The value of e/h in a sampling calorimeter depends on the atomic charge of the absorbing material, the thickness of the passive and active layers, the signal integration time of the detector and the properties of the readout material [8]. To measure slow neutrons organic scintillator is used. The neutrons can scatter elastically from the protons of the hydrogen atoms in the scintillator. These so-called *recoil protons* cause a signal as they have electric charge. The amount of neutrons can be increased by the choice of uranium as passive material due to fission. Furthermore, materials with a large atomic charge absorb low energy photons in a electromagnetic shower.

The UCAL consists of alternating layers of depleted uranium plates (3.3 mm thick $\simeq 1X_0$) and plastic scintillator SCSN38 plates (2.6 mm thick). It is compensating, i.e. $e/h = 1.0 \pm 0.03$ if $E > 3$ GeV. The relative energy resolutions measured in test beams are $\sigma(E)/E = 18\%/\sqrt{E} \oplus 1\%$ for electromagnetic showers and $\sigma(E)/E = 35\%/\sqrt{E} \oplus 2\%$ for hadron showers, where the energy is in GeV. The UCAL is a 4π detector with the exception of the holes accommodating the beam pipe. It covers more than 99.5% of the solid angle. The FCAL covers a polar angle from 2.2° to 39.9°, the BCAL from 36.7° to 129.1° and the RCAL from 128.1° to 176.5°. Each calorimeter part is divided into modules. The FCAL and RCAL modules are 20 cm wide (In Figure 1.5 a FCAL module is shown). A BCAL module is of wedge-shaped design and extends over an azimuthal angle of 11.25°. Each module is subdivided into towers, which are further subdivided into cells. The cells that face the interaction point are those of the electromagnetic calorimeter (EMC). Behind the EMC cells are the hadronic calorimeter cells (HAC). The front area of the HAC cells of FCAL and RCAL is 20 x 20 cm^2. The front area of an EMC cell of FCAL (RCAL) measures 5 x 20 cm^2 (10 x 20 cm^2). The EMC of the BCAL are projective with respect to the interaction point. The longitudinal depth of the EMC cells is about 25 X_0 ($\simeq 1\lambda$). The depth of the HAC cells can be taken from Figure 1.6. Each cell is read out at two sides via wavelength shifters which are coupled to photomultiplier tubes (PMTs). The UCAL also provides timing information with a resolution better than 1 ns for energy deposits greater than 4.5 GeV.

During operation of ZEUS, the calorimeter is frequently calibrated on a channel-by-channel basis. *Charge injection* test pulses are used to calibrate the electronic read out chain. The radioactive decay of uranium provides a small, constant reference signal, the *Uranium noise* (UNO). The gain of the PMTs is trimmed by adjustment of the high voltage from time to time to yield a defined response to this signal. Thus aging effects of the scintillator, wavelength shifters and PMTs are compensated. A combined LED/Laser light

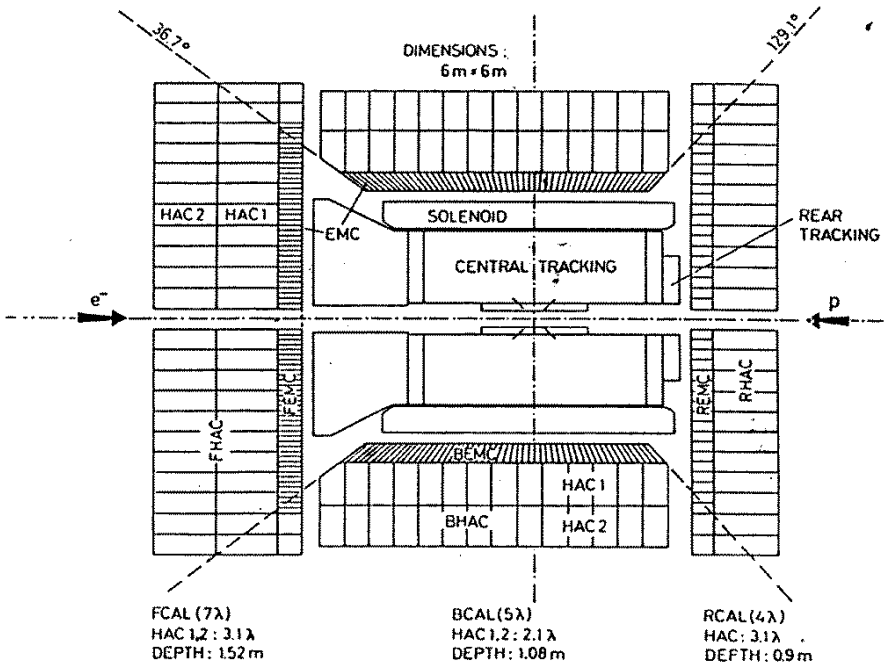

Figure 1.6: Cell structure of the uranium calorimeter

pulser system has been installed to measure the yield of photoelectrons per GeV. This system can also be used to make long term studies concerning aging effects.

1.2.4 Trigger

HERA has a bunch crossing time of 96 ns, equivalent to a rate of about 10 MHz. The total interaction rate is of the order of 10 - 100 kHz and is dominated by background from interactions of the proton beam with the residual gas. Other sources of background reactions are electron beam gas collisions, beam halo and cosmic events. The rate of *ep* physics events is only of the order of a few Hz. Some physics events have a much higher cross section than others. They need to be prescaled, i.e. only a fraction of them is recorded. Thus the task of the trigger system is the identification of the process type and to suppress background-induced events efficiently without losing interesting physics events.

ZEUS employs a three-level trigger system. A schematic diagram of the ZEUS trigger is shown in Figure 1.7. The *First Level Trigger* (FLT) is a hardware trigger, designed to reduce the input rate to 1 kHz. Each detector component has its own FLT and a 10.4 MHz pipeline to store the data and avoid dead time losses. Each local FLT sends its decision to the Global First Level Trigger (GFLT). The GFLT issues, not later than 4.4 μs after the interaction, a global trigger decision. The *Second Level Trigger* (SLT) is designed to reduce the input rate to below 100 Hz. This trigger level is also subdivided in

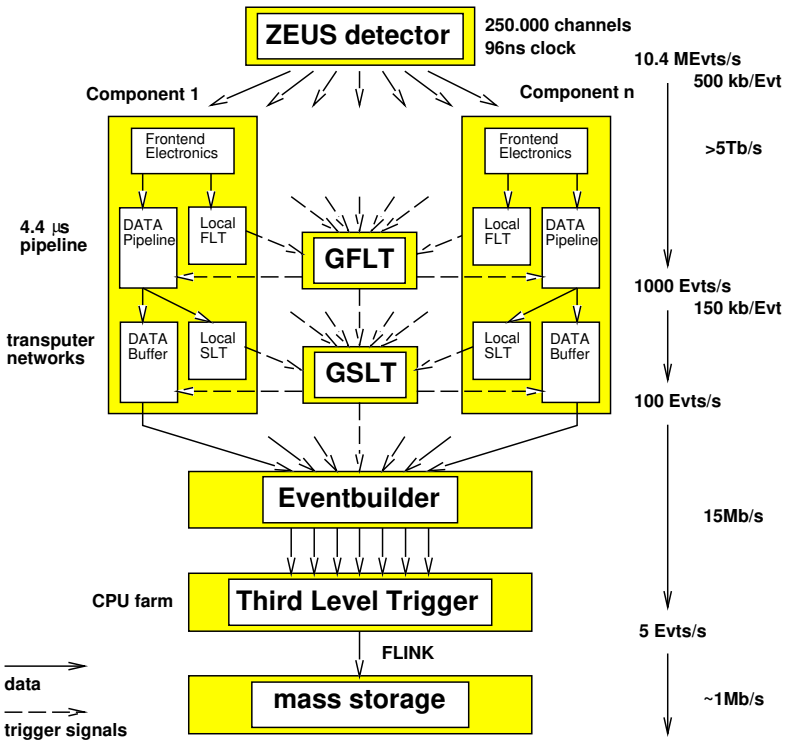

Figure 1.7: Schematic diagram of the ZEUS trigger and data acquisition system

component related parts running on a network of transputers. It is software-based, so simple algorithms can run to identify event types. If the event is accepted by the Global Second Level Trigger (GSLT), all detector components send their data to the *Event Builder* which produces an event structure on which the *Third Level Trigger* (TLT) code runs and which is used offline in the analysis. The TLT consists of a processor farm of Silicon Graphics CPUs. Accepted events are written to tape via an optical fibre link.

Chapter 2

Kinematic Variables

2.1 Definition

A deep inelastic scattering event can be described by kinematic variables that are invariant under a Lorentz transformation. The invariance can be seen from the fact that their definitions contain scalar products of four-vectors. The metric used in this thesis is defined such that the scalar product of two four-vectors a and b is $ab = a^0b^0 - a^1b^1 - a^2b^2 - a^3b^3$. As is common in high energy physics, Planck's constant, $\hbar$, and the speed of light, c, will be set to unity.

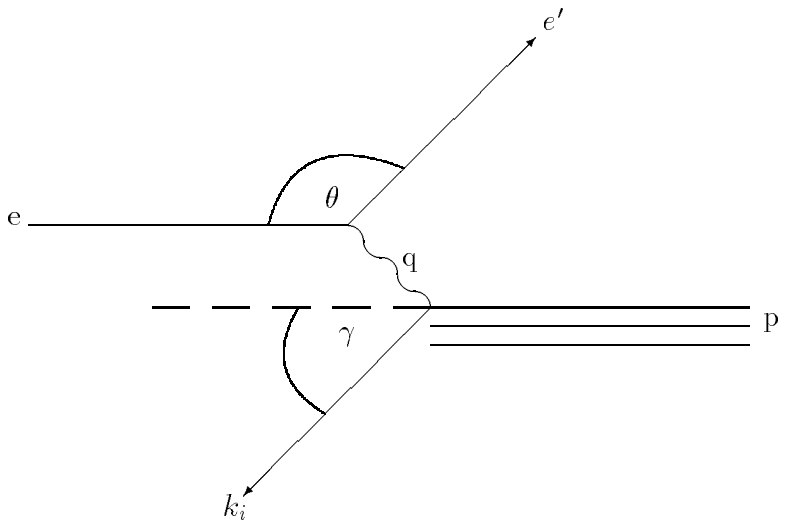

Figure 2.1: A quark from the proton is scattered by a virtual photon emitted from the electron.

Figure 2.1 shows a neutral current deep inelastic scattering event to lowest order. The intermediate boson can be a photon or a Z^0. This process is described by the Quark Parton Model (QPM), which will be further explained in the next chapter. In figure 2.1 the energy-momentum four-vectors of the

incident and scattered electron and of the incoming proton are given by e, e' and p, respectively. The polar angles of the scattered electron and quark are denoted by θ and γ, respectively. The kinematic variables are defined and can be approximated in the following way [9]:
The square of the total energy in the centre-of-mass frame is denoted by s;

$$s = (e + p)^2 \approx 4E_e E_p \approx 90200\text{GeV}^2, \tag{2.1}$$

where E_e and E_p are the energies of the incoming electron and proton, respectively. The masses of the electron and proton were neglected. The square of the four-momentum transfer is redefined because of its negative sign.

$$q^2 = (e - e')^2 =: -Q^2 \approx -2E_e E_e{}' (1 + \cos\theta), \tag{2.2}$$

where $E_e{}'$ is the energy of the scattered electron. The variable y defined by

$$y = \frac{pq}{pe} \tag{2.3}$$

is a measure for the "inelasticity" of the process so-called, because in the proton rest frame it equals

$$y = 1 - \frac{E_e{}'}{E_e}. \tag{2.4}$$

The so-called Bjorken scaling variable x is given by

$$x = \frac{Q^2}{2pq} \tag{2.5}$$

and in the QPM is the fraction of the proton momentum carried by the scattered quark. The variables mentioned so far are correlated such that,

$$Q^2 \approx xys \tag{2.6}$$

As x and y both range between 0 and 1, the maximal value for Q^2 is $Q^2_{max} \approx s$. A further variable is the invariant mass of the intermediate boson-proton system,

$$W^2 = (q + p)^2 \approx Q^2 \frac{1 - x}{x}. \tag{2.7}$$

A quantity, which is important for the selection of the kinematic range in this thesis, is

$$\cos\gamma = \frac{x(1 - y)E_p - yE_e}{x(1 - y)E_p + yE_e}. \tag{2.8}$$

Obviously this quantity is not invariant under a Lorentz transformation. However, as the beam energies can be treated as constants, cuts on $\cos\gamma$ are also well suited to select a kinematic range.

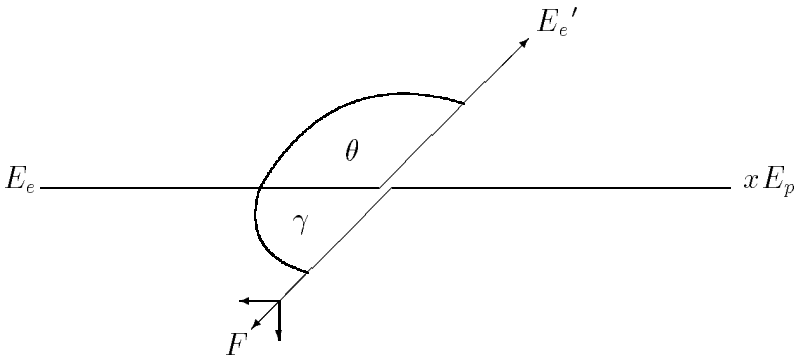

Figure 2.2: The measured quantities for the reconstruction of the kinematic variables

2.2 Reconstruction

The kinematics of deep inelastic scattering events are specified with two variables, as described in the previous section. The experiment measures the energy, E_e', and polar angle, θ, of the scattered electron, and the energy, F, and the characteristic polar angle, γ, of the hadronic final state. In figure 2.2 a QPM event is shown. The arrows at the end of the quark line are supposed to indicate that the scattered quark evolves into a collimated spray of colour-singlet hadrons, called the *current jet*. In this figure the initial energy of the quark is denoted with xE_p indicating that it is an unknown quantity. Energy and momentum conservation yield the following equations [10]:

$$\left.\begin{array}{rcl} \text{energy conservation} & : & xE_p + E_e = E_e' + F \\ \text{longitudinal momentum conservation} & : & xE_p - E_e = E_e' \cos\theta + F\cos\gamma \end{array}\right\}$$

$$\Longrightarrow \quad : \quad 2E_e = E_e'\,(1-\cos\theta) + F\,(1-\cos\gamma)$$

$$\text{transverse momentum conservation} \quad : \quad E_e' \sin\theta = F \sin\gamma$$

These equations allow one to express two of the measured quantities in terms of the other two. There are six combination of E_e', θ, F, and γ to build a pair. Three of them will be used further, to reconstruct the kinematic variables:

E_e', θ	electron method
$E_e'[F,\gamma], \theta[F,\gamma]$	Jacquet-Blondel method
$E_e'[\theta,\gamma], \theta$	double angle method

An easy way to calculate Q^2 and y for the various methods is to start with the electron method and then to use the equations above. The resulting formulae are:

- **electron method**

$$Q^2_{el} = 2E_e E_e{}' (1 + \cos\theta) \tag{2.9}$$

$$y_{el} = 1 - \frac{E_e{}'}{2E_e} (1 - \cos\theta) \tag{2.10}$$

- **Jacquet-Blondel method**

$$Q^2_{JB} = \frac{F^2 \sin^2\gamma}{1 - y_{JB}} = \frac{(\sum p_x)^2 + (\sum p_y)^2}{1 - y_{JB}} \tag{2.11}$$

$$y_{JB} = \frac{F(1 - \cos\gamma)}{2E_e} = \frac{\sum (E - p_z)}{2E_e} \tag{2.12}$$

- **double angle method**

$$Q^2_{DA} = \frac{4E_e^2 \sin\gamma (1 + \cos\theta)}{\sin\gamma + \sin\theta - \sin(\theta + \gamma)} \tag{2.13}$$

$$y_{DA} = \frac{\sin\theta (1 - \cos\gamma)}{\sin\gamma + \sin\theta - \sin(\theta + \gamma)} \tag{2.14}$$

Another result of the Jacquet-Blondel method is a prescription to reconstruct the hadronic angle γ:

$$\cos\gamma = \frac{(\sum p_x)^2 + (\sum p_y)^2 - (\sum (E - p_z))^2}{(\sum p_x)^2 + (\sum p_y)^2 + (\sum (E - p_z))^2} \tag{2.15}$$

The electron method has been used in fixed target experiments. Since only one particle needs to be measured, it is the easiest method. However, the x resolution is seriously degraded at small y. Furthermore, a photon can be radiated from the electron which can lead to large radiative corrections. At large y the resolution is very good.

The Jacquet-Blondel method relies entirely on the hadronic system. The sums in the formula above run over all final state hadrons. In practice, the final state hadrons are represented by tracks or calorimeter energy deposits. This method is stable against energy losses down the forward beam pipe since they contribute very little. However, it is sensitive to calorimeter noise at very small y, and to energy losses in the rear direction at higher values of y. It also requires a good understanding of the calorimeter energy scale and energy losses in inactive material. On the other hand, it is rather insensitve to radiative corrections.

The double angle method has the advantage that it does not require precise knowledge of energy scales (variations in scale with polar angle will however distort the γ measurement). It also results in small radiative corrections. However, the resolution is poor if y is very small [11].

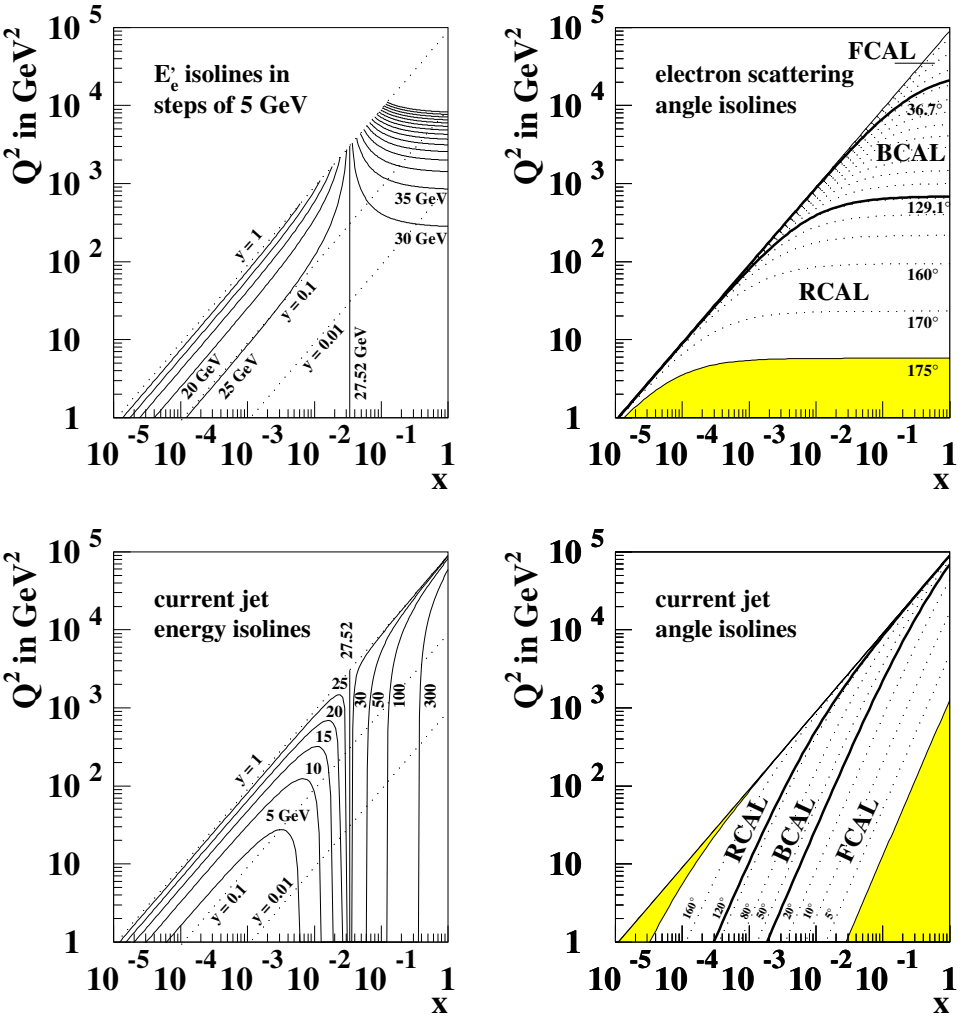

Figure 2.3: Contour lines of fixed electron energy and angle, and fixed current jet energy and angle in the (x, Q^2) plane

Chapter 3

Theory

3.1 QCD and DIS

This section is intended to give an introduction to Quantum Chromodynamics (QCD) and the theory of deep inelastic (electron-proton) scattering (DIS). The material presented here is given in more detail elsewhere [12–15].

3.1.1 Fundamentals of QCD

QCD states that hadrons are made out of quarks. This idea arose from the interpretation of the spectrum of low-mass mesons and baryons. The symmetry SU(3) of flavour [$SU(3)_f$] was introduced. The flavours taken into account were u, d and s. The six known quarks and some of their properties are shown in table 3.1. As can be seen from this table, $SU(3)_f$ is only an approximate symmetry, since the masses of u, d and s are different. The baryons were considered to consist of three quarks. They must have half-integral spin, such that the spins of the low-mass baryons have the observed value. The wave function of the spin-$\frac{3}{2}$ baryons is then symmetrical in space, spin and $SU(3)_f$. To account for Fermi-Dirac statistics the colour degree of freedom was introduced. A colour index a, usually called red, green, blue for $a = 1, 2, 3$, is carried by each quark. The wave function of a baryon is postulated to be totally antisymmetric in this new index.

Quark	Electric Charge	Mass	Spin	Baryon Number
u	+2/3	$\sim$ 4 MeV	1/2	1/3
d	-1/3	$\sim$ 7 MeV	1/2	1/3
c	+2/3	$\sim$ 1.5 GeV	1/2	1/3
s	-1/3	$\sim$ 135 MeV	1/2	1/3
t	+2/3	$\sim$ 175 GeV	1/2	1/3
b	-1/3	$\sim$ 5 GeV	1/2	1/3

Table 3.1: The properties of the six quarks.

In order not to have a proliferation of states it is imposed that only colour singlet states can exist in nature. The exact symmetry SU(3) of colour is introduced. The quarks q_a transform according to the fundamental representation, i.e. a 3×3 unitary matrix. (The antiquarks $\bar{q}^a$ transform according to the complex conjugate representation.) The basic colour singlet states for the mesons are $q_a \bar{q}^a$ and for the baryons $\epsilon^{abc} q_a q_b q_c$, where ϵ^{abc} is the totally antisymmetric tensor.

The electron deep inelastic scattering experiments at SLAC [16] indicated that the nucleon was built out of approximately point-like constituents. It had been expected that the cross section would decrease exponentially with rising inelasticity. It was found that the measured cross section was rather constant. (Such a behaviour is called "scaling".) The constituents of hadrons were afterwards called "partons", which are now known to be the coloured quarks and gluons.

For a long time there seemed to be a contradiction. On the one hand, since a free quark has never been observed, there must be a strong force that confines the quark to a hadron. On the other hand, when a quark was probed by a photon in deep inelastic scattering it appeared as a free particle. These two phenomena were finally explained by "asymptotic freedom". This concept predicts that the coupling between quarks is large at large distances which explains why quarks only exist as bound states. At short distances the coupling is predicted to be small. That is the reason why for large momentum transfers the quark is an approximately free particle. However, the approach to complete freedom is very slow and at finite energies the theory always predicts corrections.

The gluons are massless vector bosons mediating the strong force between quarks. There are eight of them belonging to a colour-anticolour octet. The colour-anticolour states of the eight gluons can be written as

$$r\bar{b}, r\bar{g}, b\bar{g}, b\bar{r}, g\bar{r}, g\bar{b}, \frac{r\bar{r} - b\bar{b}}{\sqrt{2}}, \frac{r\bar{r} + b\bar{b} - 2g\bar{g}}{\sqrt{6}}. \tag{3.1}$$

One would expect that there are nine combinations of three colours and three anticolours. However, the 'ninth gluon' is a colour singlet particle and has never been observed. As gluons are coloured they can couple with one another. Direct experimental piece of evidence for the existence of gluons was the observation of three-jet events at the storage ring PETRA in 1979 [17].

The quarks constituting a hadron are called *valence quarks*. However there are also short lived quarks appearing for example when a gluon splits into a quark-antiquark pair. These quarks are called *sea quarks*. In a scattering experiment they can also participate in an interaction with the other colliding beam.

3.1.2 The Renormalization Scale

When Feynman diagrams are evaluated that contain loops, divergent integrals occur. The reason for this is that there is no upper limit for the energy of

particles in a loop. The resulting divergence is known as ultraviolet singularity. In a so-called *regularization* procedure the integrals are made "temporarily finite" by introducing, for example, a gluon mass, an ultraviolet momentum cut-off or a fractional space-time dimension. The mathematical expressions are then well-defined, though they have a divergent limit. The next step is to absorb the regularized divergences into the definition of physical quantities through a *renormalization* procedure. This leads to the introduction of a new dimensional scale μ_r, the so-called *renormalization scale*. Renormalized quantities in the theory, such as the strong coupling α_s, depend explicitly on μ_r. Different prescriptions for the renormalization with different choices for μ_r must result in the same observable amplitudes. The transformation of renormalized operators as μ_r is changed form a Lie group, which is called the *Renormalization Group*. The equations that express the invariance of physical quantities when changing μ_r are refered to as *Renormalization Group Equations* (RGE).

As an example consider a dimensionless physical quantity R which depends on an energy scale Q. This scale is assumed to be much larger than the other dimensionful parameters like quark masses which shall therefore be neglected. Since R is dimensionless one would suggest that this observable has a constant value. In a renormalizable quantum field theory a second energy scale, μ_r, is introduced and R depends in general on the ratio Q^2/μ_r^2. This means that R is not a constant. It shall be further assumed that R depends on the dimensionless strong coupling α_s. The RGE is then

$$\mu_r^2 \frac{d}{d\mu_r^2} R(Q^2/\mu_r^2, \alpha_s) \equiv \left[\mu_r^2 \frac{\partial}{\partial \mu_r^2} + \mu_r^2 \frac{\partial \alpha_s}{\partial \mu_r^2} \frac{\partial}{\partial \alpha_s} \right] R = 0. \tag{3.2}$$

An analysis of this partial differential equation shows that $R(1, \alpha_s(Q^2))$ is a solution. Hence all of the scale dependence in R enters through the so-called *running* of the coupling constant $\alpha_s(Q^2)$. The running of α_s is determined by

$$Q^2 \frac{\partial \alpha_s}{\partial Q^2} = \beta(\alpha_s). \tag{3.3}$$

In QCD, the β function has the perturbative expansion

$$\beta(\alpha_s) = -b\alpha_s^2(1 + b'\alpha_s + O(\alpha_s^2)) \tag{3.4}$$

where

$$b = \frac{(33 - 2n_f)}{12\pi}, \qquad b' = \frac{(153 - 19n_f)}{2\pi(33 - 2n_f)} \tag{3.5}$$

and n_f is the number of active light flavours. If both $\alpha_s(\mu_r^2)$ and $\alpha_s(Q^2)$ are in the perturbative region it makes sense to truncate the series on the right-hand-side and solve the resulting differential equation for $\alpha_s(Q^2)$. For example, neglecting the b' and higher coefficients gives the solution

$$\alpha_s(Q^2) = \frac{\alpha_s(\mu_r^2)}{1 + \alpha_s(\mu_r^2) b \ln(Q^2/\mu_r^2)}. \tag{3.6}$$

Evidently as Q^2 becomes much larger than μ_r^2, the running coupling $\alpha_s(Q^2)$ decreases to zero. This is the property of *asymptotic freedom*. Including the next-to-leading order coefficient b' yields

$$\frac{1}{\alpha_s(Q^2)} - \frac{1}{\alpha_s(\mu_r^2)} + b' \ln\left(\frac{\alpha_s(Q^2)}{1+b'\alpha_s(Q^2)}\right) - b' \ln\left(\frac{\alpha_s(\mu_r^2)}{1+b'\alpha_s(\mu_r^2)}\right) = b \ln\frac{Q^2}{\mu_r^2} \quad (3.7)$$

In practice, given values for $\ln(Q^2/\mu_r^2)$ and $\alpha_s(\mu_r^2)$, $\alpha_s(Q^2)$ can be obtained numerically.

3.1.3 Structure Functions

This section discusses the structure functions in deep inelastic scattering (DIS). DIS is defined to be a scattering process of a lepton at a nucleon target with high four-momentum transfer, i.e. $Q^2 \gg 1$ GeV^2. The treatment in this section is confined to electron-proton and positron-proton scattering with their differences indicated. Only neutral current DIS events will be taken into account, i.e. the electron emits a photon or a Z.

Consider first the case in which Q^2 is much less than the mass of the Z squared, M_Z^2. In this case the intermediate boson coming from the electron is a virtual photon. The structure functions $F_i(x, Q^2)$ - which absorb the unknown couplings of the electron current to the proton - are defined in terms of the inclusive differential cross section

$$\frac{d^2\sigma(ep \to eX)}{dxdQ^2} = \frac{4\pi\alpha^2}{Q^4}\left[[1+(1-y)^2]F_1 + \frac{(1-y)}{x}(F_2 - 2xF_1)\right], \quad (3.8)$$

where α is the electromagnetic coupling constant. The kinematic variables x, Q^2 and y have been defined in the Chapter 2. The *Bjorken limit* is defined as $Q^2 \to \infty$ with x fixed. In this limit the structure functions are observed to obey an approximate *scaling* law, i.e. they depend only on the dimensionless variable x:

$$F_i(x, Q^2) \longrightarrow F_i(x). \quad (3.9)$$

This so-called Bjorken scaling implies that the virtual photon scatters off pointlike constituents, since otherwise the dimensionless structure functions would depend on the ratio Q/Q_0, with $1/Q_0$ some length scale characterizing the size of the constituents. Bjorken scaling gave rise to the parton model. The parton model is most easily formulated in the 'infinite momentum frame' in which the proton is moving very fast. In this frame, consider a simple model where the photon scatters off a pointlike quark constituent which is moving parallel with the proton and carrying a fraction, ξ, of its momentum. A calculation for spin-averaged massless electron-quark scattering then reveals that the quark structure functions, $\hat{F}_i$, are

$$\hat{F}_2 = xe_q^2\delta(x-\xi) = 2x\hat{F}_1, \quad (3.10)$$

where e_q is the electric charge of the quark in units of the elementary charge. However, the measured structure function is a distribution in x rather than

a delta function, which indicates that the quark constituents carry a range of momentum fractions. The above ideas are incorporated in the two following assumptions:

- $q(\xi)d\xi$ represents the probability that a quark, q, carries momentum fraction between ξ and $\xi + d\xi$, where $0 \leq \xi \leq 1$. $q(\xi)$ is called the *parton density function* (PDF).
- The virtual photon scatters incoherently off the quark constituents.

Thus the proton structure functions are obtained by weighting the quark structure functions with the probability distribution $q(\xi)$,

$$F_2(x) = 2xF_1(x) = \sum_{q,\bar{q}} \int_0^1 d\xi q(\xi) x e_q^2 \delta(x - \xi) = \sum_{q,\bar{q}} e_q^2 x q(x). \tag{3.11}$$

The first equality is known as the *Callan-Gross relation*. It is a direct consequence of the spin-$\frac{1}{2}$ property of the quarks. To understand this, note that the two terms in the square brackets on the right-hand side of Eq.(3.8) correspond to the absorption of transversely (F_1) and longitudinally ($F_2 - 2xF_1$) polarized virtual photons. The Callan-Gross relation follows from the fact that a spin-$\frac{1}{2}$ quark cannot absorb a longitudinally polarized vector boson. In contrast, spin-0 (scalar) quarks cannot absorb transversely polarized vector bosons and so would have $F_1 = 0$. Structure function measurements show that $(F_2 - 2xF_1) \ll F_2$, confirming the spin-$\frac{1}{2}$ property of quarks.

At very high energies, in particular for $Q^2 \sim M_Z^2$, the contribution to $ep \to eX$ scattering from Z exchange cannot be ignored. The generalization of Eq. (3.8) which incorporates all neutral current terms is

$$\frac{d^2\sigma_{NC}(e^{\pm}p)}{dxdQ^2} = \frac{4\pi\alpha^2}{xQ^4}[xy^2 F_1^{NC} + (1-y)F_2^{NC} \mp xy(1 - \frac{1}{2}y)F_3^{NC}], \tag{3.12}$$

where

$$F_2^{NC} = 2xF_1^{NC} = \sum_q x[q(x) + \bar{q}(x)]C_q(Q^2) \tag{3.13}$$

$$xF_3^{NC} = \sum_q x[q(x) - \bar{q}(x)]D_q(Q^2), \tag{3.14}$$

with

$$C_q(Q^2) = e_q^2 - 2e_q V_e V_q P_Z + (V_e^2 + A_e^2)(V_q^2 + A_q^2)P_Z^2 \tag{3.15}$$

$$D_q(Q^2) = -2e_q A_e A_q P_Z + 4V_e A_e V_q A_q P_Z^2 \tag{3.16}$$

$$P_Z = \frac{Q^2}{(Q^2 + M_Z^2)\sin^2 2\theta_W}. \tag{3.17}$$

Note the appearance of an additional parity-violating structure function F_3^{NC}. The vector and axial couplings of the fermions to the Z boson are

$$V_i = T_{i3} - 2e_i \sin^2\theta_W, \quad A_i = T_{i3}, \tag{3.18}$$

where T_{i3} is the third component of the weak isospin and θ_W denotes the Weinberg mixing angle. Note that the only difference between positron-proton and electron-proton scattering is the sign in front of F_3^{NC} (For V_e and A_e always take the vector and axial couplings of the electron.). In the equations for F_2^{NC} and F_3^{NC}, the expressions with P_Z arise from $\gamma - Z$ interference and the expressions with P_Z^2 come from Z-exchange [18].

3.1.4 The Factorization Scale

Consider as an example the case where the quark which interacts with the electron emits a gluon with a transverse momentum k_t with respect to the initial quark. Calculating the cross section it turns out that there is a singularity for the limit $k_t \to 0$. This case has to be taken into account since the virtual photon can distinguish between a quark and a collinear quark-gluon pair carrying the same overall momentum. The key to understanding what is happening is to realize that the limit $k_t \to 0$ corresponds to a long-range ('soft') part of the strong interaction which is not calculable in perturbation theory. The procedure by which this problem is solved is very similar to that of renormalization. [1] First the singularity is made temporarily finite e.g. by introducing a cut-off or a fractional space-time dimension. This regularized divergence of perturbation theory is then removed by absorbing it into the definitions of physical quantities through a *factorization* procedure. This procedure introduces a new dimensional scale, the so-called *factorization scale* μ_f. The parton density functions (PDFs) are quantities that are now defined at a factorization scale:

$$q_0(x) \to q(x, \mu_f),$$

where $q_0(x)$ is the unmeasurable, bare PDF. The distribution $q(x, \mu_f)$ cannot be calculated from first principles in perturbation theory, since it receives contributions from the long-distance (non-perturbative) part of the strong interaction. It can of course be determined from structure function data at any particular scale.

Consider again deep inelastic lepton-hadron scattering. Assume that all partonic cross sections $\hat{\sigma}_i$ for all initial partons i are known at a factorization scale μ_f. Then the *factorization theorem* states that the final cross section σ can be calculated by

$$\sigma = \sum_i \int_0^1 f_{i,h}(\xi, \mu_f) \hat{\sigma}_i(x/\xi, \mu_f). \tag{3.19}$$

The PDF $f_{i,h}$ only depends on the parton i and the hadron h to which this parton belongs. The quantity $\hat{\sigma}_i$ only depends on the partonic interactions and is considered to be independent of the target hadron. When calculated to all

[1] In contrast to renormalization that removes ultraviolet divergences the factorization procedure is introduced because of the so-called infrared divergences.

orders in α_s, σ should not depend on μ_f:

$$\frac{\partial\sigma}{\partial \ln \mu_f} = \mu_f \frac{\partial\sigma}{\partial\mu_f} = 0 \tag{3.20}$$

Such an equation leads to the DGLAP[2] equation [19], an evolution equation for the PDFs:

$$\mu_f \frac{\partial}{\partial\mu_f} \begin{pmatrix} q_i(x,\mu_f) \\ g(x,\mu_f) \end{pmatrix} = \frac{\alpha_s}{2\pi} \sum_{q_j,\bar{q}_j} \int_x^1 \frac{d\xi}{\xi} \begin{pmatrix} P_{q_i q_j}\left(\frac{x}{\xi},\alpha_s\right) & P_{q_i g}\left(\frac{x}{\xi},\alpha_s\right) \\ P_{g q_j}\left(\frac{x}{\xi},\alpha_s\right) & P_{gg}\left(\frac{x}{\xi},\alpha_s\right) \end{pmatrix} \begin{pmatrix} q_j(\xi,\mu_f) \\ g(\xi,\mu_f) \end{pmatrix}, \tag{3.21}$$

where g is the gluon density, q_i is the quark density for flavour i and $\alpha_s \equiv \alpha_s(\mu_f)$. The functions P_{ab}, which are called splitting functions or evolution kernels, are calculable as power series in α_s,

$$\begin{aligned} P_{q_i q_j}(z,\alpha_s) &= \delta_{ij} P_{qq}^{(0)}(z) + \tfrac{\alpha_s}{2\pi} P_{q_i q_j}^{(1)}(z) + \ldots \\ P_{qg}(z,\alpha_s) &= P_{qg}^{(0)}(z) + \tfrac{\alpha_s}{2\pi} P_{qg}^{(1)}(z) + \ldots \\ P_{gq}(z,\alpha_s) &= \delta_{ij} P_{gq}^{(0)}(z) + \tfrac{\alpha_s}{2\pi} P_{gq}^{(1)}(z) + \ldots \\ P_{gg}(z,\alpha_s) &= \delta_{ij} P_{gg}^{(0)}(z) + \tfrac{\alpha_s}{2\pi} P_{gg}^{(1)}(z) + \ldots \end{aligned} \tag{3.22}$$

Note that because of charge conjugation invariance and SU(n_f) flavour symmetry we have

$$\begin{aligned} P_{q_i q_j} &= P_{\bar{q}_i \bar{q}_j} \\ P_{q_i \bar{q}_j} &= P_{\bar{q}_i q_j} \\ P_{q_i g} &= P_{\bar{q}_i g} \equiv P_{qg} \\ P_{g q_i} &= P_{g \bar{q}_i} \equiv P_{gq} \quad . \end{aligned} \tag{3.23}$$

This means that no distinction is needed between quarks and antiquarks and that the splitting functions P_{qg} and P_{gq} are independent of the quark flavour. The evolution kernel $P_{q_i q_j}$ in leading order is zero unless $q_i = q_j$.

The leading-order splitting functions $P_{ab}^{(0)}(z)$ can be interpreted as the probabilities to find a parton a after a branching of parton b. The variable z denotes the fraction of the longitudinal momentum of the parent parton. The transverse momentum of the daughter parton is assumed to be much smaller than μ_f. Both the leading-order and next-to-leading-order contributions to the DGLAP splitting functions have been calculated. The leading-order

[2] Dokshitzer-Gribov-Lipatov-Alterelli-Parisi

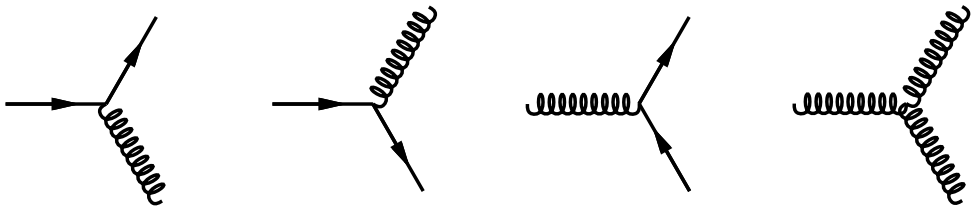

Figure 3.1: Feynman diagrams for the leading-order DGLAP splitting functions $P_{qq}^{(0)}$, $P_{gq}^{(0)}$, $P_{qg}^{(0)}$, and $P_{gg}^{(0)}$.

contributions are

$$\begin{aligned}
P_{qq}^{(0)}(z) &= \tfrac{4}{3}\left[\tfrac{1+z^2}{(1-z)_+} + \tfrac{3}{2}\delta(1-z)\right], \\
P_{qg}^{(0)}(z) &= \tfrac{1}{2}\left[z^2 + (1-z)^2\right], \\
P_{gq}^{(0)}(z) &= \tfrac{4}{3}\left[\tfrac{1+(1-z)^2}{z}\right], \\
P_{gg}^{(0)}(z) &= 6\left[\tfrac{z}{(1-z)_+} + \tfrac{1-z}{z} + z(1-z)\right] + \delta(1-z)\tfrac{33-2n_f}{6},
\end{aligned} \tag{3.24}$$

where the "plus" distribution is defined so that its integral with any sufficiently smooth distribution f is

$$\int_0^1 dz \frac{f(z)}{(1-z)_+} = \int_0^1 dz \frac{f(z) - f(1)}{1-z} \tag{3.25}$$

and

$$\frac{1}{(1-z)_+} = \frac{1}{1-z} \quad \text{for } 0 \leq z < 1 \quad . \tag{3.26}$$

In Fig. 3.1 the corresponding Feynman diagrams are shown.

3.2 Jets

Within perturbative QCD (pQCD), hard partonic interactions can be calculated that occur at very small distance scales. In an experimental environment this view is inevitably clouded by the subsequent long distance showering, by the eventual hadronization of primary quarks and gluons and by detector effects. To understand what is meant by showering consider as an example a scattered quark. This quark can radiate gluons which can subsequently split into quark-antiquark pairs or can radiate another gluon. Thus a cascade is created. (How such cascades are modeled in Monte Carlo programs, will be described in Chapter 4.) These daughter partons generally have only a small transverse energy with respect to the parent parton. Hadronization takes place

to preserve confinement. The quarks and gluons carry colour charge and are thus not observable at a macroscopic scale. The production of colour-singlet hadrons occurs at a scale where α_s is large, so pQCD is no longer applicable and approximate models have to be used (Some of these models will also be explained in Chapter 4.). These models are based on a kind of duality between partons and hadrons, which means that long range processes create a small amount of transverse energy and therefore do not affect the topology of high transverse momentum partons. Finally, the detector records signals (e.g. tracks and energy deposits) from the hadrons. Although its resolution is finite, it can distinguish between groups of particles that are far apart. So in order to keep track of the hard partonic interaction it would be advantageous to group together "particles" (i.e. partons or hadrons or energy deposits) that have a "small distance" with respect to one another and to form observables that have a close relation between the described evolution stages. This is the idea behind "jets".

In order to have a picture of a jet, imagine a collimated spray of particles and consider Fig. 3.3 where a neutral current event measured with the ZEUS detector is displayed. In this event display, two collimated sprays of particles are seen, which are then the two jets in the event.

To lower orders the hard processes that produce jets are rather easy to picture and are shown in Fig.3.2.

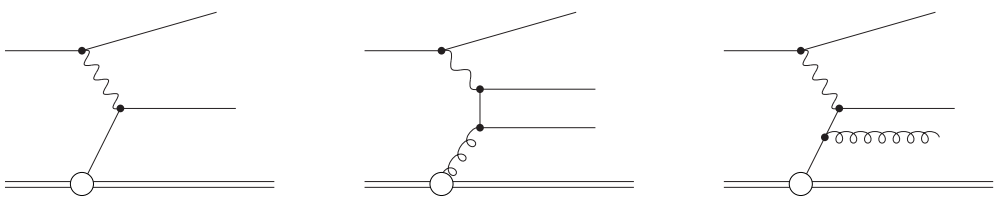

Figure 3.2: Feynman diagrams of the Born process, Boson-Gluon Fusion and QCD-Compton (from left to right).

In Fig. 3.2 on the left the so-called Born process is shown. This process, which has already been introduced in Chapter 2, gives rise to one current jet from the scattered quark and one beam jet from the proton remnant when the jet search is performed in the Laboratory frame. In the middle and on the right two processes of $O(\alpha_s)$ are shown. In Boson-Gluon Fusion (BGF) a gluon from the proton splits into a quark and an antiquark of which one interacts with the vector boson from the positron. In a QCD-Compton process (QCDC) the quark involved in the scattering emits a gluon. Both BGF and QCDC can give rise to two current jets.

Certainly a precise definition is needed for what is called a jet and a jet observable. Such a definition shall be given for the longitudinally invariant k_t-algorithm in the inclusive mode [20, 21]. Consider a reference frame where

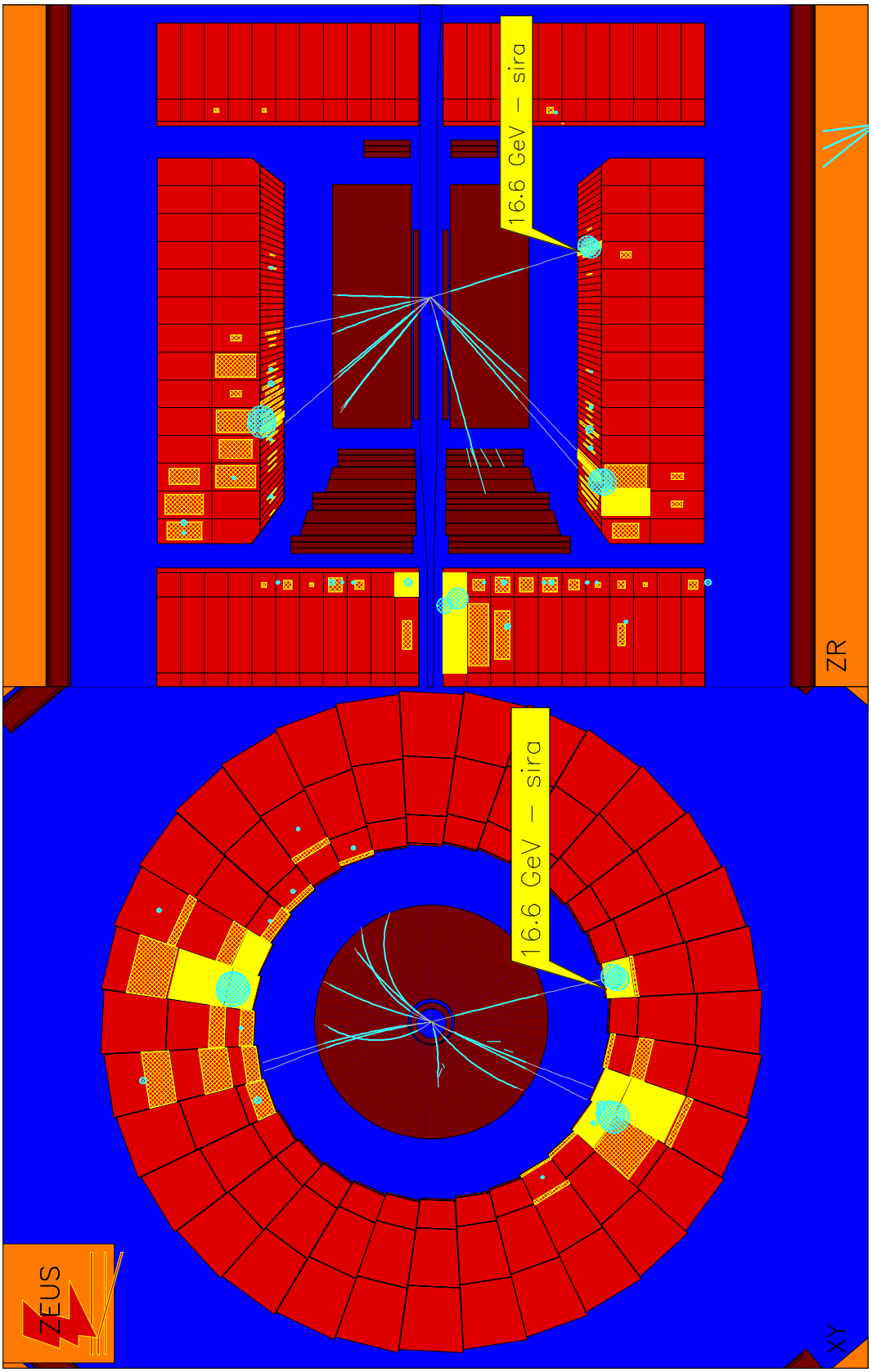

Figure 3.3: Display of a neutral current event with two jets. On the top the event is presented in the (y, z) plane. On the bottom the event is displayed in the (x, y) plane. The inner part of the figures show the tracks of electrically charged particles. The lighter areas in the outer parts of the figures indicate energy deposits in the UCAL. A flag marks the impact point of the scattered positron.

the direction of the incoming proton coincides with the z axis. The hadronic final state of the collision consists of a starting set of "protojets" i with four-momenta p_i^μ. The p_i^μ may be the momenta of quarks and gluons or hadrons or UCAL cells. In all cases their mass $p_i^\mu p_{i\mu}$ is zero. Each protojet is characterized by its azimuthal angle ϕ_i, its pseudorapidity η_i and its transverse energy $E_{t,i}$. Starting with the initial list of protojets, the jet algorithm recursively groups pairs of protojets together to form new protojets. The idea is that protojets with nearly parallel momenta should be joined, so that they will eventually form part of the same jet. The algorithm depends on a parameter R, which was chosen to be one as recommended in [20, 21]. The algorithm begins with a list of protojets and an empty list of completed jets. It proceeds recursively as follows [21]:

1. For each protojet, define
$$d_i = E_{t,i}^2 \tag{3.27}$$
and for each pair of protojets define
$$d_{ij} = \min(E_{t,i}^2, E_{t,j}^2)[(\eta_i - \eta_j)^2 + (\phi_i - \phi_j)^2]/R^2. \tag{3.28}$$

2. Find the smallest of the d_i and d_{ij} and label it $d_{\min}$.

3. If $d_{\min}$ is a d_{ij}, merge protojets i and j into a new protojet k with
$$E_{t,k} = E_{t,i} + E_{t,j} \tag{3.29}$$
and
$$\eta_k = [E_{t,i}\eta_i + E_{t,j}\eta_j]/E_{t,k} \tag{3.30}$$
$$\phi_k = [E_{t,i}\phi_i + E_{t,j}\phi_j]/E_{t,k} \tag{3.31}$$

4. If $d_{\min}$ is a d_i, the corresponding protojet i is "not mergable". Remove it from the list of protojets and add it to the list of jets.

5. Go to step 1.

The procedure continues until there are no more protojets. As it proceeds, it produces a list of jets with successively larger values of $d_i = E_{t,i}^2$.

The algorithm above produces a list containing many jets for each event. However, only the jets with large values of E_t are of interest for this thesis. The jets with smaller E_t are regarded as "minijets" or just random debris from the beam jet.

It is crucial that a jet cross section be "infrared safe". That is, when the cross section is calculated in QCD at the parton level, the cross section must be finite, despite the infrared divergences in the Feynman diagrams. One may differentiate between soft and collinear singularities. In the first case a parton emits another parton with $p^\mu \to 0$. In the other case, a parton splits into a pair of partons with collinear momenta. These situations cause no problem to jet cross sections calculated with the above jet algorithm. If a parton divides

into two partons with collinear momenta, then the algorithm immediately recombines them, producing the same result as if the parton had not divided. Similarly, a parton with a very small energy may be part of a high E_t jet. However, in the limit that its energy tends to zero it does not change the transverse energy or the angle of the jet.

The algorithm introduced above is called a "jet clustering algorithm", which defines jets by successive recombination of pairs of particles in an iterative procedure. Another approach is used in "cone algorithms" which define jets by maximizing the transverse energy flow through a cone of fixed size. The jet clustering algorithms are usually further divided into "exclusive" and "inclusive" algorithms. In e^+e^- annihilation, where the entire final state emerges from the hard process, one typically uses exclusive jet definitions. That is, every particle of the final state is associated with one of the hard jets. In DIS (and in hadron collisions) there is also energy flow associated with the hadron remnant(s). For such a process usually only a fraction of the final state particles is included in the hard jets whereas the rest is not further considered. The algorithm introduced above is an example of such an inclusive jet definition.

In comparison with various other jet definitions, the inclusive longitudinally invariant k_t-algorithm is reported to have the smallest hadronization corrections [22].

For this thesis, the jet search was performed in the Breit frame, which will be defined in the next section. It has been discussed in [23] that in deep inelastic scattering the factorization between the beam fragmentation and the hard process in the calculation of jet cross sections is only given in a special family of reference frames, one of them being the Breit frame.

3.3 The Breit Frame

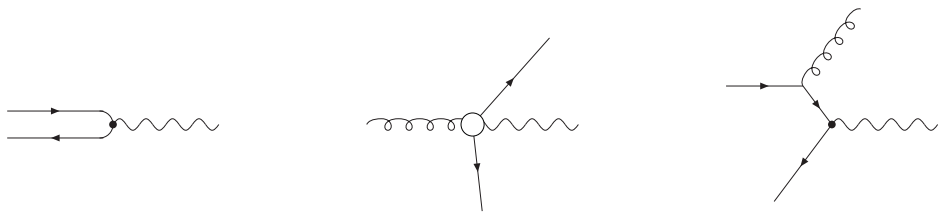

Figure 3.4: Feynman diagrams of the Born process, Boson-Gluon Fusion and QCD-Compton in the Breit frame (from left to right).

The Breit frame is defined by

$$2x\vec{p} + \vec{q} = 0, \tag{3.32}$$

where x is the Bjorken x and $\vec{p}$ and $\vec{q}$ are the three-momenta of the incoming proton and the exchanged virtual boson (γ, Z), respectively. In order to understand, what this definition means for the basic processes, consider Fig. 3.4. In this figure the Feynman diagrams for the Born process, Boson-Gluon Fusion (BGF) and QCD-Compton (QCDC) in the Breit frame are shown. First consider the Born process (diagram on the left). In the Breit frame, the exchanged boson is purely space-like with four-momentum

$$q = (0, 0, 0, -Q) \quad . \tag{3.33}$$

In the Born process the virtual boson is absorbed by the struck quark, which is backscattered with zero transverse momentum. The four-momenta of the struck quark before (p_q) and after ($p_q{}'$) the absorption of the virtual boson are

$$p_q = (Q/2, 0, 0, Q/2) \quad and \quad p_q{}' = (Q/2, 0, 0, -Q/2) \quad . \tag{3.34}$$

The beam jet follows the direction of the initial struck quark. (The proton remnant is not shown in Fig. 3.4 for the sake of simplicity.)

As can be seen from the other two diagrams, the BGF and QCDC processes give rise to two hard jets with opposite transverse momenta. These are processes of $O(\alpha_s)$. It is apparent now that studying the production of jets with high transverse energy in the Breit frame allows to test perturbative QCD.

Up to this point, there remains an arbitrariness in the definition of the x axis in the Breit frame. The direction of the x axis will be defined in the next section.

3.4 The Azimuthal Asymmetry

Jet production in the Breit frame allows, furthermore, to investigate the non-trivial azimuthal dependence predicted by QCD [24–26]. In the Breit frame a z axis along the proton direction can be chosen to define longitudinal and transverse momentum components. The angle that is considered in this section is the azimuthal angle around this axis and with $\phi^{Breit} = 0$ (the direction of the x axis) defined by the scattered positron, which together with the incoming one forms the positron scattering plane shown in Fig. 3.5. The jet production plane is then defined by the exchanged virtual boson and the outgoing jet (which is assumed to have transverse momentum). The angle between these two planes is regarded as the azimuthal angle of the jet.

Asymmetries in the ϕ^{Breit} distribution, i.e. terms proportional to $\cos\phi^{Breit}$ and $\cos 2\phi^{Breit}$ are expected whenever a non-zero transverse momentum, in the Breit frame, is present. Both non-perturbative and perturbative QCD effects are regarded as the reasons for these asymmetries. The azimuthal dependence of parton production has the form

$$\frac{d\sigma}{d\phi^{Breit}} = A + B\cos\phi^{Breit} + C\cos 2\phi^{Breit}. \tag{3.35}$$

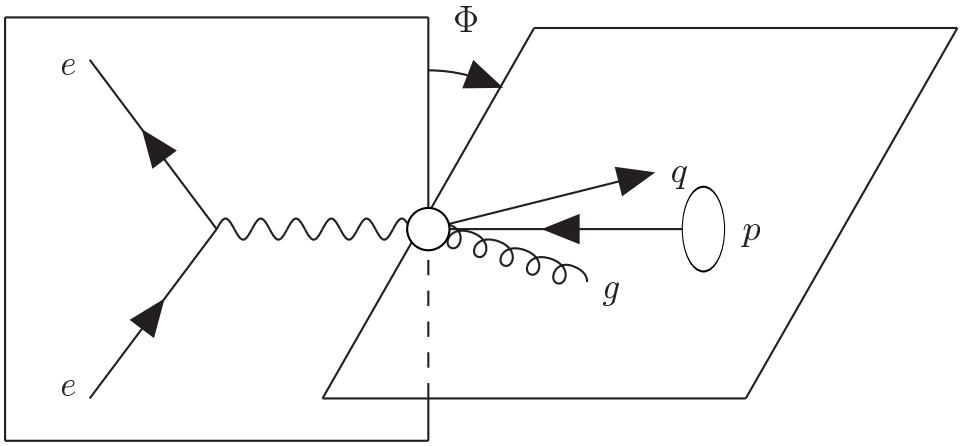

Figure 3.5: The definition of the azimuthal angle in the Breit frame.

The coefficients B and C depend on the helicity of the final-state parton(s), partonic transverse momenta and on colour coherence [27]. The $\cos 2\phi^{Breit}$ term is expected from interference of amplitudes arising from the $+1$ and -1 helicity components of the transversely-polarised part of the exchanged boson, whereas transverse/longitudinal interference gives rise to the $\cos \phi^{Breit}$ term.

The small intrinsic transverse momentum of a quark in the proton is the reason for the so-called non-perturbative asymmetry. However, this effect is expected not to be observable when the transverse momenta of the jets and Q^2 are high.

In contrast, the asymmetry associated with leading-order terms in perturbative QCD calculations, the perturbative asymmetry, is weakly dependent on Q^2 and persists at high transverse momenta. The perturbative QCD contribution to the coefficients B and C is large at leading order in α_s. The BGF process is the dominant contribution to the $\cos 2\phi^{Breit}$ term, while the QCDC contribution dominates the $\cos \phi^{Breit}$ term. In order to observe the $\cos \phi^{Breit}$ asymmetry it would be necessary to differentiate between the quark and the gluon-initiated jets, since the quark and the gluon have opposite distributions that cancel the effect if added. In the BGF process there is symmetry between the quark and the antiquark such that their distributions can simply be added. In fact, this is confirmed in Monte Carlo studies. In Fig. 3.6 the ϕ^{Breit} distribution is shown for parton jets (already applying all the selection criteria of Chapter 5). The distribution for QCDC is flat, since no effort was made to seperate quark and gluon-induced jets. The distribution for BGF has the form

$$\frac{d\sigma}{d\phi^{Breit}} = A' + B' \cos 2\phi^{Breit}. \tag{3.36}$$

It is such a ϕ^{Breit} distribution that will be measured in this thesis. In order to achieve this, no cut should be applied to the jets in the Laboratory frame;

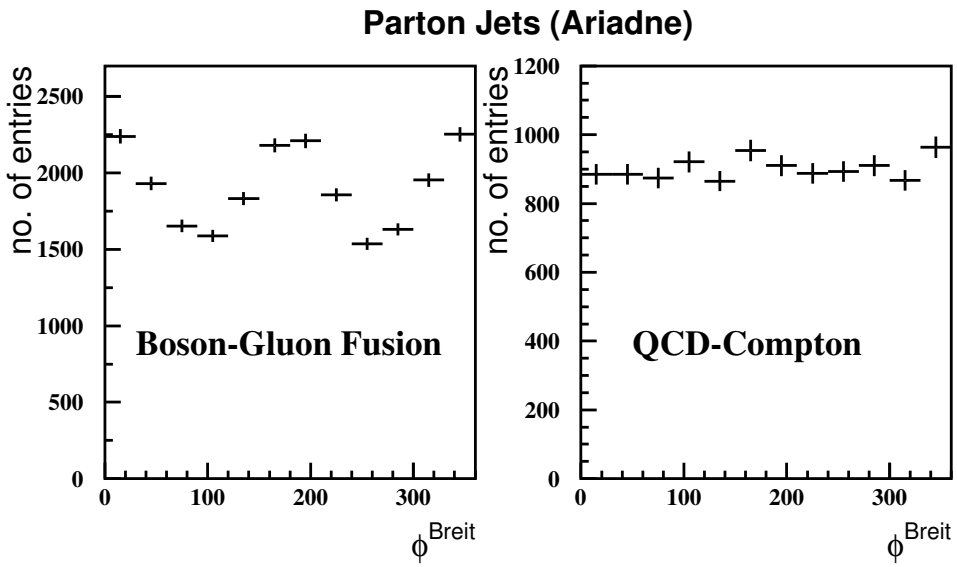

Figure 3.6: Different distributions of ϕ^{Breit} for Boson-Gluon Fusion and QCD-Compton obtained with parton jets.

otherwise the azimuthal distribution would be dominated by kinematic effects [28].

Chapter 4

Monte Carlo Simulation

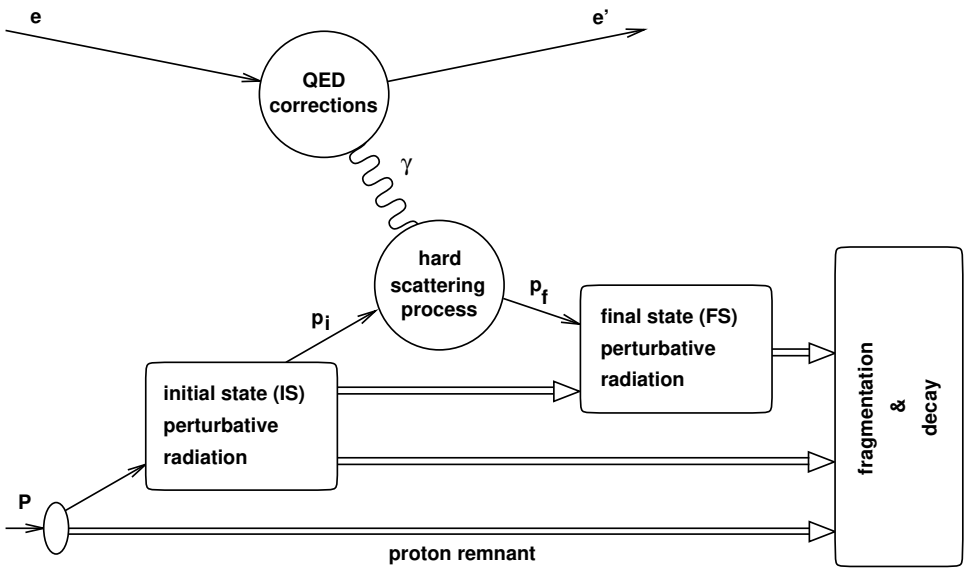

Figure 4.1: The various steps of an event generator.

For this thesis Monte Carlo programs are needed to produce theoretical predictions and to relate the measured data to these predictions. For the first purpose a next-to-leading-order (NLO) QCD program is used, in which calculations are performed in terms of quarks and gluons (parton level). For the other purpose, so-called event generators are taken into account. Fig. 4.1 shows typical features of an event generator for deep inelastic positron-proton scattering. Such a Monte Carlo program usually starts with generating a hard scattering process up to leading order in α_s. QED corrections are taken into account that may affect the incoming or outgoing positron and the intermediate photon. The effects of orders higher than $O(\alpha_s)$ are simulated by models of QCD cascades. Such cascades may evolve before and after the virtual boson vertex. Furthermore, the quarks and gluons fragment into colour-singlet

hadrons of which some decay into lighter particles. Thus a list of final state particles and their four-momenta is obtained defining the hadron level. In order to relate these particles to a measurement the detector has to be simulated. Thus an event sample is created at the so-called detector level, which can be compared to the measured data.

In this chapter a survey will be given of the Monte Carlo programs used for this thesis and the main principles of these simulations will be explained.

4.1 Leading-order MC Simulation

4.1.1 The Parton Shower Model

The parton shower model is derived from the "leading logarithm approximation" of perturbative QCD from which the DGLAP equations are obtained. It makes iterative use of the branching processes $q \rightarrow qg$, $g \rightarrow gg$ and $g \rightarrow q\bar{q}$ for which the probabilities are considered to be the first-order splitting functions $P_{ab}^{(0)}$ as discussed in Chapter 3. In DIS the quark struck by the electroweak boson can emit partons before and after the boson vertex giving rise to an initial and final state parton shower, respectively. Consider first a parton in the incoming proton with a virtuality close to mass-shell. In an initial branching one emerging parton has a space-like virtuality ($m^2 < 0$) while the other parton is on-shell or has a time-like virtuality ($m^2 > 0$). In a further splitting the space-like parton can give rise to a parton with even higher space-like virtuality. This so-called initial state space-like shower results in a space-like quark which interacts with the electroweak boson. After the boson vertex an outgoing quark is either on-shell or has a time-like virtuality. In the latter case it gives rise to a so-called time-like shower with daughter partons of decreasing off-shell masses. This shower continues until all outgoing partons are (essentially) on-shell. Any parton from the inial state shower with a time-like virtuality will develop similarly.

To understand how such a procedure is implemented in a Monte Carlo program, consider first the final state time-like shower. Let the variable t be the virtuality, i.e. $t = p^2 = m^2$. A splitting process $a \rightarrow bc$ shall be considered with the splitting function $P_{a\rightarrow bc}$. This function depends on the energy fraction z with

$$z = \frac{E_b}{E_a} = 1 - \frac{E_c}{E_a} \quad .$$

The so-called Sudakov form factor for the parton a is defined by

$$S_a(t) = \exp\left(- \int_{t_{\min}}^{t} dt' \int_{z_{\min}(t')}^{z_{\max}(t')} dz \frac{\alpha_s}{2\pi} P_{a\rightarrow bc}(z) \right) \quad , \tag{4.1}$$

where $z_{\min}$ and $z_{\max}$ are infra-red cut-offs beyond which branchings are classified to be unresolvable, since they would involve the emission of an undetectable soft parton. The Sudakov form factor can be interpreted as the probability that the parton a with the virtuality t evolves to the cut-off virtuality $t_{\min}$

without branching. (The parameter $t_{\min}$ is the virtuality where the time-like shower is supposed to come to an end.) The advantage of a Sudakov form factor is that it can be tabulated once $t_{\min}$, $z_{\min}$ and $z_{\max}$ have been chosen. Now assume that for a parton a the virtuality t_1 and the energy fraction z_1 have been determined from a previous step or as initial condition. The problem for the Monte Carlo program is then to determine the values (t_2, z_2) for the next step. The probability for parton a to evolve to a virtuality t_2 without branching is

$$P_{\text{no emission}} = \frac{S_a(t_1)}{S_a(t_2)} \quad . \tag{4.2}$$

The value of t_2 is generated with the correct probability distribution by solving the equation

$$S_a(t_2) = \frac{S_a(t_1)}{R} \quad , \tag{4.3}$$

where R is a random number from the interval $[0, 1]$. In the case $t_2 < t_{\min}$, i.e. $R < S_a(t_1)$, the algorithm decides that the parton a does not branch any more keeping the virtuality t_1. In the case $t_2 > t_{\min}$ the energy fraction $z = z_2/z_1$ has to be generated. This can be achieved by solving the equation

$$\int_{z_{\min}}^{z_2/z_1} dz \frac{\alpha_s}{2\pi} P_{a\to bc}(z) = R' \int_{z_{\min}}^{z_{\max}} dz \frac{\alpha_s}{2\pi} P_{a\to bc}(z) \quad , \tag{4.4}$$

where R' is another random number from the interval $[0, 1]$.

The procedure described in the paragraph above is known as forward evolution. In order to make the Monte Carlo program more efficient a so-called backward evolution is usually used for the initial state parton shower. The algorithm is very similar to the one above with the difference that also the parton density functions of the proton are involved (see e.g. [12]).

An item which has not been considered so far is coherence which arises from quantum mechanical interference. In the parton shower approach there is interference between the initial and final state shower and there is interference between subsequent partons in a shower [29]. The latter effect is approximately accounted for by imposing "angular ordering". This means that the opening (polar) angles in a shower decrease, $\theta_{i+1} < \theta_i$. A parton shower program where this is taken into account is from Marchesini and Webber [30]. Consider again the branching $a \to bc$. Again z is the energy fraction $E_b = zE_a$. The maximal value for the parameter t for the daughter partons b and c is now set equal to

$$E_b^2 \xi_a \quad \text{and} \quad E_c^2 \xi_a \quad \text{with } \xi_a = \frac{p_b \cdot p_c}{E_b E_a} \approx 1 - \cos\theta \quad , \tag{4.5}$$

where θ is the polar angle between the daughter partons. In general this means that the daughter partons may split with

$$\xi_b < \xi_a \quad \text{and} \quad \xi_c < \xi_a \quad . \tag{4.6}$$

The use of the leading logarithm approximation has the consequence that the emission of soft partons or of partons with a direction close to that of the

parent parton are well described. On the other hand, the wide angle emission of a hard parton is not so well taken into account. That is the reason why such a process is usually calculated from the exact matrix element (ME) and the parton shower (PS) evolves as a kind of correction to the matrix element. Such an approach is denoted with the abbreviation "MEPS".

4.1.2 The Colour Dipole Model

The colour dipole model (CDM) [31] is another approach to simulate QCD cascades. It makes use of the fact that the radiation of a gluon from a $q\bar{q}$ from e^+e^- annihilation can be regarded as radiation from a colour dipole between the q and the $\bar{q}$. To a good approximation the emission of a second softer gluon can be considered as coming from two independent dipoles, one between the q and the g, the other between the g and the $\bar{q}$. The radiation of a third even softer gluon then comes from three independent dipoles etc..

For DIS, the first dipole extends beween the struck quark and the proton remnant. (No distinction is made between initial and final state QCD radiation as is done in the parton shower approach.) To see how the colour dipole model is implemented in the Monte Carlo program ARIADNE [32–34] for DIS, some definitions need to be made. First of all, the gluons are generated in the Hadronic centre-of-mass system (HCM). The HCM is defined as the centre-of-mass system of the virtual boson and the incoming proton. The direction of the z axis is the direction of the proton beam. The HCM can be obtained from the Breit system by a longitudinal boost. Furthermore, in the following light-cone momenta are used. They can be derived from the usual components of a four-momentum $k^\mu = (k^0, k^1, k^2, k^3)$ by the definitions

$$k_\pm = k^0 \mp k^3 \quad \text{and} \quad \vec{k}_t = (k^1, k^2) \quad . \tag{4.7}$$

Another quantity that is needed to be defined is the rapidity, y,

$$y = \frac{1}{2} \ln \frac{k^0 + k^3}{k^0 - k^3} \quad . \tag{4.8}$$

Given are the momentum of the incoming proton in the HCM (in light-cone components) $(0, P_-, \vec{0})$ and the momentum of the virtual boson $(Q_+, -xP_-, \vec{0})$, where x denotes the Bjorken x of the event. For the emission of a gluon with momentum $(k_+, k_-, \vec{k}_t)$ the phace space is limited by

$$k_+ = k_t e^{-y} < Q_+ \quad \text{and} \quad k_- = k_t e^{y} < P_- \quad . \tag{4.9}$$

The quantities that are generated at each step in the Monte Carlo program are k_t and y. By choice of an appropriate Sudakov form factor the k_t decreases in each step, i.e. $k_{t,i+1} < k_{t,i}$. If the emissions are reordered in y, the order in k_t is in general lost [29]. Such a property is desirable for certain analyses like [35].

For DIS, there is an important further item to be considered. It has to be taken into account that the proton remnant is an extended object with

a transverse extension of $1/\mu \approx 1$ fm. Therefore a gluon should only have access to a fraction of the remnant's negative light-cone momentum. It is a well known fact, that the emission of short wavelengths are suppressed for an extended antenna. Only a fraction proportional to the emitted wavelength $\lambda \propto 1/k_t$ should be participating in the emission. This consideration leads to the condition

$$k_t e^y < \left(\frac{\mu}{k_t}\right)^{\alpha} P_- \quad , \tag{4.10}$$

where the parameter α is called the dimensionality of the remnant.

However, it turned out that ARIADNE gave a rather poor description of DIS data at high values of Q^2. During the HERA Monte Carlo Workshop Leif Lönnblad made a suggestion how to overcome this deficiency [34]. He argued, that in a DIS event a fraction x of the proton momentum has already been localized and that this fraction should be available for gluon emission. Therefore the above condition should be changed to

$$k_t e^y < \max\left(x, \left(\frac{\mu}{k_t}\right)^{\alpha}\right) P_- \quad . \tag{4.11}$$

Indeed, it was reported in the workshop that this modification improves the situation considerably.

This modification has been implemented in the ARIADNE program by Enrico Tassi and such a program has been used for this thesis. So when in the following it is said that an event sample has been generated using ARIADNE for the QCD cascades it is always a modified version with the above extension of phase space.

4.1.3 String Fragmentation

The Lund String Fragmentation Model [14,36] describes in a stochastic manner the hadronization of coloured objects like quark and gluons. In order to understand the principle, consider a typical e^+e^- annihilation event where in the final state a quark, q, and an antiquark, $\bar{q}$, are moving apart back-to-back in the center-of-mass system. Because of the three-gluon coupling the colour flux lines that connect the q and the $\bar{q}$ are concentrated in a narrow tube with constant tension

$$\kappa \simeq 1 \text{ GeV/fm} \simeq 0.2 \text{ GeV}^2 \quad . \tag{4.12}$$

(The value for κ is taken from Regge phenomenology, heavy quarkonium spectroscopy and lattice QCD.) Within the tube new $q\bar{q}$ pairs may be created and the original tube is seperated in many small pieces. This breaking continues until the single tube pieces have an energy comparable to the energy of final state hadrons in an experiment. A hadron is formed out of a q and the adjacent $\bar{q}$. (The model also takes into account the breaking of the tube into diquark-antidiquark pairs to account for the production of baryons.)

As experimental observation indicates, the final state hadrons are aligned on the original $q\bar{q}$ axis having a transverse momentum of the order of 400 MeV.

Therefore the transverse dimensions shall be first neglected which results in a model with $1+1$ dimensions. The space-time vector is $x^\mu = (t, x)$ and the energy-momentum vector, $p^\mu = (E, p)$. The colour flux tube from above now becomes a string with no transverse size. Consider first a bound $q\bar{q}$ state. The two particles are assumed to be massless and to move always with the speed of light. Since the force between them is constant, the equation of motion is

$$dp/dt = \pm\kappa \quad , \tag{4.13}$$

where the sign depends on which end of the string is considered. In the beginning, the two particles move apart losing momentum with increasing distance. At the time when all energy is in the connecting string the direction of motion turns. The momenta of the particles increase and their distance becomes smaller. Finally they meet and change sides and the whole process is repeated. This oscillation is called a "yo-yo mode". (The description of the yo-yo mode has been in the center-of-mass system.) Note, that the equation of motion is invariant under a (longitudinal) boost.

Consider the initial quark q_0 moving to the right and the initial antiquark $\bar{q}_0$ moving to the left. Let n $q\bar{q}$ be created at the space-time points (t_i, x_i) starting from the right-hand side. It is assumed that all breaks take place in the first expanding phase of the yo-yo modes. Thus all q_i are moving left and all $\bar{q}_i$ are moving to the right. The momentum and energy of the ith hadron $q_{i-1}\bar{q}_i$ are

$$p_i = \kappa(t_{i-1} - t_i) \quad , \quad E_i = \kappa(x_{i-1} - x_i) \quad . \tag{4.14}$$

Note, that in order to obtain the correct hadron mass m_i the point (t_i, x_i) must lie on a hyperbola given by

$$(x_{i-1} - x_i)^2 - (t_{i-1} - t_i)^2 = m_i^2/\kappa^2 \quad . \tag{4.15}$$

The procedure to generate the break-points (t_i, x_i) is conveniently described with light-cone coordinates $x^\pm = t \pm x$. It is assumed that the $(i-1)$ break-point has already been found. The next break in the x^+ direction is

$$\Delta x^+ \equiv (x^+_{i-1} - x^+_i) = z_i x^+_{i-1}, \quad 0 \le z_i \le 1 \quad , \tag{4.16}$$

where z_i is generated with a probability function $f(z)$. The mass m_i then fixes the step in the x^- direction

$$\Delta x^- \equiv (x^-_{i-1} - x^-_i) = \frac{-m_i^2}{\kappa^2 \Delta x^+} \quad . \tag{4.17}$$

The boundary conditions are

$$x^+_0 = 2E_0/\kappa, \; x^-_0 = 0 \quad \text{and} \quad x^+_{n+1} = 0, \; x^-_{n+1} = 2\bar{E}_0/\kappa \quad , \tag{4.18}$$

where E_0 and $\bar{E}_0$ are the energies of q_0 and $\bar{q}_0$. Instead of generating the break-point from right to left, a slightly different approach is used in the Lund model. Each new step is with equal probability taken from the right or the

left. When the remaining mass-squared is about 5 GeV^2 a final $q\bar{q}$ is generated for the last two hadrons. The probability function $f(z)$ is of the form

$$f_{\alpha\beta}(z) = N_{\alpha\beta} z^{a_\alpha - a_\beta - 1}(1-z)^{a_\beta} \quad , \tag{4.19}$$

where $N_{\alpha\beta}$ is a normalization constant and α and β refer to the flavours of the quark and the antiquark constituting a hadron.

The relative probabilities for the different flavours are chosen to be

$$u\bar{u} : d\bar{d} : s\bar{s} : c\bar{c} \simeq 1 : 1 : \frac{1}{3} : 10^{-11} \quad . \tag{4.20}$$

This means that quarks heavier than the s quark are in general never produced during the soft hadronization process. The transverse momentum of a hadron, p_t, is generated with a probability given by a Gaussian distribution

$$\frac{d\sigma}{dp_t^2} \propto \exp(-bp_t^2) \quad , \tag{4.21}$$

where b is another tunable parameter. Everywhere the mass of a hadron occured so far, it has to be replaced by the so-called transverse mass

$$m_t = \sqrt{m^2 + p_t^2} \quad . \tag{4.22}$$

Since the gluon carries both colour and anticolour, it is regarded as a "kink" on a string connecting a quark and an antiquark. This picture leads to a suppression of hadron production in the direction opposite to the gluon's direction of motion. This "string-effect" has actually been observed in experiment [14].

4.1.4 Cluster Fragmentation

According to the idea of "preconfinement", colour connected partons tend to be close in phase space towards the end of the perturbative phase. This property is the theoretical basis of the cluster fragmentation model [29]. In the following the model as it is implemented in the Monte Carlo program Herwig will be described [30,37,38].

At the beginning of the hadronization phase, the final state gluons are split non-perturbatively in $q\bar{q}$ pairs. Then a quark is combined with an adjacent antiquark to form a colour-singlet cluster. (To decide what is adjacent the so-called "planar approximation" is used , see e.g. [12]). If the cluster is too light to decay into two hadrons, it produces the lightest hadron with its flavour content. If its mass does not have the appropriate value it is shifted, exchanging momentum with an adjacent cluster in the jet. For the majority of the clusters, the procedure is the following. For a $q_1\bar{q}_2$ cluster a $q_3\bar{q}_3$ pair is chosen. Here q can be a quark or an antidiquark. Similarly, $\bar{q}$ means an antiquark or a diquark. The resulting decay products are $q_1\bar{q}_3$ and $\bar{q}_2 q_3$. The flavour q_3 is chosen among the possibilities u, d, s, c, $\bar{u}\bar{u}$, $\bar{u}\bar{d}$,, $\bar{u}\bar{s}$, $\bar{d}\bar{d}$, $\bar{d}\bar{s}$ and $\bar{s}\bar{s}$. Choices that would result in a diquark-antidiquark particle are rejected. The pairs $q_1\bar{q}_3$

and $\bar{q}_2 q_3$ are associated with hadrons of this flavour content. For mesons there is a choice between the pseudoscalar (0^-), vector (1^+), pseudovector (1^-) and tensor (2^+) multiplets, for baryons between the "octet" ($1/2^+$) and "decuplet" ($3/2^+$) ones. For each chosen combination there is a weight equal to the density of states

$$(2s_1 + 1) \cdot (2s_2 + 1) \cdot (2p^*/m) \quad , \tag{4.23}$$

where s_1 and s_2 are the spins of the hadrons, p^* is the common momentum in the rest frame of the cluster and m is the mass of the cluster. The density of states is compared to the maximum density multiplied by a random number. If it is smaller, q_3 is rejected and the procedure is repeated.

In the rare case, where the mass of a cluster is too large for the isotropic decay into two hadrons, a fission procedure is used to produce subclusters. A flavour q_3 is generated with equal probabilities for u, d and s. The subclusters $q_1\bar{q}_3$ and $\bar{q}_2 q_3$ move in the direction of the original q_1 and $\bar{q}_2$. For each subcluster a mass is chosen with a spectrum M^{P_c}, where P_c is a tunable parameter. Kinematically impossible choices are rejected. The fission procedure continues, until all subclusters can decay into two hadrons.

4.1.5 QED Corrections

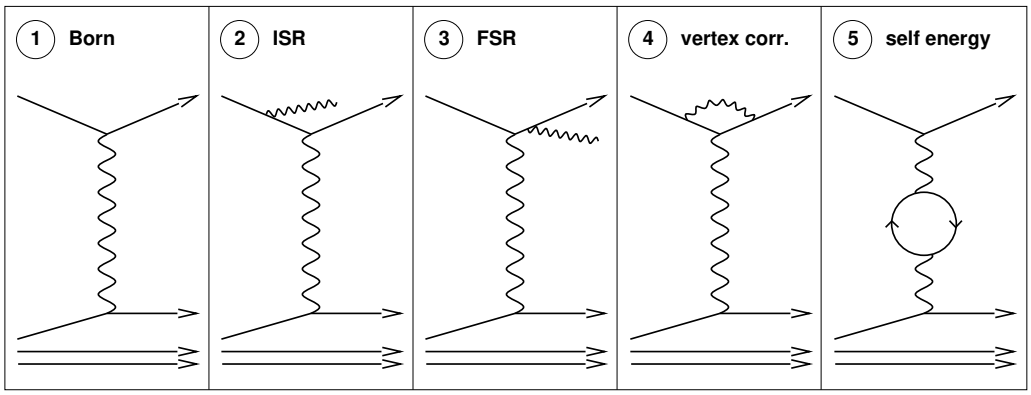

Figure 4.2: Feynman diagrams for QED corrections to the Born process.

In order to have a realistic Monte Carlo simulation of the measured data, radiative QED corrections have also to be taken into account. Fig. 4.2 shows the relevant Feynman diagrams of order α, where α is the electromagnetic coupling constant. Two of these diagrams can give rise to a change in the event topology: initial and final state radiation (ISR and FSR). For this thesis the Monte Carlo program DJANGOH [39–41] was used. It is an interface of the programs HERACLES [42] and LEPTO [43]. In HERACLES the leading logarithm approximation (LLA) of QED is applied, whereas LEPTO uses the LLA of QCD to simulate parton showers. The LLA has the advantage that

corrections of QED and QCD can be factorized, i.e. two independent programs can be used for these purposes. The program HERACLES first determines a cut-off for the photon's energy depending on the selected phase space. Then it decides whether the event is an ISR, FSR or a so-called non-radiative event. (This distinction can only be made in the LLA.) In HERACLES the complete set of one-loop weak corrections is also taken into account.

4.1.6 The Detector Simulation

After an event has been generated the response of the detector to the final state particles has to be simulated. The detector simulation for ZEUS is the program MOZART [1] which is based on the CERN program package GEANT [44]. It includes all the knowledge on the geometry, calibration, resolution etc. of the various components. For the simulation of the UCAL so-called shower terminators are used. These algorithms prevent the simulation of every low-energy particle in a shower which makes the detector simulation faster by a factor of about 15. The trigger is simulated by the program ZGANA.

4.1.7 The Used Event Generators

For this thesis Monte Carlo event samples have been generated with DJANGOH (version 1.1). This Monte Carlo Program uses the Lund string model for the hadronization as implemented in JETSET [45]. For two samples the QCD cascades were simulated by LEPTO using a parton shower model. Alternatively in DJANGOH the QCD cascades can be generated by ARIADNE. To distinguish the samples the labels "Lepto" and "Ariadne" will be used. For both Lepto and Ariadne two samples were generated: One sample with ISR, FSR and a running electromagnetic coupling constant α. This type of sample has gone through the detector simulation. The other sample was generated without ISR, FSR and with a fixed value of α. Since this type of sample was only needed for corrections on generator level, it did not go through the detector simulation. The former type is referred to as "with radiation", the latter as "without radiation". It would have been desirable to generate events without the effect of the Z^0 boson, since the NLO Monte Carlo program used for this thesis does not take the exchange of this particle into account. Unfortunately, this option is not provided in DJANGOH. However, the number of events with $Q^2 > 5000$ GeV^2 is rather small (in the order of 100), so the statistical error is expected to be larger than the effect of the Z^0 boson.

The (integrated) luminosity for the Lepto sample with radiation is 88.5 pb^{-1} and 109 pb^{-1} for the sample without radiation. The Ariadne sample with (without) radiation has a luminosity of 88.5 pb^{-1} (86.8 pb^{-1}). The luminosity, L, has been determined according to

$$L = \frac{N}{\sigma} \quad , \tag{4.24}$$

where N is the number of events and σ is the cross section.

Furthermore, an event sample has been generated with HERWIG (version 5.9). This sample was only used to determine correction factors for the hadronization. The luminosity is 137.4 pb^{-1}.

4.2 Next-to-leading-order MC Simulation

4.2.1 The Phase Space Slicing Method

[46] An n-jet cross section can be separated into several parts. The cross section, $\sigma^{\mathrm{LO}}_{n\ \mathrm{partons}}$, is the tree level contribution at leading order with exactly n partons in the final state. Since all n partons have been resolved by an infrared safe jet algorithm, this cross section should not have soft and collinear divergences. Furthermore there is the contribution from $\sigma^{\mathrm{NLO}}_{n\ \mathrm{partons}}$ where there are n partons in the final state with one-loop corrections. Finally there is $\sigma^{\mathrm{LO}}_{n+1\ \mathrm{partons}}$ from a final state where two partons are not resolved by the jet algorithm. The latter two contributions are divergent. For the phase space slicing method the theoretical parameter s_{min} is introduced and the distance between two partons i and j is defined by their four-momenta

$$s_{ij} = 2p_i p_j \quad . \tag{4.25}$$

For the $(n+1)$-final state parton matrix element soft and collinear approximations are used for the phase space region inside the cone $s_{ij} < s_{\mathrm{min}}$. The soft and/or collinear parton is then integrated analytically and added to $\sigma^{\mathrm{NLO}}_{n\ \mathrm{partons}}$. In general this new term is negative and increases in magnitude logarithmically as s_{min} becomes smaller. The remaining part of $\sigma^{\mathrm{LO}}_{n+1\ \mathrm{partons}}$ with $s_{ij} > s_{\mathrm{min}}$ for every pair of partons can be evaluated using Monte Carlo methods. The logarithmic growth of this contribution with s_{min} is exactly cancelled with the logarithmic divergence of the new $\sigma^{\mathrm{NLO}}_{n\ \mathrm{partons}}$. (For lepton-hadron scattering an additional term appears to take into account the collinear splitting of an initial state parton. This complication is not treated to make the procedure more transparent.)

The idea behind the phase space slicing method is to assume that s_{min} is small enough, so the approximation of the $(n+1)$-final state parton matrix element within the s_{min}-cone is valid. Furthermore, in this case a soft and collinear safe jet algorithm could not resolve a parton pair with $s_{ij} < s_{\mathrm{min}}$. The Monte Carlo program could then provide the four-momenta of every relevant particle and it would be flexible enough to implement any jet algorithm and arbitrary acceptance cuts. For this thesis, no NLO Monte Carlo program has been used that applies the phase space slicing method.

4.2.2 The Subtraction Method

[47] Suppose again that a n-jet cross section is to be calculated. As in the previous section, no difficulty arises from the leading-order contribution of n

partons. The NLO part can be decomposed in the following way:

$$\sigma^{NLO} = \int_{n+1} d\sigma^R + \int_n \left[d\sigma^V + d\sigma^C \right] \quad , \tag{4.26}$$

where $d\sigma^R$ is called the real part with $n+1$ final state partons and $d\sigma^V$ is the virtual part with n partons and one-loop corrections. The contribution $d\sigma^C$ is a counterterm arising from a collinear divergence in the initial state. Each part in the equation above is divergent, though their sum is finite. The divergences can be regularized in $d = 4 - 2\epsilon$ dimensions giving rise to singularities in $1/\epsilon$. For the subtraction method the following exact identity is used:

$$\sigma^{NLO} = \int_{n+1} \left[d\sigma^R - d\sigma^A \right] + \int_{n+1} d\sigma^A + \int_n \left[d\sigma^V + d\sigma^C \right] \tag{4.27}$$

In this expression an "approximate" cross section $d\sigma^A$ has been introduced. On the one hand, this cross section must have the same singular behaviour in d dimensions as $d\sigma^R$. Thus the limit $\epsilon \to 0$ can be performed under the integral sign. On the other hand, it must be possible to integrate $d\sigma^A$ in the subspace of the parton that leads to a divergence. The result of this integration must have singularities in $1/\epsilon$ that cancel with those of $d\sigma^V$ and $d\sigma^C$. Thus the equation above can be rewritten as

$$\sigma^{NLO} = \int_{n+1} \left[\left(d\sigma^R \right)_{\epsilon=0} - \left(d\sigma^A \right)_{\epsilon=0} \right] + \int_n \left[d\sigma^V + d\sigma^C + \int_1 d\sigma^A \right]_{\epsilon=0} \quad . \tag{4.28}$$

Note that the remaining integrations can be done in four dimensions where Monte Carlo techniques may be applied.

For this thesis the NLO Monte Carlo program DISENT [48] has been used that applies the subtraction method. During the HERA Monte Carlo Workshop it was reported [49] that the agreement of DISENT with DISASTER++ [50] is better than 2%. DISASTER++ also uses the subtraction method but with different expressions for $d\sigma^A$. (Two NLO programs that apply the phase space slicing method were reported to give either 5-8% lower cross sections or unstable results with respect to the cut-off parameter.)

Chapter 5

Event Selection

This analysis is based on the data taken by the ZEUS Collaboration in the years 1996 and 1997 corresponding to an integrated luminosity of about 38.6 pb^{-1}.

5.1 Positron Reconstruction

To acurately reconstruct a neutral current event a scattered positron is found (predominantly) in the uranium calorimeter. Therefore the identification of the final state positron in the total final state is of vital importance for the whole analysis. For this purpose an algorithm, called an electron finder, is used. In general the algorithms used within the ZEUS Collaboration consist of the following steps [51]:

- First the energy deposits in the UCAL are grouped into objects. These objects can be determined with a "cone", "cluster" or "island" algorithm. The cone algorithm is very similar to a cone jet finding algorithm. The cluster algorithm looks for isolated clusters of cells with energy deposits. The island algorithm assigns the energy of each cell to a direct neighbour with higher energy until no further assignment is possible. Fig. 5.1 illustrates the difference between these three possibilities.

- In the next step the algorithm seperates electromagnetic and hadronic shower objects. For example it makes use of the fact that an electromagnetic shower generally starts immediately after the impact of the particle in the calorimeter and has a much smaller lateral und longitudinal extension. In this step the algorithm does not differentiate between electrons, positrons and photons.

- Depending on the algorithm, the object with the highest energy, the lowest Q^2 or the highest p_t is selected as the scattered positron.

The quality of an electron finder is determined with Monte Carlo simulations and is expressed in terms of the efficiency and purity. The efficiency is defined as the fraction of events generated in a certain region of phase space with the electron found to all events generated in that region of phase space.

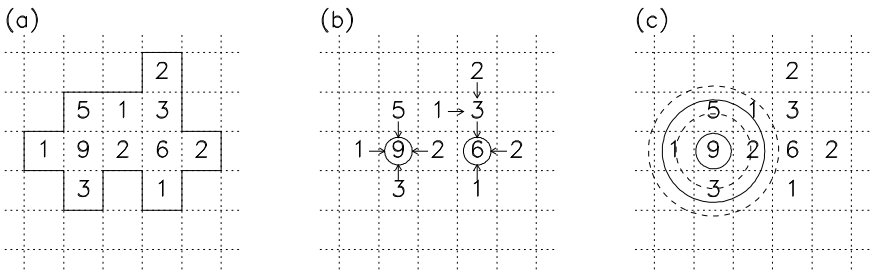

Figure 5.1: Illustration of different methods for electron identification: (a) cluster, (b) island and (c) cone algorithm. The grid is supposed to represent a part of the UCAL. The numbers refer to the magnitude of the energy deposit.

The purity is defined as the fraction of events generated and reconstructed in a kinematic region to the number of reconstructed events including background events. The efficiency and purity of any electron finding algorithm become worse at low electron energies. One reason for this is that low energy electrons can shower quite easily and cause a wider shower. Thus, a minimum energy of the reconstructed electron is generally required. There are also methods to ensure that the efficiency of an electron finder is the same for data and Monte Carlo. For an example see [52].

The electron finder used in this analysis is SINISTRA95 [53] which uses a neural network technique to find electrons. The neural network was trained on Monte Carlo samples of deep inelastic scattering events. SINISTRA95 calculates the probability P_{Si} for an island of calorimeter cells to be an electron using the shower profiles in the transverse and longitudinal direction. In those cases where more than one electron candidate was found a decision is made by the routine FINDIS96. In this analysis FINDIS96 option 5 was used which selects the electron candidate with the highest probability P_{Si}. In those cases where the electron candidate was in an angular region with a good CTD acceptance, taking the vertex position into account, a track match was required. A track is matched to an electron if the distance of closest approach from the electron impact point on the calorimeter surface to the track extrapolated from the event vertex into the direction of the electron is less than 20 cm [52].

In this analysis the minimum probability P_{Si} for a candidate to be selected as the scattered positron was 0.9. In the case where more than one track was found with a distance of closest approach less than 10 cm and a transverse momentum greater than 5 GeV, the track with the smallest distance was taken. In case of a successful track search the polar and azimuthal angle of the track was taken into account for the boost into the Breit frame. The energy of the scattered electron for this boost was calculated according to the double angle

method:

$$E_{DA} = \frac{Q^2_{DA}}{2E_e(1+\cos\theta)} = \frac{2E_e \sin\gamma}{\sin\gamma + \sin\theta - \sin(\gamma+\theta)} \tag{5.1}$$

5.2 Preselection

The starting point for the preselection was the use of two DST (Data Selection Tape) filters. The DST filters are part of the offline reconstruction program ZEPHYR. The DST bits 9 and 11 were both required to be set. This ensures that one of various electron finders found a positron with an energy of at least 4 GeV and that

$$\delta = E - P_z = \sum E_i(1-\cos\theta_i) > 30\text{GeV} - 2E^{Lumi}_{\gamma}$$

is satisfied. The sum runs over all UCAL cells and E^{Lumi}_{γ} denotes the energy of a photon in the luminosity detector. In a DIS event δ is supposed to be around 2 times the beam energy of the positron. On the other hand in a photoproduction event with $Q^2 \approx 0$GeV the positron escapes the detection in the UCAL through the beampipe and δ has a much smaller value. E^{Lumi}_{γ} is taken into account to include also events with initial state radiation. The same DST filters are used for the preselection of Monte Carlo events at the detector level.

Another tool for the fast preselection of the data is the ZEUS Event Store (ZES). ZES is a database where many properties of an event are stored. Thus cuts can be applied without having to analyse all events. For this analysis cuts have been chosen with limits that were far away from the limits imposed in the final selection:

$$Q^2_{DA,Si} > 80\text{GeV}^2; \quad \delta > 20\text{GeV}; \quad |Z_{VTX}| < 70\text{cm}$$

where $Q^2_{DA,Si}$ is the Q^2_{DA} using the information of SINISTRA and Z_{VTX} is the Z-coordinate of the event vertex.

In the first analysis only events are kept which have at least one jet with $E^B_t > 2.5$ GeV, where E^B_t denotes the transverse energy of a jet in the Breit frame. At this stage the jet energy correction is not yet applied. The phase space is further constraine which will be described in the section on cleaning cuts.

5.3 Kinematic Region and Jet Selection

For the selection of the kinematic region the following two requirements are imposed:

- $Q^2 > 125\text{GeV}^2$. For the reconstruction of Q^2 the double angle method is used having the best resolution.
- $-0.7 < \cos\gamma < 0.5$

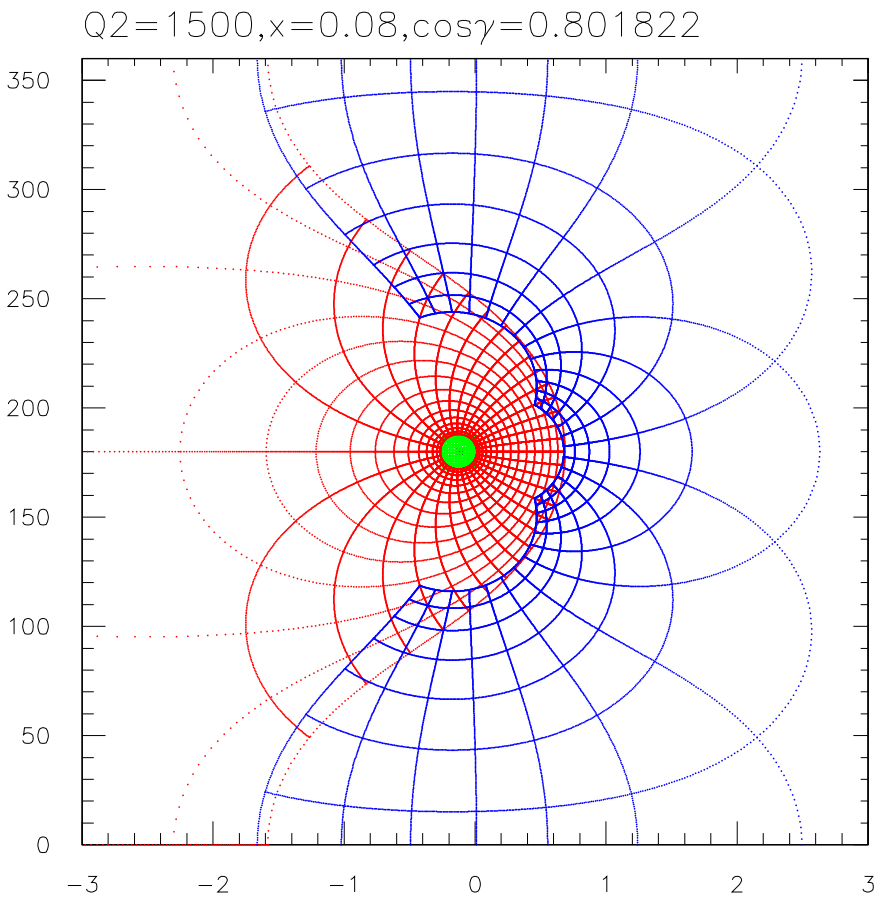

Figure 5.2: The UCAL cell structure in the Breit frame in the (η, ϕ)-plane for a value of $\cos\gamma$ which is larger than the upper limit. In this case many cells are very large giving an unfavourable resolution for the jet reconstruction.

Fig. 5.2 and Fig. 5.3 illustrate why an upper limit for $\cos\gamma$ is required. In these figures the structure of the UCAL is shown as it is seen in the Breit frame in the (η, ϕ)-plane. In Fig. 5.2 the value of $\cos\gamma$ is beyond the upper limit. In this case big parts of the UCAL have very large cells giving an unfavourable resolution for the jet reconstruction. In Fig. 5.3 the value for $\cos\gamma$ is inside the accepted range. Here most cells have an acceptable size (jets with $\eta > 1.8$ are excluded). Fig. 5.4 shows a comparison of $\cos\gamma$ on detector and hadron level. As can be seen from this figure, including events with $\cos\gamma < -0.7$ would result in large correction factors and is therefore excluded.

The jet search was performed in the Breit frame. At the detector level a jet energy correction was applied. The jets are then required to pass the following cuts:

- $E_t^B > 8$GeV, where E_t^B is the transverse energy of the jet in the Breit

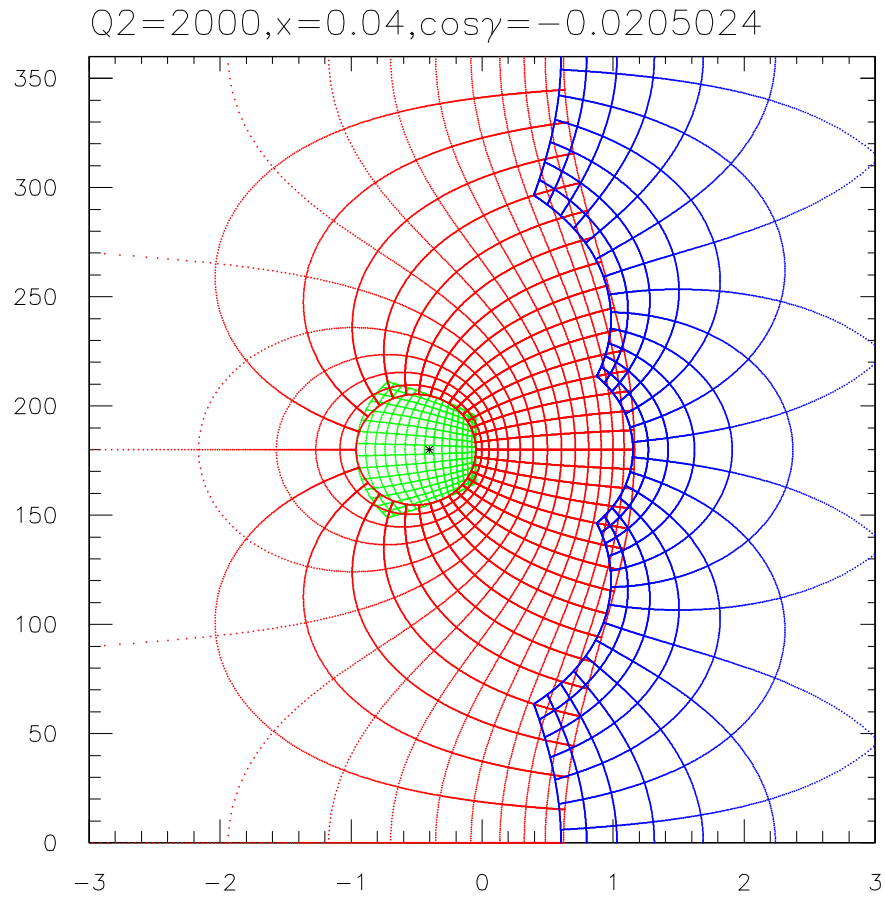

Figure 5.3: The UCAL cell structure in the Breit frame in the (η, ϕ)-plane for a value of $\cos\gamma$ which is within the chosen range. In this case most cells have an acceptable size.

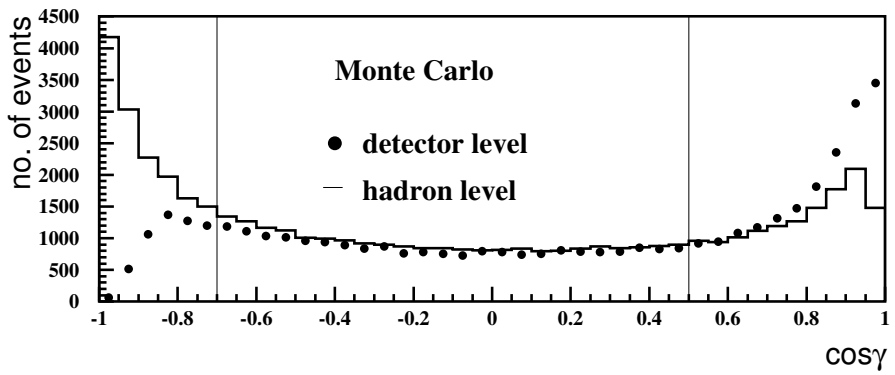

Figure 5.4: Comparison of $\cos\gamma$ on detector and hadron level. All cuts except the cut on $\cos\gamma$ have been applied. The boundaries of the accepted range are indicated with a line.

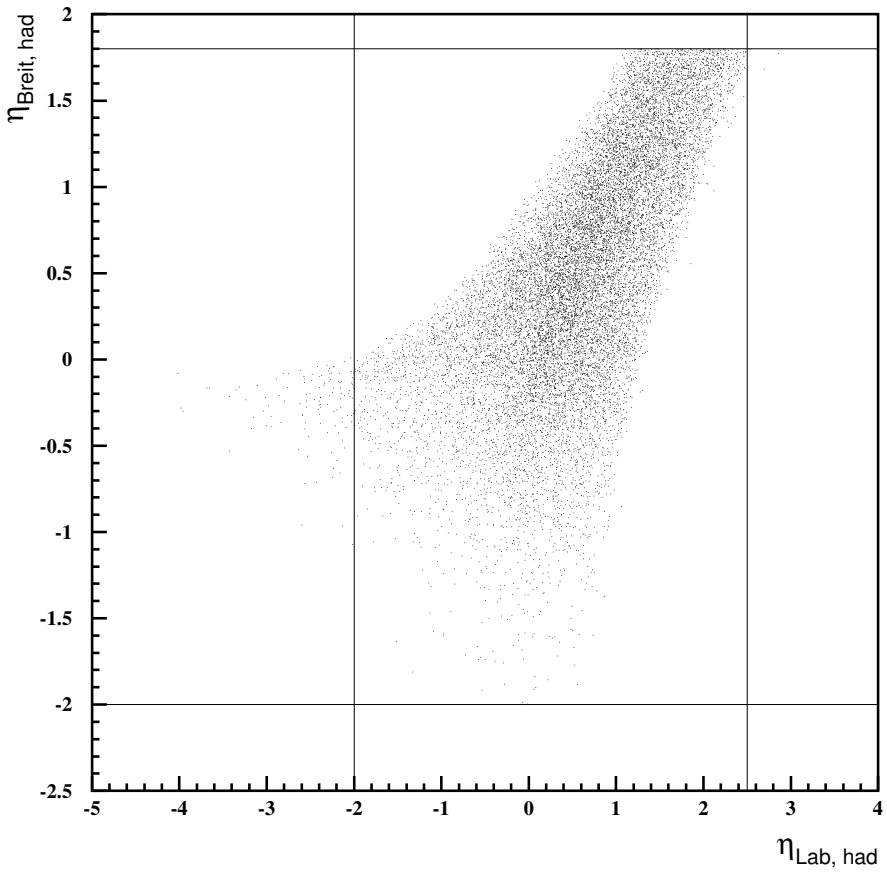

Figure 5.5: The correlation between the pseudorapidities of the jets in the laboratory and Breit frame on hadron level.

frame.

- $-2 < \eta^B < 1.8$, where η^B is the pseudorapidity of the jet in the Breit frame.

Fig. 5.5 shows the correlation at the hadron level between the pseudorapidity of the jets in the laboratory, η^L, and the pseudorapidity in the Breit frame, η^B. As can be seen from this figure, the upper limit for η^B prevents the jets to have a value for η^L larger than 2.5. This region should be excluded since the UCAL resolution worsens. (The same conclusion would hold for the same relation at the detector level. The reason of showing the hadron level is that this figure can also be refered to in the section on cleaning cuts.)

5.4 Cleaning Cuts

Cleaning cuts are event selection criteria that are only applied at the detector level. They are needed to reduce background and to improve the quality of the reconstruction.

The following cuts are imposed for data only:

- The routine EVTAKE discards events where an important detector component was out of operation.
- The routine O1TTYP is used to remove events recorded only for tests.

The cleaning cuts, now detailed, are required for both data and Monte Carlo:

- The routine RMSPARK removes events with sparks in single photomultiplier tubes of the UCAL.
- The routines ISITAMU and ALHALO2 reject events originating from cosmic muons or halo muons.
- At least one track in the CTD is required.
- $38 < \delta < 65$GeV. This cut removes events with large initial-state radiation and reduces the background from photoproduction.
- $y_{el} < 0.95$. This condition mostly rejects events where fake positron candidates are found in the FCAL.
- The vertex position along the beam axis is required to be in the range $-38 < Z < 32$cm.
- A positron candidate is found with an uncorrected energy $E_e{}' > 10$GeV. This cut ensures a high and well understood positron finding efficiency and further suppresses background from photoproduction.
- $\not{p}_T/\sqrt{E_T} < 2.5\text{GeV}^{1/2}$ where $\not{p}_T$ is the missing transverse momentum as measured with the UCAL ($\not{p}_T \equiv \sqrt{p_X^2 + p_Y^2}$) and E_T is the total transverse energy in the UCAL. This cut removes cosmic rays and beam-related background.
- One of four additional DST-bits is required to be set:
  - DST64 (very high E_t): The total transverse energy in the UCAL has to be larger than 25 GeV. The region around the FCAL beampipe is excluded for the measurement of E_t.
  - DST65 (inclusive jet): At least one jet has to be found with a transverse energy larger than 10 GeV and $\eta(\text{jet}) < 2.5$.

- DST77 (dijet low E_t): Two or more jets must be found with $E_t(\text{jet}) > 4\text{GeV}$ and $\eta(\text{jet}) < 2.5$.
- DST78 (dijet high E_t): two or more jets have to be found with $E_t(\text{jet}) > 6\text{GeV}$ and $\eta(\text{jet}) < 2.5$ or $E_t(\text{jet}) > 4\text{GeV}$ and $\eta(\text{jet}) < 1.5$.

For these bits the scattered positron is not looked for.

- For the following two cuts the polar angle of the scattered positron, θ, has to be between 20° and 140°.
  - The total energy associated with the positron candidate within a cone of radius 0.3 units in the (η, ϕ)-plane around the positron direction, $E_{cone,e}$, is required to be more than 90% of the positron energy. This condition removes events where the two photons of a neutral pion decay was falsely identified as the scattered positron.
  - The total energy not associated with the positron candidate within a cone of radius 0.7 units in the (η, ϕ)-plane around the positron direction, $E_{cone,h}$, is required to be less than 10% of the positron energy. This condition rejects events where part of a jet was falsely identified as the scattered positron.

- If a jet with $E_t^B > 5\text{GeV}$ (before the jet energy correction) is found within a cone of radius 1 unit in the (η, ϕ)-plane around the direction of the scattered positron, the event is discarded. This selection criterion improves the purity of the positron finding since a part of a jet could be falsely identified as the scattered positron. [1]

- If a jet with $E_t^B > 5\text{GeV}$ (before the jet energy correction) is found with $\eta^L < -2$, the event is rejected. As can be seen from Fig. 5.5, there are very few jets with a pseudorapidity less than -2 having such a high E_t^B. At the detector level, where no effort is made to identify photons from initial and final-state radiation, such a 'jet' is most likely to be a photon from initial-state radiation. If such a photon is reconstructed as a jet, the event is badly reconstructed. For this reason these events are rejected.

- In addition to jet selection criteria introduced in the previous section, the transverse energy of a jet in the laboratory frame, E_t^L, is required to be above 2.5 GeV. This condition ensures an unambiguous signal in the UCAL.

In Table 5.1 the number of events removed by the various cuts is given. To determine these numbers, the order of the cuts in this table was the order in the analysis procedure. A rejected event is only counted once. After having

[1] This selection criterion has been introduced after the ICHEP 2000 in Osaka [54].

preselected events	167623
$Q^2 < 125\text{GeV}^2$	33777
$\cos\gamma$ out of range	93313
δ out of range	3480
$y_{el} > 0.95$	15
Z_{VTX} out of range	950
$E_e{}' < 10\text{GeV}$	37
$\not{p}_T/\sqrt{E_T} > 2.5\text{GeV}^{1/2}$	18
$(E_{cone,e}/E_e{}') < 0.9$	82
$(E_{cone,h}/E_e{}') > 0.1$	495
additional DST-bits	446
$R_{min}^{jet,el} < 1$	1049
$\eta^L < -2$	1237
jet selection cuts	25158
events accepted	7566

Table 5.1: The effect of the various cuts on the data.

applied all cuts a data sample of 7566 events remains for the determination of the inclusive jet cross sections. In this sample 4607 events have one jet, 2817 events have two jets, 137 events have three jets, and 5 events have four jets giving 10672 jets in total. In Fig. 5.6 the accepted data sample is shown in the (x, Q^2)-plane.

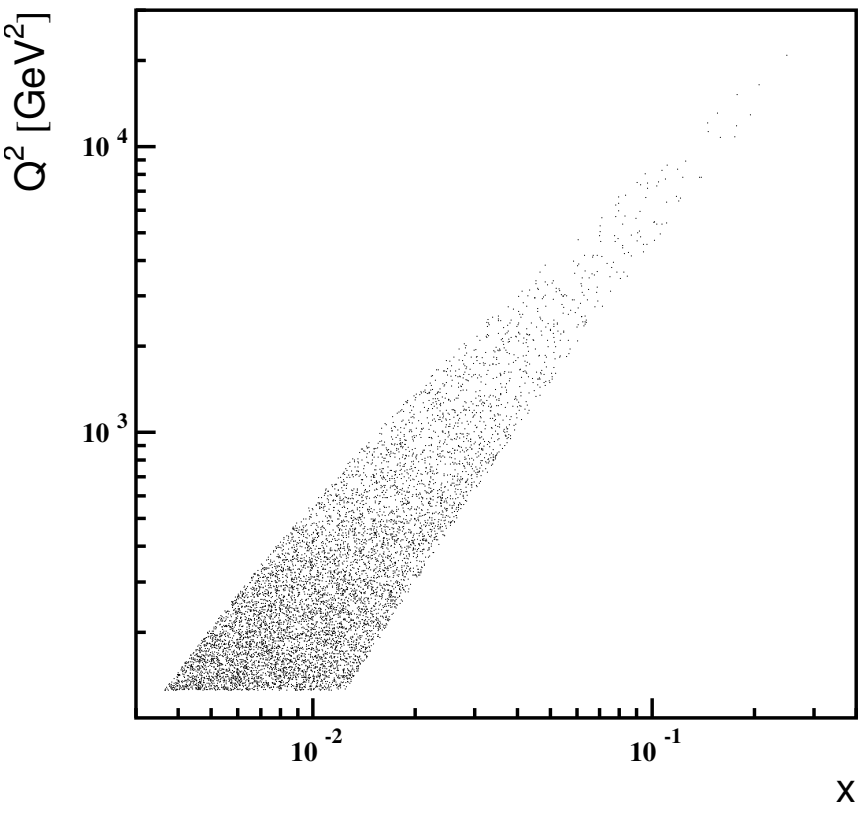

Figure 5.6: The accepted data sample in the (x, Q^2)-plane. The double angle method has been used to reconstruct x and Q^2.

Chapter 6

The Analysis

6.1 Noise Suppression and Global Energy Correction

To minimize the influence from the uranium noise in the UCAL isolated EMC (HAC) cells with less than 80 MeV (140 MeV) are removed. If the imbalance between the two read-out channels of an isolated cell with less than 1 GeV is higher than 70 % the cell is also removed. These corrections are performed for both data and Monte Carlo. In the case of analysing data, cells are removed which were found to be continously noisy over some time. After these corrections the positron identification can be performed as described in the previous chapter.

Furthermore a calorimeter calibration correction has to be done to make the data and Monte Carlo energy scales agree. It is assumed that this correction is necessary since the inactive material is not completely modeled in the Monte Carlo. The correction has to be applied either for data or Monte Carlo. In this analysis it is done for data. If the positron is found in the BCAL (RCAL) its energy is scaled up by a factor of 1.05 (1.025). Energy deposits belonging to the hadronic final state are corrected with the routine RCALCORR. This routine applies a cell-by-cell correction for the RCAL. For all cells in BCAL the correction factor is again 1.05.

6.2 The Jet Energy Correction

From Monte Carlo studies it can be observed that the transverse energy of a jet on detector level, $E_{t,lab}$(detector level), is significantly smaller than the transverse energy of a matching jet on hadron level, $E_{t,lab}$(hadron level). Fig. 6.1a illustrates this situation. The reason for this difference is due to energy loss of hadrons in the inactive material in the detector. Thus a jet energy correction has to be applied in order to reduce migrations between different bins and to keep correction factors small.

For this analysis the parameters of the correction are determined from a Monte Carlo. A jet on detector level is considered to match with a jet on

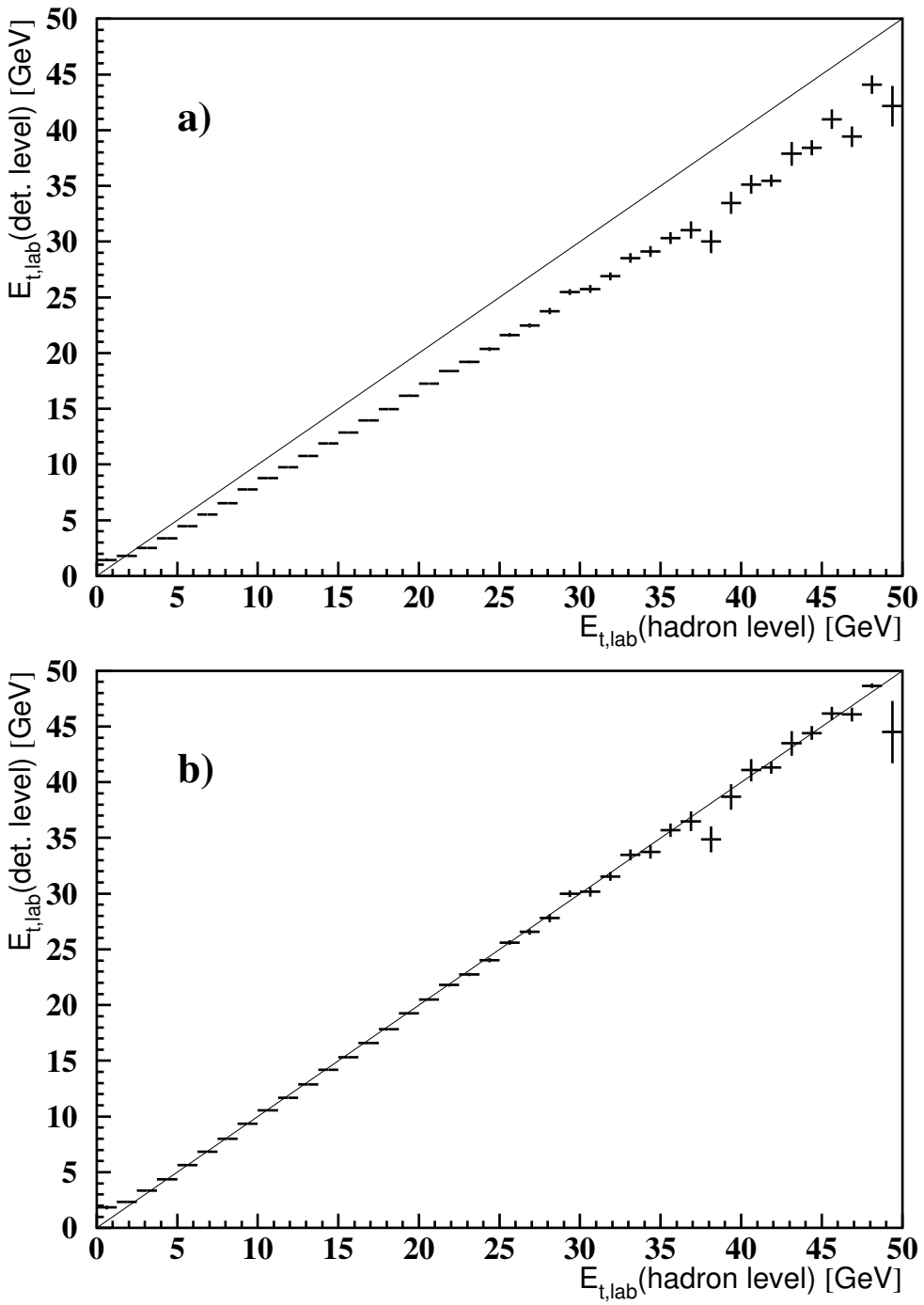

Figure 6.1: The averaged correlation between the jets' transverse energy on detector and hadron level a) before and b) after the jet energy correction.

hadron level if the distance in the (η, ϕ)-plane in the laboratory frame is smaller than one. For various ranges of jet pseudorapidity at detector level a profile plot like Fig. 6.1a is obtained. A straight line fit is performed to the points of such a plot. Table 6.1 shows the results of the fits. Using the slope and the intercept of this straight line fit the inverse function gives a prescription for the jet energy correction. Fig. 6.1b shows the averaged correlation between $E_{t,lab}$(detector level) and $E_{t,lab}$(hadron level) after the jet energy correction.

η-range	intercept	slope
(-2.0,-1.0)	0.3538	0.6216
(-1.0,-0.75)	0.0235	0.7155
(-0.75,-0.5)	0.0238	0.7403
(-0.5,-0.25)	-0.3659	0.8495
(-0.25,0.0)	-0.4002	0.8661
(0.0,0.25)	-0.4160	0.8757
(0.25,0.5)	-0.2313	0.8579
(0.5,0.75)	-0.4467	0.8725
(0.75,1.0)	-0.6443	0.8609
(1.0,1.25)	-0.2885	0.8078
(1.25,1.5)	-0.3747	0.8393
(1.5,1.75)	-0.4505	0.8837
(1.75,2.0)	-0.5370	0.9175
(2.0,3.0)	-0.8495	0.9888

Table 6.1: Results of the straight line fits to determine the parameters of the jet energy correction.

6.3 Comparison of Data and LO Monte Carlos

The first step in an analysis like this is the comparison at detector level between the data and the leading order (LO) Monte Carlos. Only if a Monte Carlo describes the data reasonably well can it be used to correct the data to hadron level. As the normalisation of a Monte Carlo is not relevant for the determination of the correction factors, only the shapes are compared.

Fig. 6.2 shows the distributions of various jet observables: the transverse energy in the Breit frame, $E_{t,Breit}$, the pseudorapidity in the Breit frame, η_{Breit}, the pseudorapidity in the Laboratory frame, η_{Lab}, and the azimuthal angle in the Breit frame, ϕ_{Breit}. The crosses represent the data indicating the bin widths and errors. The dashed line is Ariadne and the dotted line Lepto. The binning is the same as for the differential jet cross sections except for η_{Lab} where there are twice as many bins. Notice that the distributions for ϕ_{Breit} are rather flat not displaying peaks at 0° and 180°. This will be discussed further in another section of this chapter.

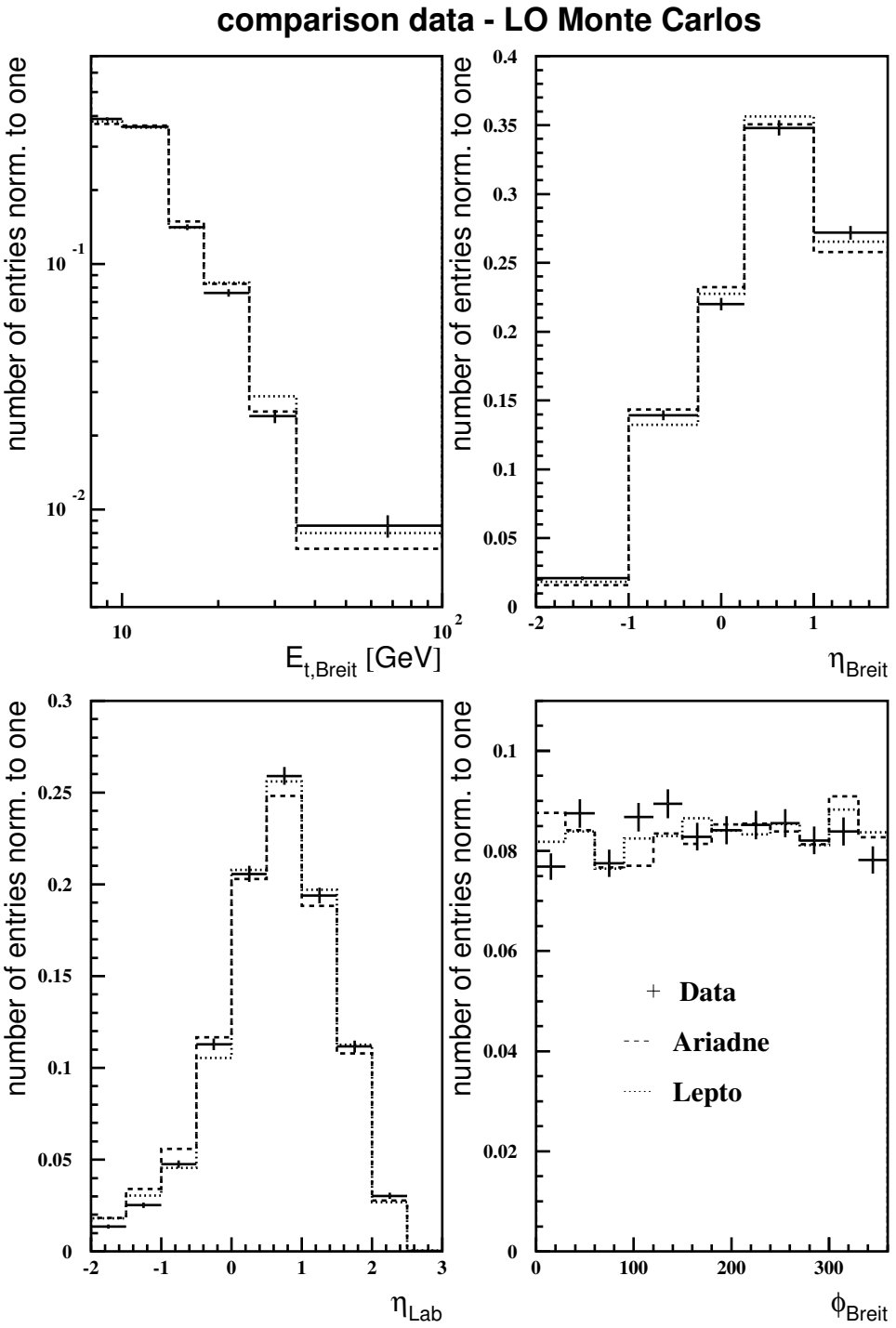

Figure 6.2: Comparison at detector level between data and the LO Monte Carlos Ariadne and Lepto. The distributions of some jet observables are shown: the transverse energy in the Breit frame, $E_{t,Breit}$, the pseudorapidities in the Breit frame, η_{Breit}, and in the Laboratory frame, η_{Lab}, and the azimuthal angle in the Breit frame, ϕ_{Breit}. As for each distribution the total number of entries is set to one, only the shape of the distributions is compared.

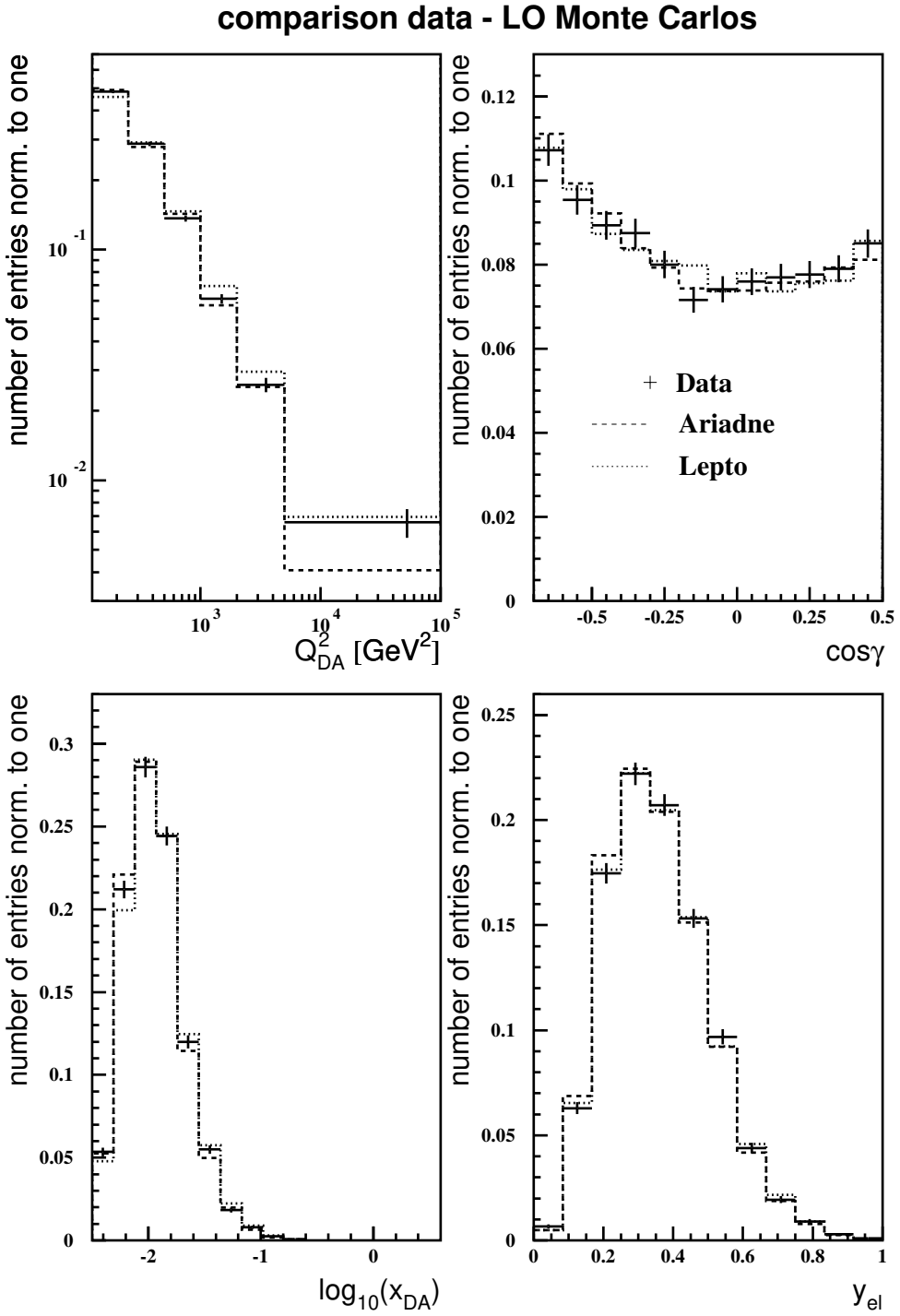

Figure 6.3: Comparison at detector level between data and the LO Monte Carlos Ariadne and Lepto. The distributions of some kinematic variables are shown: the squared four-momentum transfer reconstructed with the double angle method, Q^2_{DA}, the cosine of the hadronic polar angle, $\cos\gamma$, the logarithm of the Bjorken x reconstructed with the double angle method, $\log_{10} x_{DA}$, and the inelasticity reconstructed with the electron method, y_{el}. As for each distribution the total number of entries is set to one, only the shape of the distributions is compared.

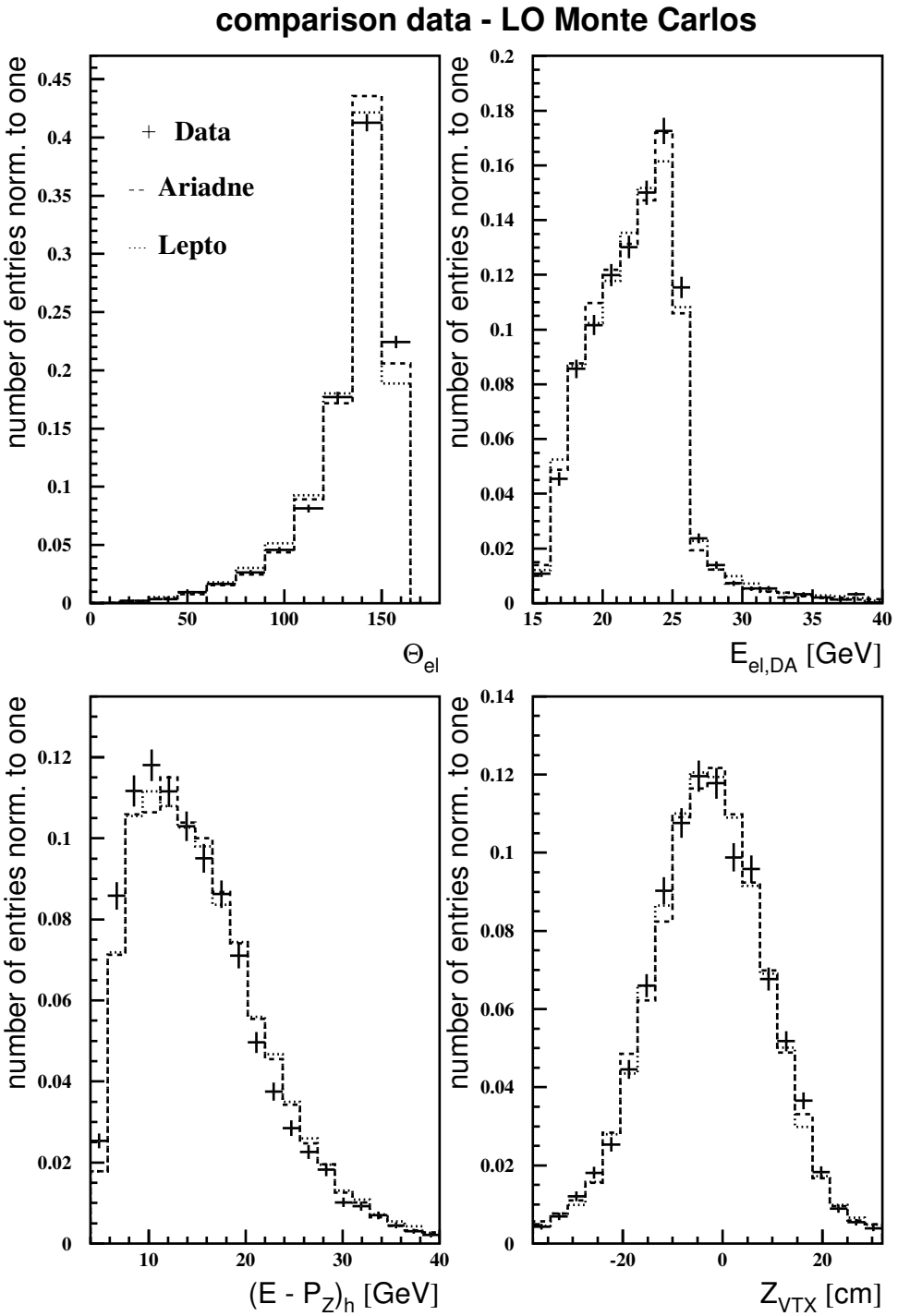

Figure 6.4: Comparison at detector level between data and the LO Monte Carlos Ariadne and Lepto. The distributions of the positron's polar angle, θ_{el}, and its energy reconstructed with the double angle method, $E_{el,DA}$, are shown. Furthermore the hadronic $E - P_Z$ and the Z position of the event vertex, Z_{VTX}, are displayed. As for each distribution the total number of entries is set to one, only the shape of the distributions is compared.

Fig. 6.3 shows the distributions of various kinematic variables: the squared four-momentum transfer reconstructed with the double angle method, Q^2_{DA}, the cosine of the hadronic polar angle, $\cos\gamma$, the logarithm of Bjorken x reconstructed with the double angle method, $\log_{10}(x_{DA})$, and the inelasticity reconstructed with the electron method, y_{el}. Both Ariadne and Lepto describe the data reasonably well.

Fig. 6.4 shows the distributions for quantities that are either important for the boost into the Breit frame or used to apply cleaning cuts: the polar angle of the positron, θ_{el}, the energy of the positron reconstructed with the double angle method, $E_{el,DA}$, the part of $(E - P_Z)$ coming from the hadronic final state and the Z position of the event vertex. The $(E - P_Z)_h$ of both Monte Carlos is slightly shifted towards higher values with respect to the data. This shift has also been observed for the part of the $(E - P_Z)$ coming from the positron. However the dependence of the results on the energy scale of the UCAL will be investigated in the section on systematic studies (Sec. 6.6).

In general the shapes of the data distributions are well reproduced by both Monte Carlos. The factors obtained with Ariadne are taken as the central values for correcting the data to hadron level. Deviations arising from using Lepto for this correction will be included in the systematic errors.

6.4 Efficiencies and Purities

The next step is to determine the efficiencies and purities for the inclusive jet cross sections. The efficiency, ε, and the purity, P, are defined in the following way:

$$C = \text{number of jets generated and reconstructed in a bin}$$

$$D = \text{number of jets generated but not reconstructed in a bin}$$

$$E = \text{number of jets reconstructed but not generated in a bin}$$

$$\varepsilon = \frac{C}{C + D}$$

$$P = \frac{C}{C + E}$$

The efficiency is a measure of how many of the generated jets are reconstructed in the same bin. Similarly, the purity is a measure of how many of the reconstructed jets are generated in the same bin. To estimate these quantities a Monte Carlo is used (The values that are shown were obtained with Ariadne.). Neither the efficiency nor the purity should be too low in order to have a good correlation between detector and hadron level. Obviously the larger the bin size the larger is the value of the efficiency and purity. The cleaning cuts, that are only performed at detector level, reduce the value of the efficiency. The error of the efficiency and purity is obtained using the error propagation law and assuming that the error of finding N jets is $\sqrt{N}$:

$$(\Delta\varepsilon)^2 = \frac{DC}{(C + D)^3}$$

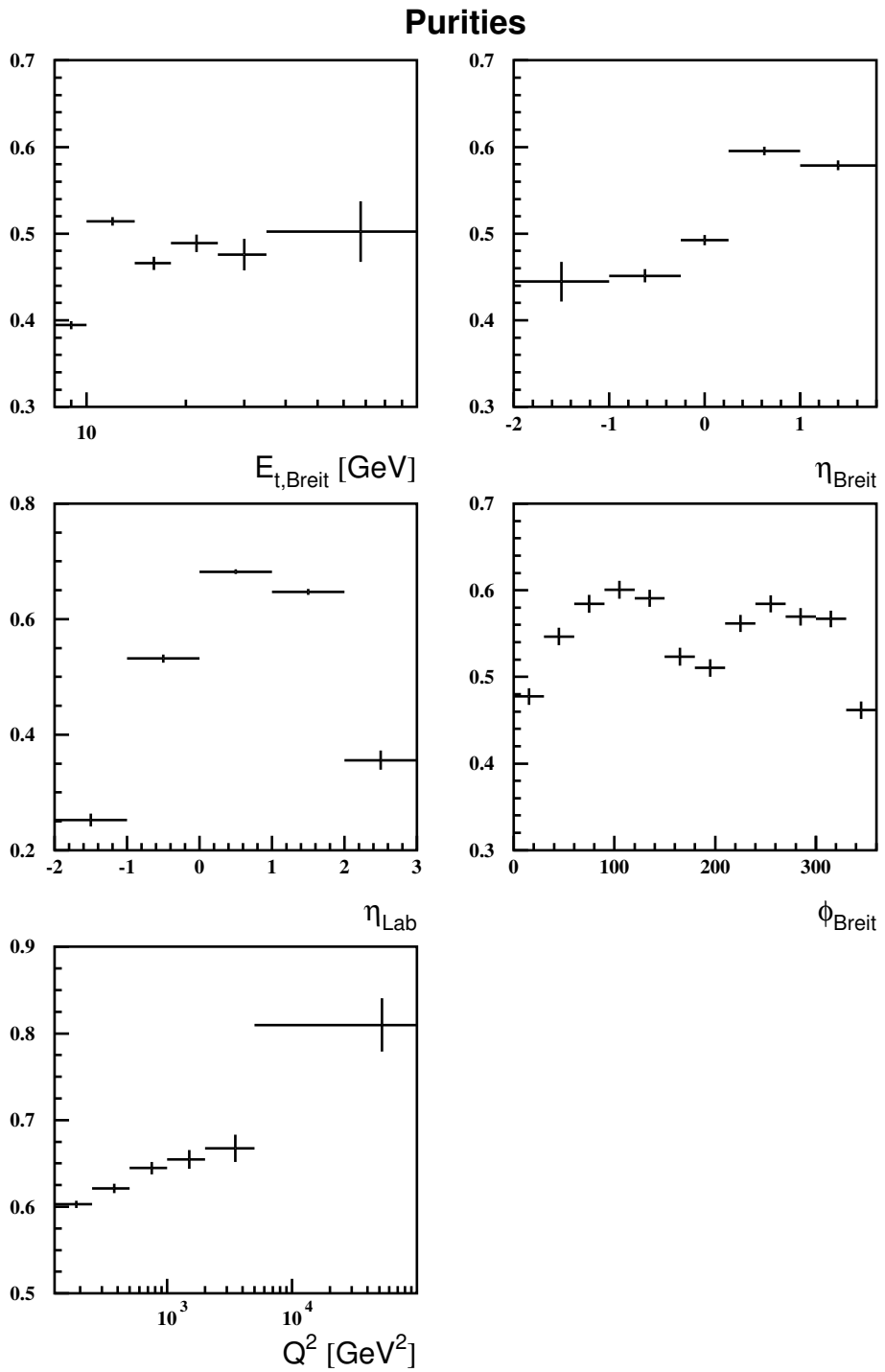

Figure 6.5: Purities for the inclusive differential jet cross sections $d\sigma/dE_{t,Breit}$, $d\sigma/d\eta_{Breit}$, $d\sigma/d\eta_{Lab}$, $d\sigma/d\phi_{Breit}$ and $d\sigma/dQ^2$.

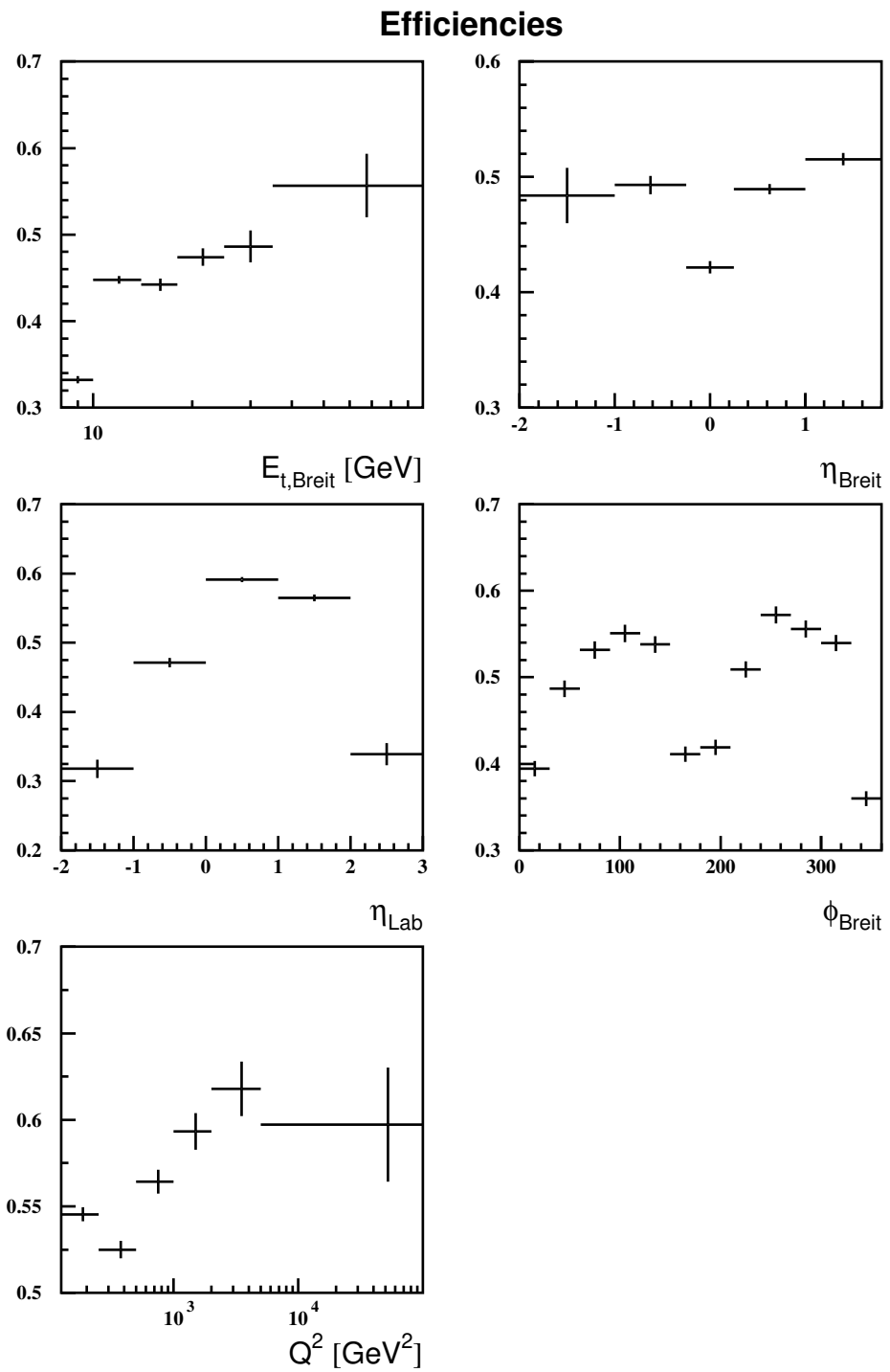

Figure 6.6: Efficiencies for the inclusive differential jet cross sections $d\sigma/dE_{t,Breit}$, $d\sigma/d\eta_{Breit}$, $d\sigma/d\eta_{Lab}$, $d\sigma/d\phi_{Breit}$ and $d\sigma/dQ^2$.

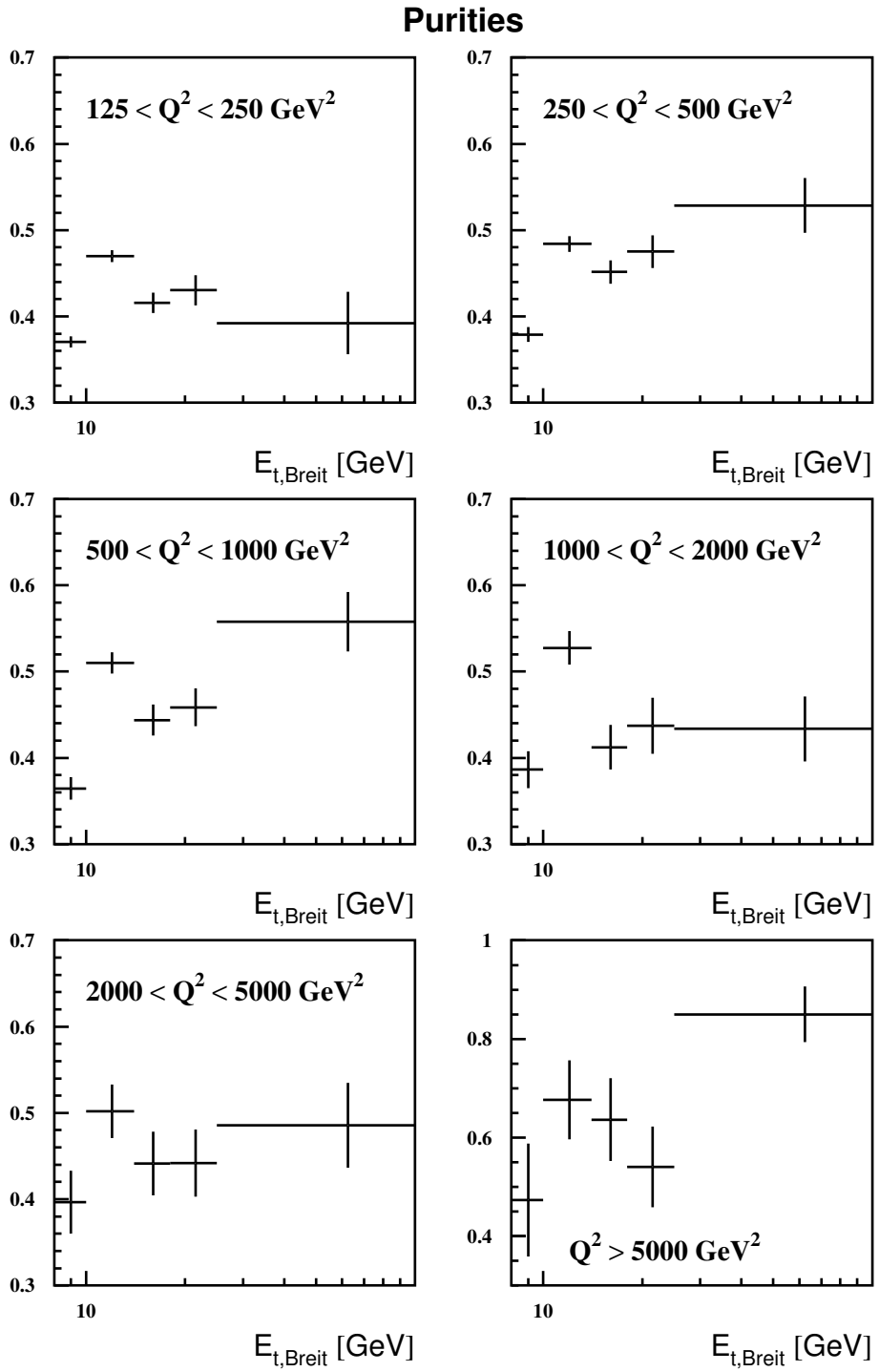

Figure 6.7: Purities for the inclusive double differential jet cross sections $d^2\sigma/dE_{t,Breit}dQ^2$.

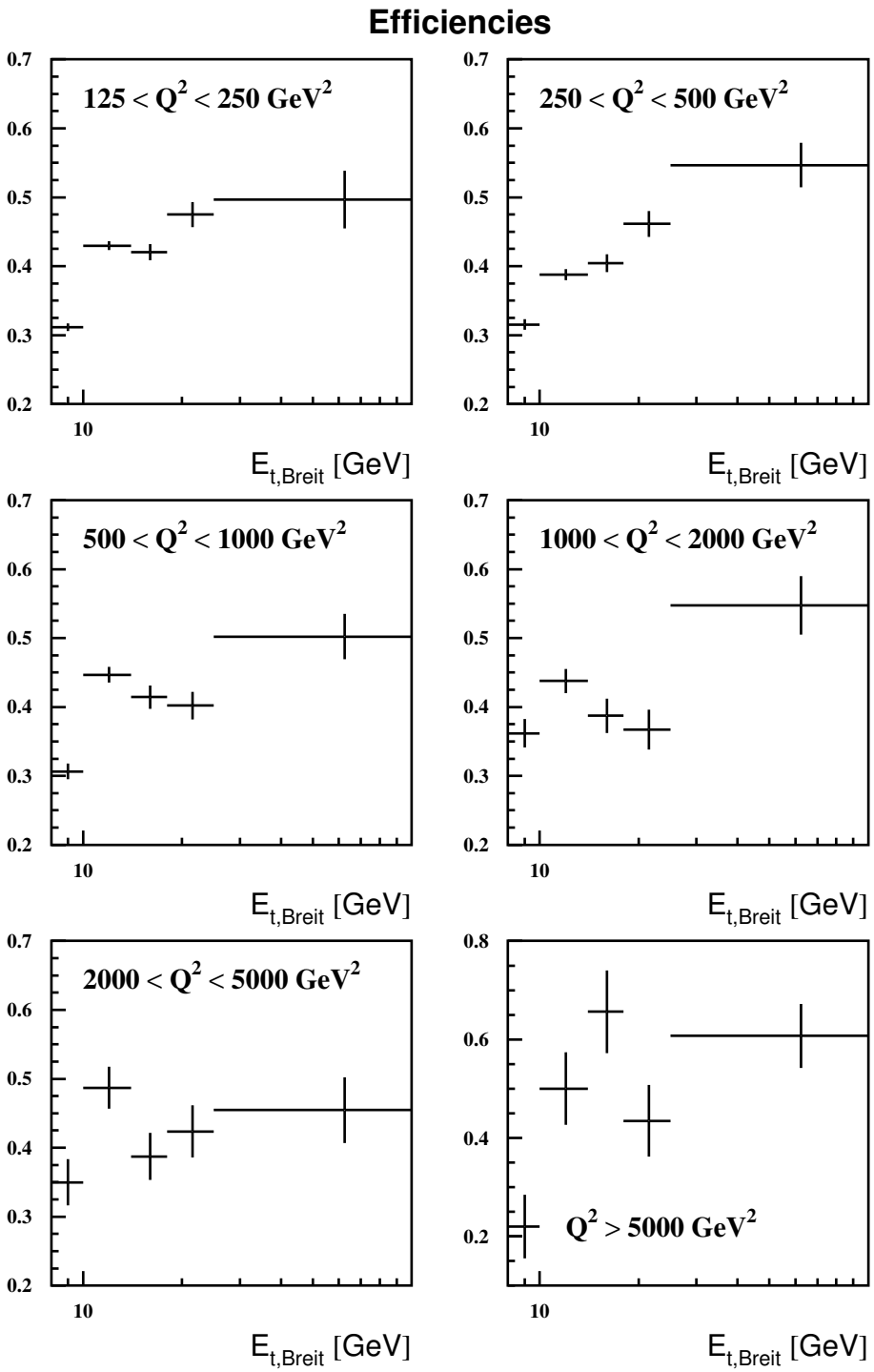

Figure 6.8: Efficiencies for the inclusive double differential jet cross sections $d^2\sigma/dE_{t,Breit}dQ^2$.

$$(\Delta P)^2 = \frac{EC}{(C+E)^3}$$

Fig. 6.5 shows the purities for the inclusive differential jet cross sections $d\sigma/dE_{t,Breit}$, $d\sigma/d\eta_{Breit}$, $d\sigma/d\eta_{Lab}$, $d\sigma/d\phi_{Breit}$ and $d\sigma/dQ^2$. In most bins the purity is about 50% or even higher. In the first bin of $d\sigma/dE_{t,Breit}$ the purity has a value of 40% which is still acceptable. The reason for the smaller value is the bin width of two GeV. In general the bin size should be chosen such that the bin accomodates at least 2σ where σ is the resolution. For this bin the resolution is about 11%, so the bin size is at the limit. However, the number of jets in this bin is so high that a larger bin size is unnecessary from a statistical point of view. The purities for $d\sigma/d\eta_{Lab}$ are low for very rear and very forward jets. As can be seen in Fig. 6.6, in the range $-2 < \eta_{Lab} < -1$, the purity is even a bit smaller than the efficiency. The reason for this may be photons from initial state radiation that are misidentified as jets at detector level. However, as Fig. 6.2 reveals, the data are well reproduced by the Monte Carlos in that region. In the range $2 < \eta_{Lab} < 3$ the purity is about 35%. The reason for this is that there are only very few jets with $\eta_{Lab} > 2.5$, so the bin is actually rather narrow.

Fig. 6.6 shows the efficiencies for the inclusive differential jet cross sections. The shape of the distributions are similar to those of the purities. In general the value for the efficiency is a bit lower than the value for the purity. This is caused by the various cleaning cuts which discard numerous jets at detector level.

Fig. 6.7 displays the purities for the inclusive double differential jet cross sections $d\sigma/dE_{t,Breit}dQ^2$. For most bins the purity is above 40% which is a good value for a double differential cross section. Only for 8 GeV $< E_{t,Breit} <$ 10 GeV some values of the purity are a bit lower than 40%. Fig. 6.8 is the corresponding figure for the efficiencies. The same conclusions as for the purities hold except that for $Q^2 > 5000$ GeV^2 in the lowest bin for $E_{t,Breit}$ the efficiency is very small (about 22%). However for this range of Q^2 the number of jets is quite low which is also indicated by the error bars.

6.5 Correction Factors

In order to compare the data with the predictions of the NLO calculations the data as well as the NLO results are corrected to hadron level. The method used in this analysis is the bin-by-bin correction, i.e. for each bin a correction factor is obtained from Monte Carlos by dividing the cross section of one level with the cross section of another level. For example, the correction factor, C_i^{dh}, by which the data are corrected to hadron level is the ratio

$$C_i^{dh} = \frac{\sigma_{i,MC2}^{had}}{\sigma_{i,MC1}^{det}},$$

where $\sigma^{had}_{i,MC2}$ denotes the cross section of a Monte Carlo at hadron level in a bin and $\sigma^{det}_{i,MC1}$ denotes the cross section of another Monte Carlo at detector level in the same bin. In this analysis MC1 is a leading order Monte Carlo with initial and final state radiation (ISR and FSR). MC2 is a LO Monte Carlo of the same type as MC1 but without ISR, FSR. The hadron level of a Monte Carlo with ISR, FSR in general is about 3% higher than the hadron level of a Monte Carlo without these features. There are two LO Monte Carlos to correct the data to hadron level: Ariadne and Lepto. In the figures only the error of the correction factors obtained with Ariadne is presented since Ariadne is the first choice Monte Carlo for the correction. The correction factors obtained for Lepto are also presented but without errors which are very similar to those of Ariadne.

Fig. 6.9 shows the factors by which the data are corrected to hadron level level for the inclusive differential jet cross sections $d\sigma/dE_{t,Breit}$, $d\sigma/d\eta_{Breit}$, $d\sigma/d\eta_{Lab}$, $d\sigma/d\phi_{Breit}$ and $d\sigma/dQ^2$. The largest correction factors are about 20% and are similar for both Ariadne and Lepto. The correction factors for $d\sigma/dE_{t,Breit}$ are reasonably flat, only for lower $E_{t,Breit}$ there is a slight rise. The distribution of the correction factors for $d\sigma/d\phi_{Breit}$ has distinct peaks at $0°$ and $180°$. Recall that the distribution of $d\sigma/d\phi_{Breit}$ is rather flat at detector level. This feature will be discussed in a seperate section of this chapter.

Fig. 6.10 displays the factors by which the data are corrected to hadron level for the inclusive double differential jet cross sections $d^2\sigma/dE_{t,Breit}dQ^2$. The factors are in the order of 20% and below. The only exception is the lowest $E_{t,Breit}$-bin for $Q^2 > 5000$ GeV^2 where the factor obtained with Ariadne is about 100%. However the error for this factor is very large. The agreement between Ariadne and Lepto is not as good as in the previous figure. On the other hand migrations between the bins are expected to be higher for double differential cross sections. However the migrations are not too large as the purities and efficiencies indicate and most deviations are generally compatible with the errors.

The cross sections of the NLO calculations are also corrected to hadron level; this time from parton to hadron level. There are three LO Monte Carlos without ISR and FSR from which hadronisation correction factors are obtained: Ariadne, Lepto and Herwig. The factors by which the NLO calculations are corrected are the mean values of the factors obtained with the three Monte Carlos. The uncertainty of the correction was set equal to the estimate of the spread.

Fig. 6.11 shows the effects of the hadronization on the inclusive differential jet cross sections. (The displayed factors are for the correction of the hadron level to parton level. The factors by which the NLO calculations are corrected are the reciprocal values.) For $d\sigma/dE_{t,Breit}$, $d\sigma/d\phi_{Breit}$ and $d\sigma/dQ^2$ the corrections are below 10%. For $d\sigma/d\eta_{Breit}$ and $d\sigma/d\eta_{Lab}$ the correction is in the order of 20% in the backward direction.

The hadronization correction factors for $d^2\sigma/dE_{t,Breit}dQ^2$ are shown in Fig. 6.12. The corrections are in the order of 10% and below. The distributions

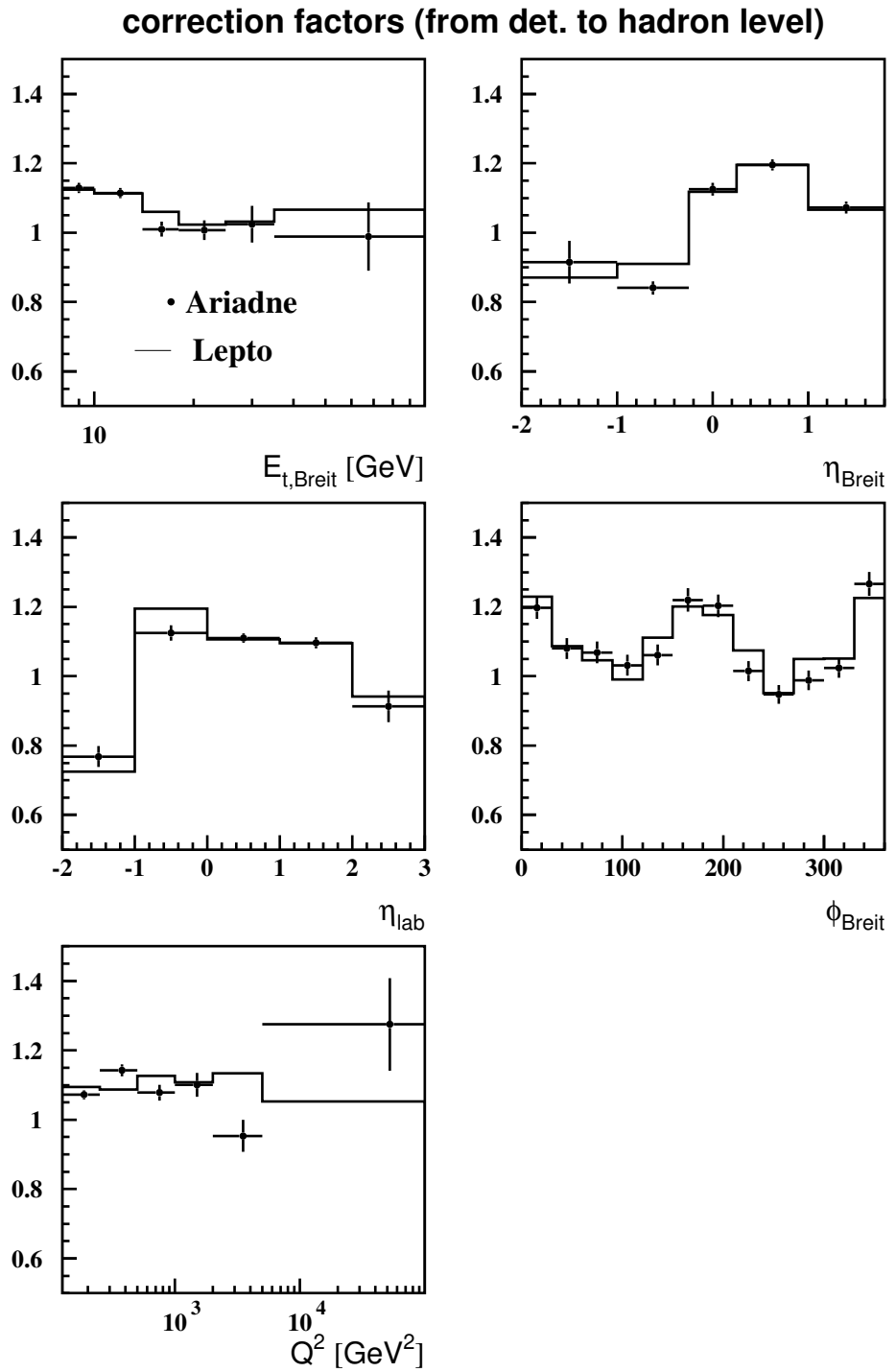

Figure 6.9: Factors to correct the data to hadron level for the inclusive differential jet cross sections $d\sigma/dE_{t,Breit}$, $d\sigma/d\eta_{Breit}$, $d\sigma/d\eta_{Lab}$, $d\sigma/d\phi_{Breit}$ and $d\sigma/dQ^2$.

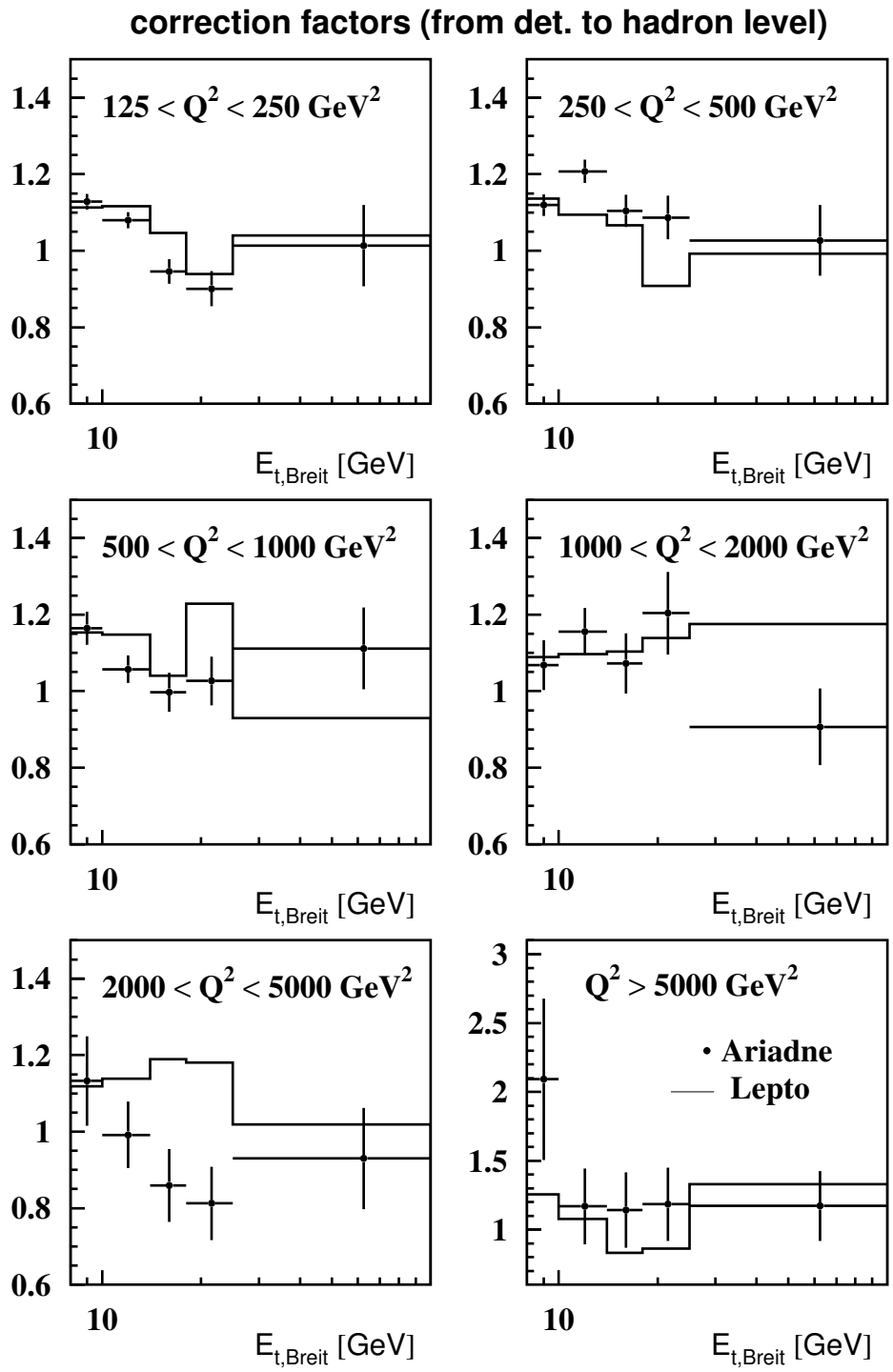

Figure 6.10: Factors to correct the data to hadron level for the inclusive double differential jet cross sections $d^2\sigma/dE_{t,Breit}dQ^2$.

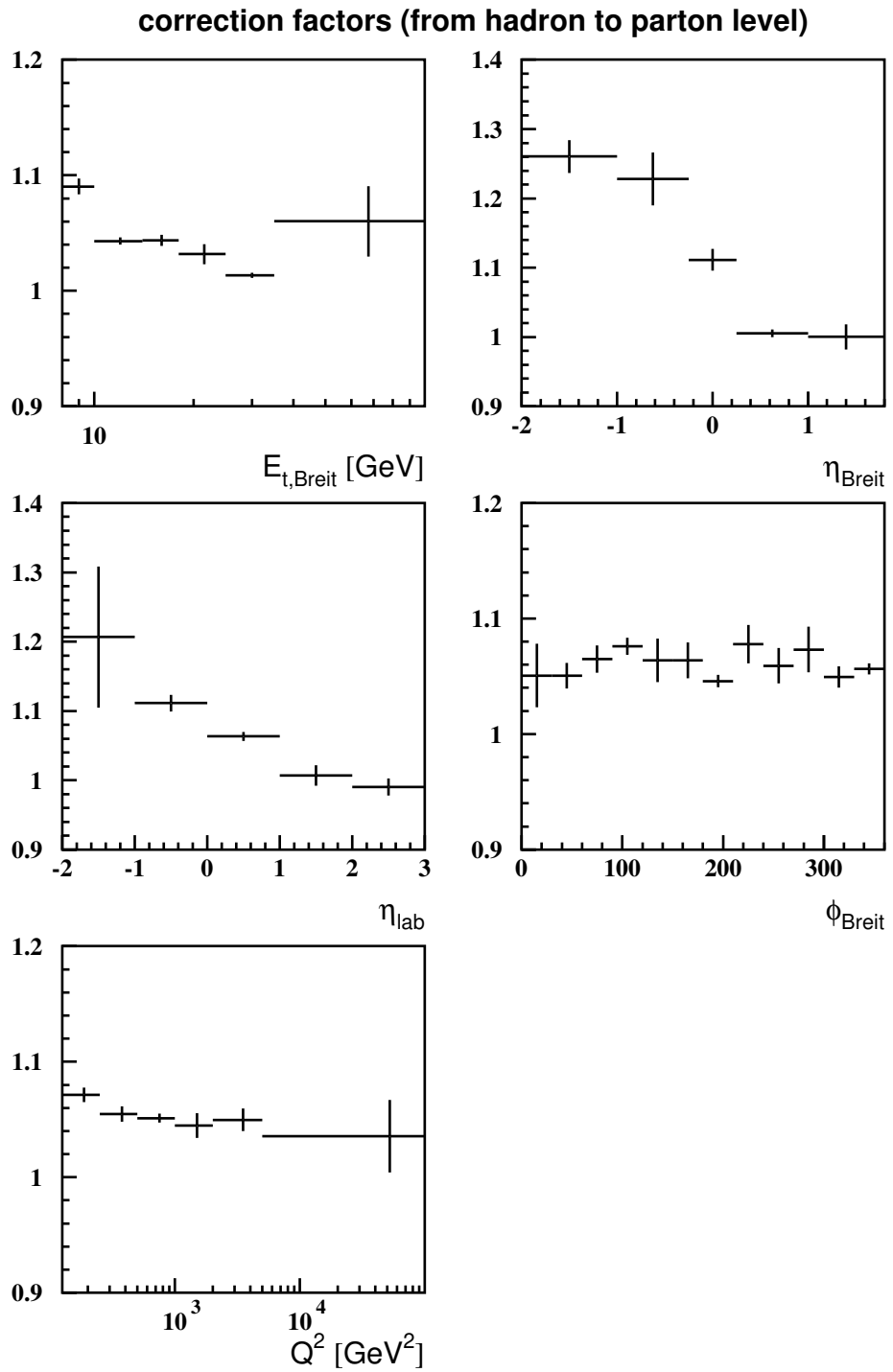

Figure 6.11: Hadronization corrections for the inclusive differential jet cross sections $d\sigma/dE_{t,Breit}$, $d\sigma/d\eta_{Breit}$, $d\sigma/d\eta_{Lab}$, $d\sigma/d\phi_{Breit}$ and $d\sigma/dQ^2$.

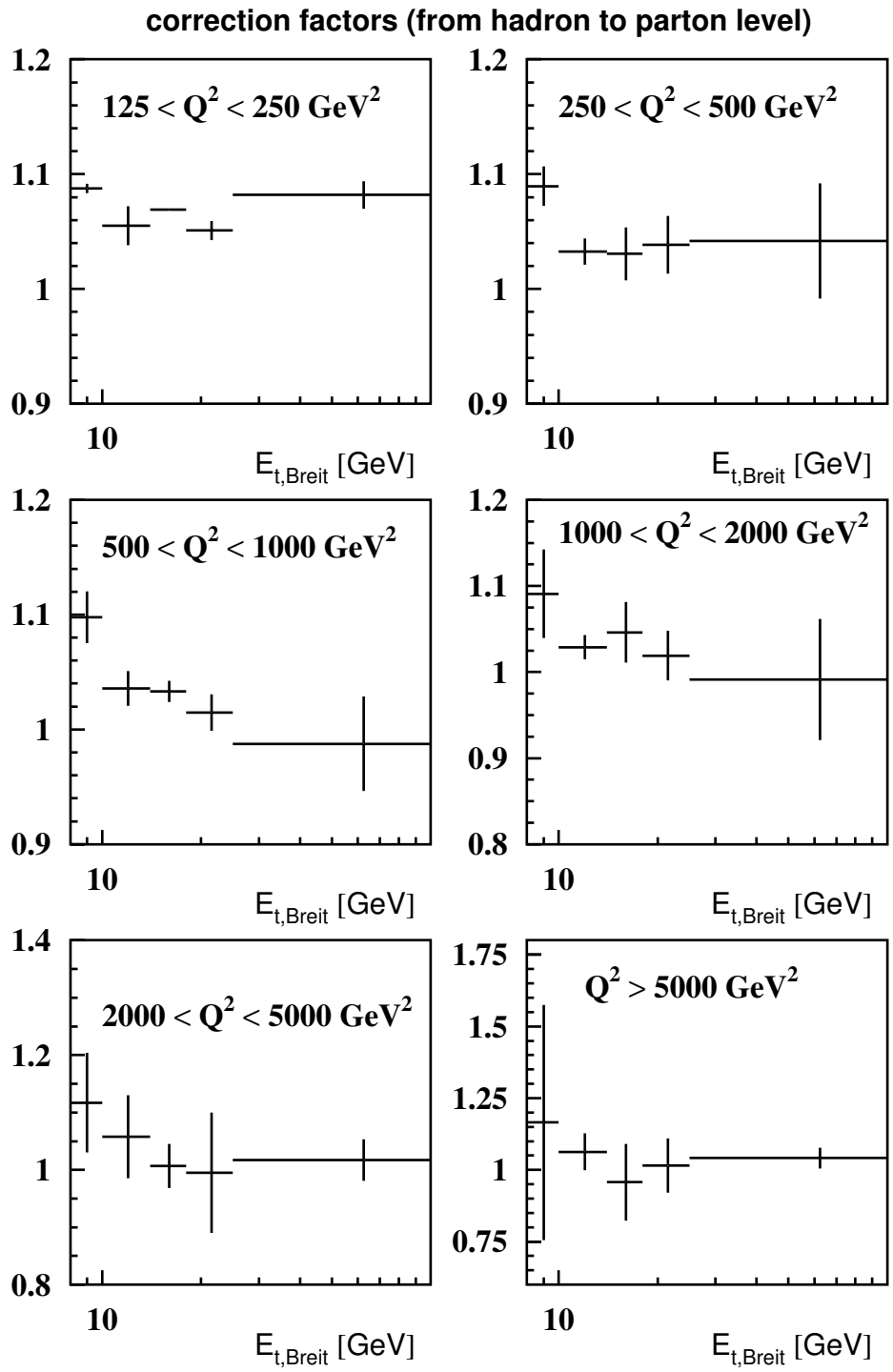

Figure 6.12: Hadronization corrections for the inclusive double differential jet cross sections $d^2\sigma/dE_{t,Breit}dQ^2$.

are rather flat. For lower $E_{t,Breit}$ there is a slight rise.

6.6 Systematic Studies

The systematic uncertainties for the determination of the inclusive jet cross sections arise from the uncertainty of the UCAL energy scale of $\pm$ 3% and from the differences of the correction factors from Ariadne and Lepto.

There are many different methods to determine the UCAL energy scale uncertainty of $\pm$ 3%. One method starts with determining the transverse momentum of the positron, p_t^{el}, and the transverse momentum of the hadronic final state, p_t^{had}, and calculating the ratio of these quantities. This is done for the data and Monte Carlo. Then the ratio data/MC is approximately one with an uncertainty of $\pm$ 3%. (The transverse momentum of the positron is supposed to balance the transverse momentum of the hadronic final state. Thus the ratio p_t^{el}/p_t^{had} is considered to be invariant.)

Fig. 6.13 shows the systematic uncertainties for the inclusive differential jet cross sections $d\sigma/dE_{t,Breit}$. The black (white) circles represent the upper (lower) relative uncertainties. These systematic errors are compared to the statistical errors represented by the shaded area. The first graph shows the relative deviations that are obtained by scaling $E_{t,Breit}$ and $E_{t,Lab}$ by a factor 1.03 and 1/1.03. The scaling is done for the data only. For most bins the deviations are larger than the statistical error but of the same order. The second graph is obtained by scaling the $E - P_Z$. Here the largest deviations are in the order of 1%. Thus the slight shift of the Monte Carlos with respect to the data shown in Fig. 6.4 gives rise to only a small systematic uncertainty. The third graph displays the relative deviations from scaling the energy of the positron, E_{el}. Here the effect of the scaling is neglegible for most bins. Only for the fourth and sixth bin the lower uncertainty is in the order of 0.5% and 1%, respectively. The last graph shows the deviations resulting from using Lepto instead of Ariadne for the correction of the data. In the third bin the cross section obtained with Lepto is about 5% higher and in the sixth bin it exceeds the cross section obtained with Ariadne by about 8%.

Fig. 6.14 shows the systematic uncertainties for the inclusive differential jet cross sections $d\sigma/dQ^2$. In the first graph the systematic uncertainty decreases for increasing Q^2. As it will be shown in the next chapter, the distribution for $d\sigma/dE_{t,Breit}$ becomes flatter for increasing Q^2. Thus by scaling $E_{t,Breit}$ fewer jets are gained for higher Q^2. As the last graph of Fig. 6.14 reveals, for the first, third and fifth bin Lepto has larger correction factors, whereas for the second and sixth bin the correction factors are lower. This observation will become important when in the next chapter the corrected data are compared to the results of the NLO calculations.

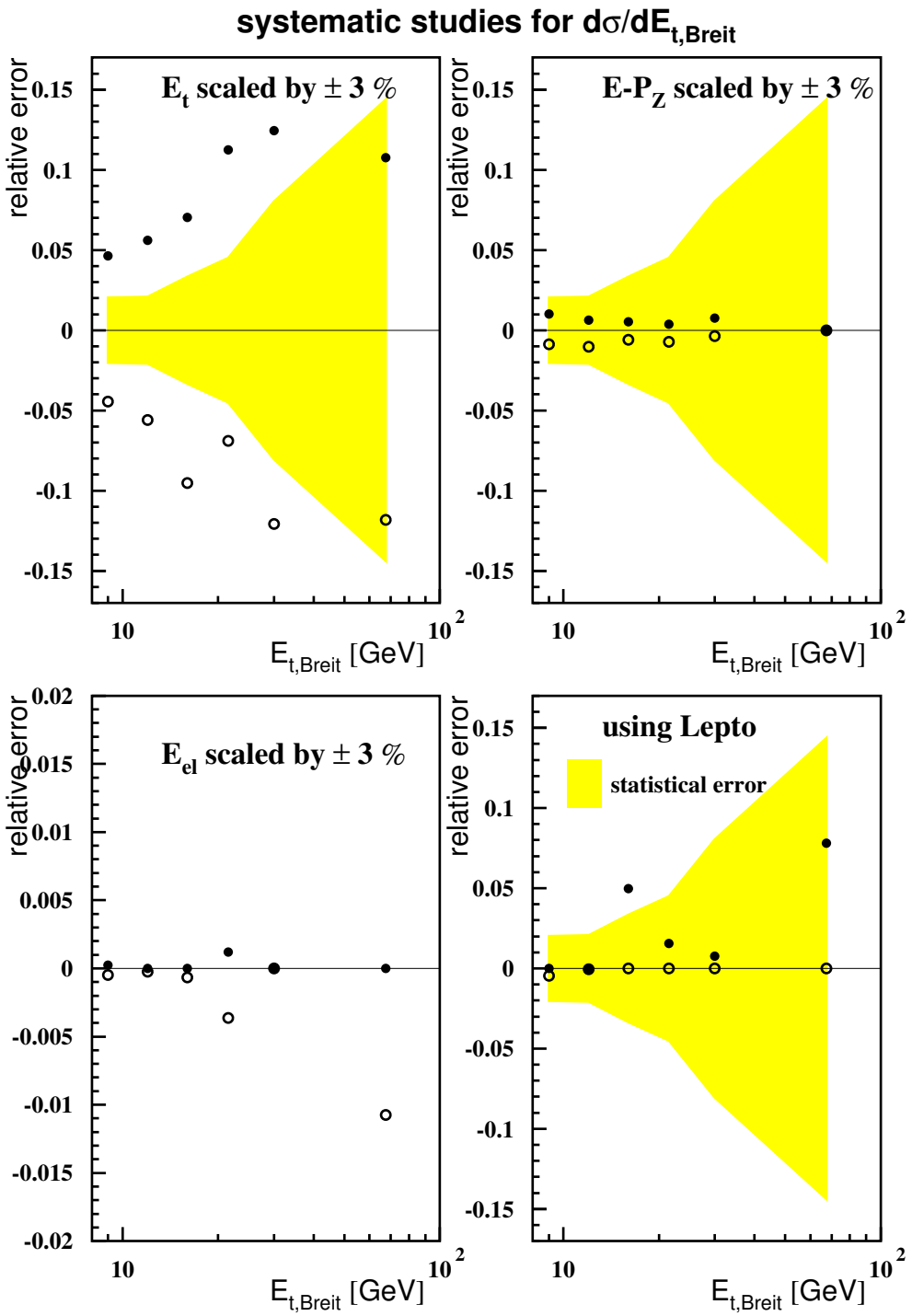

Figure 6.13: Systematic uncertainties for $d\sigma/dE_{t,Breit}$. The black (white) circles represent the upper (lower) systematic uncertainties. The shaded area represent the statistical errors. (In one figure the statistical errors are not displayed since the scale is much smaller.)

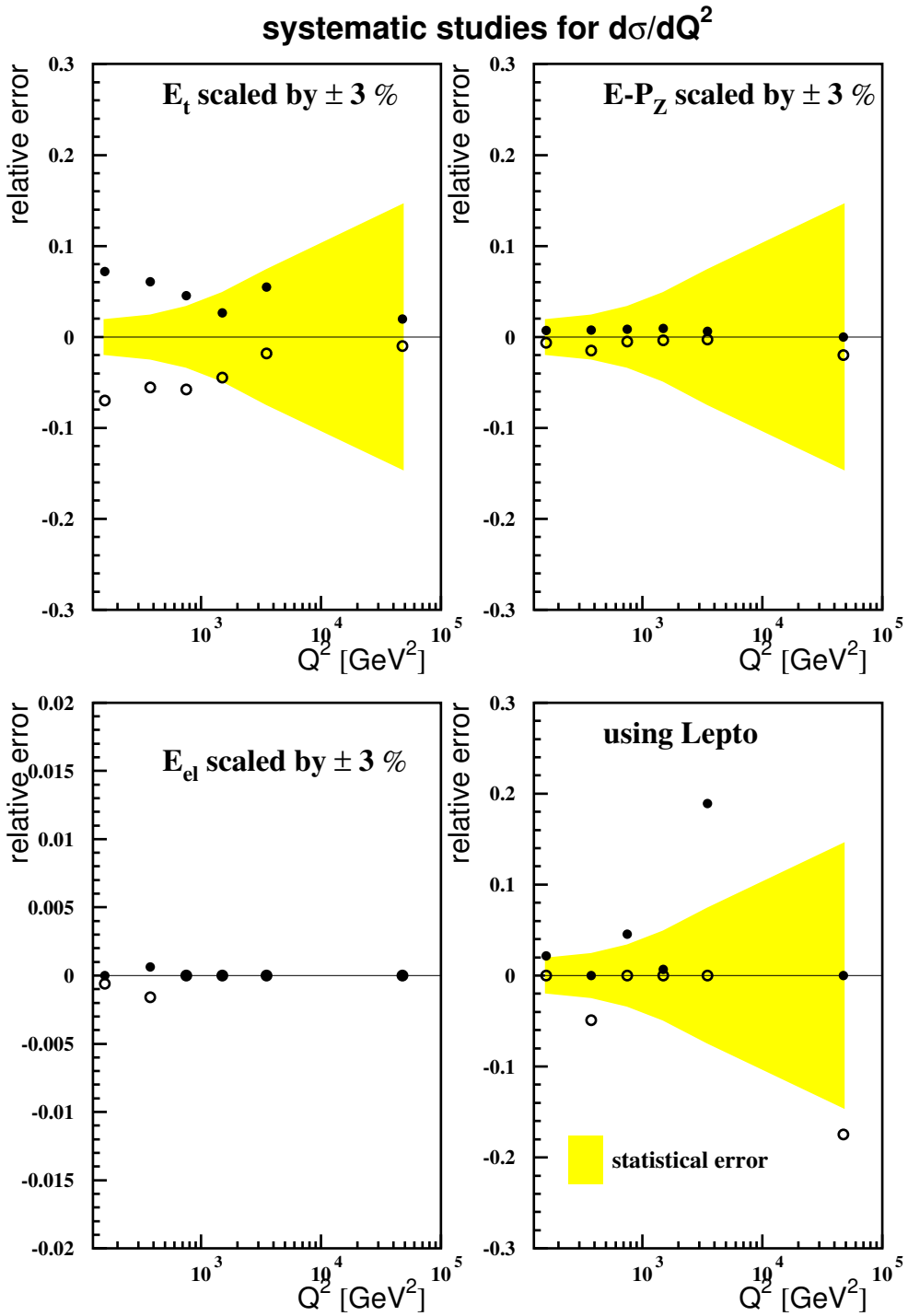

Figure 6.14: Systematic uncertainties for $d\sigma/dQ^2$. The black (white) circles represent the upper (lower) systematic uncertainties. The shaded area represent the statistical errors. (In one figure the statistical errors are not displayed since the scale is much smaller.)

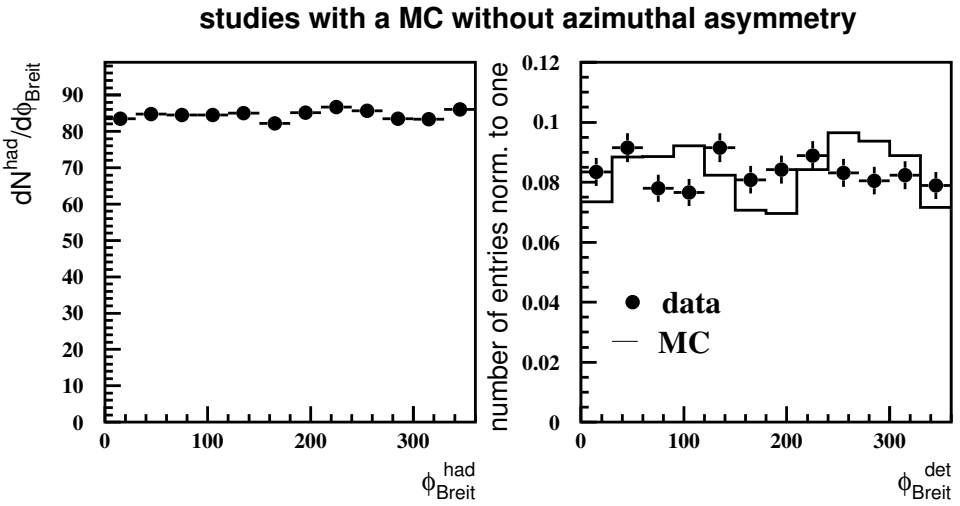

Figure 6.15: Studies with a Monte Carlo without azimuthal asymmetry. On the left the number of jets at hadron level divided by the bin width, $dN^{had}/d\phi_{Breit}$, is shown. On the right the data are compared to the Monte Carlo at detector level (comparison of the shape).

6.7 The Azimuthal Asymmetry

In Fig. 6.2 the data were compared to Ariadne and Lepto at detector level. Recall that the distribution for ϕ_{Breit} was rather flat and that there was an agreement between data and the Monte Carlos. In Fig. 6.9 the correction factors for $d\sigma/d\phi_{Breit}$ were shown. This distribution had the shape of the azimuthal asymmetry, i.e. there were peaks at 0° and 180°. Thus the reader may suspect that the azimuthal asymmtry is only obtained since the LO Monte Carlos have it at generator level. To convince the reader that the azimuthal asymmetry is actually measured, studies have been done with a LO Monte Carlo that has a flat ϕ_{Breit}-distribution at generator level (cf. Fig. 6.15 left hand side). This Monte Carlo was generated by Eduardo Rodrigues with a slightly changed version of Lepto-MEPS. As for Eduardo's analysis the phase space is different, the following additional cuts were applied for the comparison of the data with Eduardo's Monte Carlo:

$$0.01 < x < 0.1 \quad ; \quad 0.2 < y < 0.8 \quad ,$$

where x is the Bjorken x and y is the inelasticity. On the right hand side of Fig. 6.15 the data are compared to the Monte Carlo without azimuthal asymmetry (comparison of the shape). The distribution for ϕ_{Breit} reveals that for the Monte Carlo the region around 0° and 180° is depleted, whereas the data have a clearly different distribution. A Monte Carlo with azimuthal asymmetry has also been analysed with the additional phase space cuts mentioned above. It

describes the data much better. So there is no indication that the agreement or disagreement at detector level depends on the phase space.

However the reader may ask which cleaning cut prevents the observation of the azimuthal asymmetry at detector level and why the Monte Carlo without azimuthal asymmetry at generator level has less jets with a ϕ_{Breit} around 0° and 180°. The cleaning cut that causes these phenomena is the requirement that if there is a jet near the positron with a distance in the (η_{Lab}, ϕ_{Lab})-plane less than one, the whole event is discarded. It is obvious that this cut removes jets with $\phi_{Breit} \approx 0°$, since this is by definition the azimuthal angle of the positron in the Breit frame. As it was mentioned in the chapter on the theory, most of the accepted events have two jets with a high $E_{t,Breit}$. If one jet has $\phi_{Breit} \approx 0°$ the other jet must have $\phi_{Breit} \approx 180°$ in order to balance it. Thus if the whole event is discarded in the case of a jet being close to the positron, in most cases a second jet with $\phi_{Breit} \approx 180°$ is also removed. On the one hand it is true that the distribution of ϕ_{Breit} would peak around 0° and 180° if this cleaning cut was not applied. On the other hand Monte Carlo studies reveal that a great contribution to these peaks would come from initial and final state radiation.

Note that even if Eduardo's Monte Carlo was used to correct the data to hadron level, the azimuthal asymmetry would be obtained. So the conclusion of this section is that there is evidence that the rather flat distribution of ϕ_{Breit} is caused by the azimuthal asymmetry.

6.8 NLO Calculations

For the theoretical calculations the program DISENT was used. Forty million events were generated and analysed with this program to obtain the predictions to next to leading order in α_S for the inclusive jet cross sections. For the square of the factorisation scale, ${\mu_f}^2$, Q^2 was chosen. The relative uncertainty caused by the factorisation scale was found to be negligible (1% and below when μ_f was scaled by a factor 2). For the choice of the renormalization scale, μ_r, studies were undertaken to decide whether to set $\mu_r = E^{jet}_{t,Breit}$ or ${\mu_r}^2 = Q^2$. The latter choice defines μ_r for the whole event, whereas the first possibility defines μ_r for each jet. Since the distributions for the inclusive jet cross sections all contain one entry for each jet, μ_r is well defined in both cases. Fig. 6.16 illustrates the differences between the two choices. The left hand side refers to the inclusive differential jet cross sections $d\sigma/dE_{t,Breit}$, the right hand side to the inclusive differential jet cross sections $d\sigma/dQ^2$. On the top the relative uncertainty for $E_{t,Breit}/2 < \mu_r < E_{t,Breit} * 2$ is shown. In the centre the relative uncertainty for $Q^2/4 < (\mu_r)^2 < Q^2 * 4$ is displayed. On the bottom the points mark the ratios $(d\sigma/dE_{t,Breit}) \left|_{(\mu_r)^2=Q^2} / (d\sigma/dE_{t,Breit}) \right|_{\mu_r=E_{t,Breit}}$ and $(d\sigma/dQ^2) \left|_{(\mu_r)^2=Q^2} / (d\sigma/dQ^2) \right|_{\mu_r=E_{t,Breit}}$, respectively. The procedure by which the relative uncertainty is determined needs some explanation. Take as an example the figure at the top on the right hand side. At higher Q^2 there

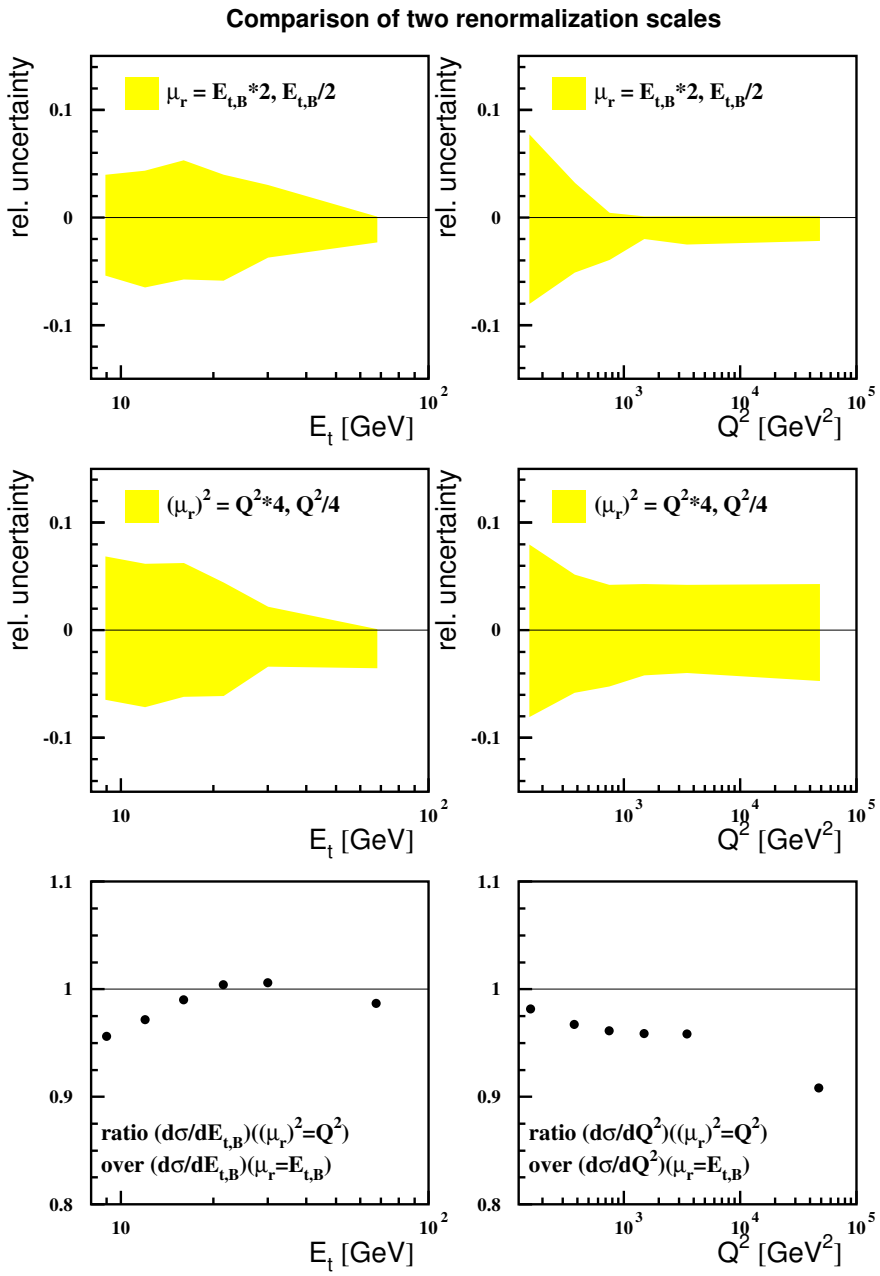

Figure 6.16: Comparison of the NLO results for two different choices for the renormalization scale. The left hand side refers to the inclusive differential jet cross sections $d\sigma/dE_{t,Breit}$, the right hand side to the inclusive differential jet cross sections $d\sigma/dQ^2$. On the top the relative uncertainty for $E_{t,Breit}/2 < \mu_r < E_{t,Breit} * 2$ is shown. In the center the relative uncertainty for $Q^2/4 < (\mu_r)^2 < Q^2 * 4$ is displayed. On the bottom the points mark the ratios $(d\sigma/dE_{t,Breit})\left|_{(\mu_r)^2=Q^2}\right. / (d\sigma/dE_{t,Breit})\left|_{\mu_r=E_{t,Breit}}\right.$ and $(d\sigma/dQ^2)\left|_{(\mu_r)^2=Q^2}\right. / (d\sigma/dQ^2)\left|_{\mu_r=E_{t,Breit}}\right.$, respectively.

is only a lower uncertainty. In this region the upper uncertainty is set to zero. As a matter of fact the cross sections, $d\sigma/dQ^2$, for $\mu_r = E_{t,Breit}/2$ and $\mu_r = E_{t,Breit} * 2$ were both lower than the cross section for $\mu_r = E_{t,Breit}$. Since there was no indication that there was an upper uncertainty, this quantity was set to zero. The lower uncertainty was taken from the larger deviation.

As can be seen from Fig. 6.16 the uncertainty for $d\sigma/dE_{t,Breit}$ at lower values of $E_{t,Breit}$ is a bit larger when Q^2 is chosen as the renormalization scale. For $d\sigma/dQ^2$ the uncertainty is larger at higher values of Q^2 when Q^2 is chosen as the renormalization scale. In this case there is an upper uncertainty that is not equal to zero. In the regions where the difference between the uncertainties is larger the deviations of the central cross sections are larger as can be seen from the two graphs on the bottom. However, no choice can be ruled out since in both cases the uncertainties are not too large. The comparison with the data will show which alternative is to be prefered. As it will be shown in the next chapter the choice of $E_{t,Breit}$ as the renormalization scale gives a better description of the data.

Chapter 7

Results

7.1 Inclusive Jet Cross Sections

In this section the measured inclusive jet cross sections are presented and compared to NLO QCD predictions obtaind with the program DISENT. For comparison, the data and the NLO QCD predictions are corrected to hadron level without initial and final state QED radiation for a fixed value of the electromagnetic coupling constant, α. From Fig. 7.1 to Fig. 7.5 the differential inclusive jet cross sections $d\sigma/dQ^2$, $d\sigma/dE_{t,Breit}$, $d\sigma/d\eta^{Breit}$, $d\sigma/d\eta^{Lab}$, and $d\sigma/d\phi^{Breit}$ are presented. Q^2 is the virtuality of the exchanged boson (cf. Chapter 2) in an event where a jet has been selected. $E_{t,Breit}$ is the transverse energy of a jet in the Breit frame. η^{Breit} (η^{Lab}) denotes the pseudorapidity of a jet in the Breit (Laboratory) frame. ϕ^{Breit} is the azimuthal angle of a jet in the Breit frame. (The azimuthal angle of the scattered positron in the Breit frame is zero by construction.)

Note that the uncertainty due to the absolute energy scale of the jets has a large degree of correlation from bin to bin. In addition, there is a overall normalization uncertainty of 1.6% from the luminosity determination, which is not included. The NLO QCD calculations using the CTEQ5M parametrizations of the proton PDFs are shown for two choices of the renormalization scale. The calculations were performed in the $\overline{MS}$ renormalization and factorization scheme. The number of flavours was set to five. The strong coupling constant α_s was calculated at NLO with $\alpha_s(M_Z) = 0.118$.

In the figures showing (Data - Theory)/Theory the uncertainty of the NLO calculations has two contributions. One part of the uncertainty was estimated by scaling the renormalization scale by a factor two. The other part is due to the uncertainty of the hadronization correction. These two contributions have been added in quadrature.

The measured $d\sigma/dQ^2$ ($d\sigma/dE_{t,Breit}$) exhibits a steep fall-off over five (three) orders of magnitude in the Q^2 ($E_{t,Breit}$) range considered. The measured $d\sigma/d\eta^{Breit}$ displays a peak for $0.25 < \eta^{Breit} < 1$ and decreases rapidly for $\eta^{Breit} < 0$. The values for $d\sigma/d\eta^{Lab}$ have a peak for $0 < \eta^{Lab} < 1$ and decrease rapidly for smaller and larger values (The decrease for smaller values is a bit steeper than for higher values.). The low value for the cross section in the

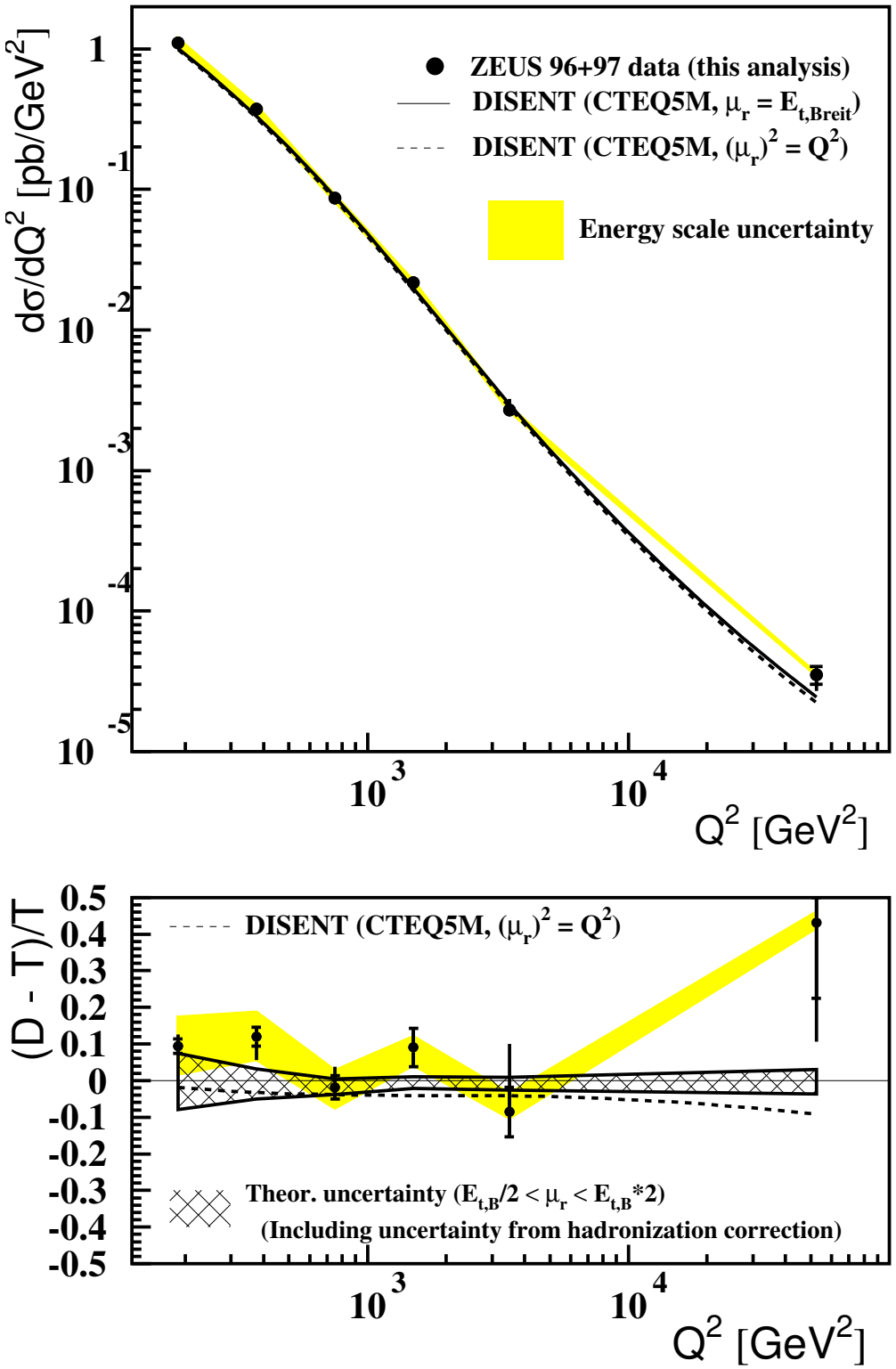

Figure 7.1: (top) Measured differential cross sections $d\sigma/dQ^2$ for inclusive jet production (black dots). The error bars represent the statistical errors and systematic uncertainties added in quadrature. The shaded band displays the uncertainty due to the absolute energy scale of the jets. The NLO QCD calculations using the CTEQ5M parametrizations of the proton PDFs are shown for two choices of the renormalization scale. (bottom) The quantity (Data - Theory)/Theory; the hatched band displays the uncertainty of the NLO QCD calculations.

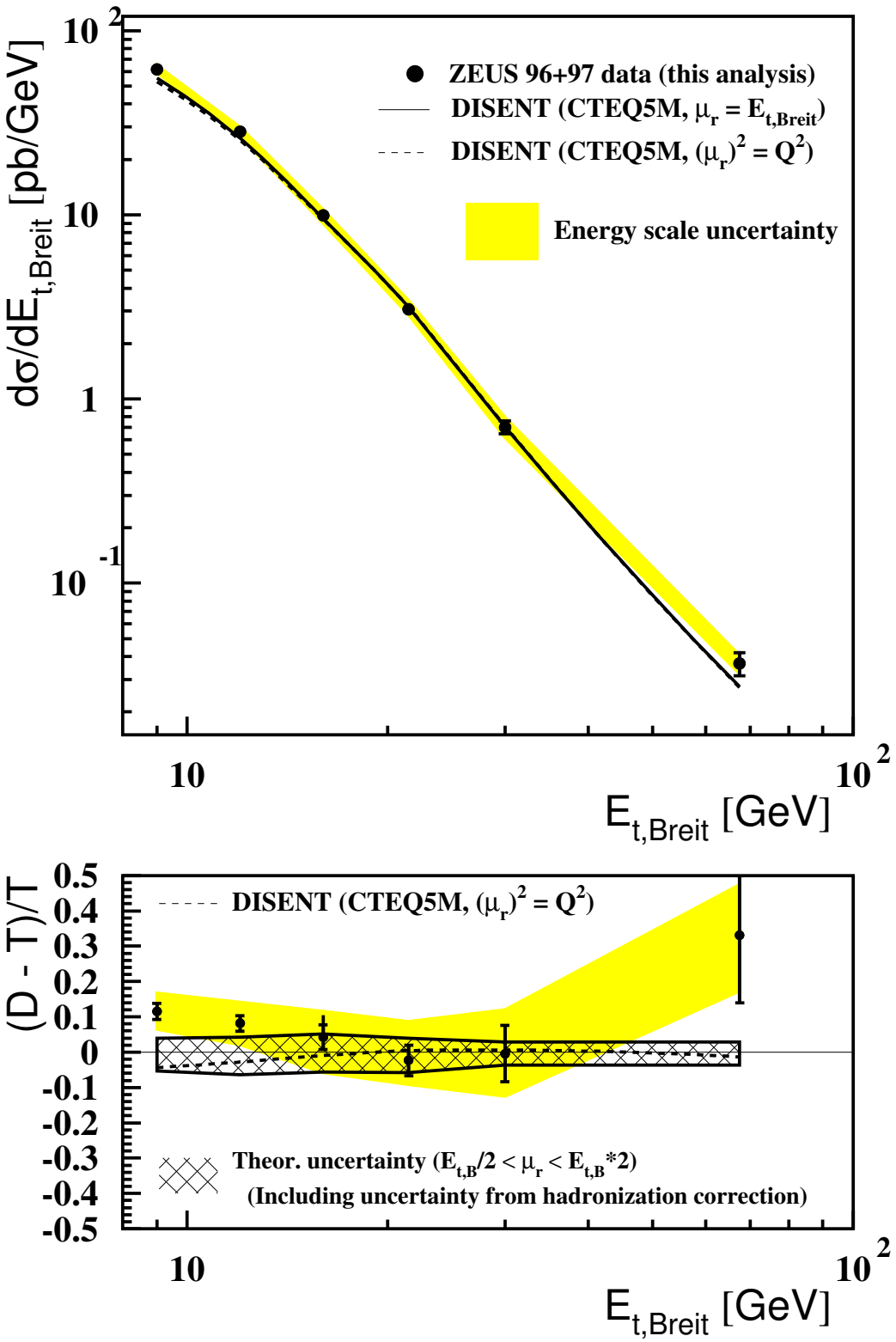

Figure 7.2: (top) Measured differential cross sections $d\sigma/dE_{t,Breit}$ for inclusive jet production (black dots), where $E_{t,Breit}$ denotes the transverse energy of a jet in the Breit frame. The error bars represent the statistical errors and systematic uncertainties added in quadrature. The shaded band displays the uncertainty due to the absolute energy scale of the jets. The NLO QCD calculations using the CTEQ5M parametrizations of the proton PDFs are shown for two choices of the renormalization scale. (bottom) The quantity (Data - Theory)/Theory; the hatched band displays the uncertainty of the NLO QCD calculations.

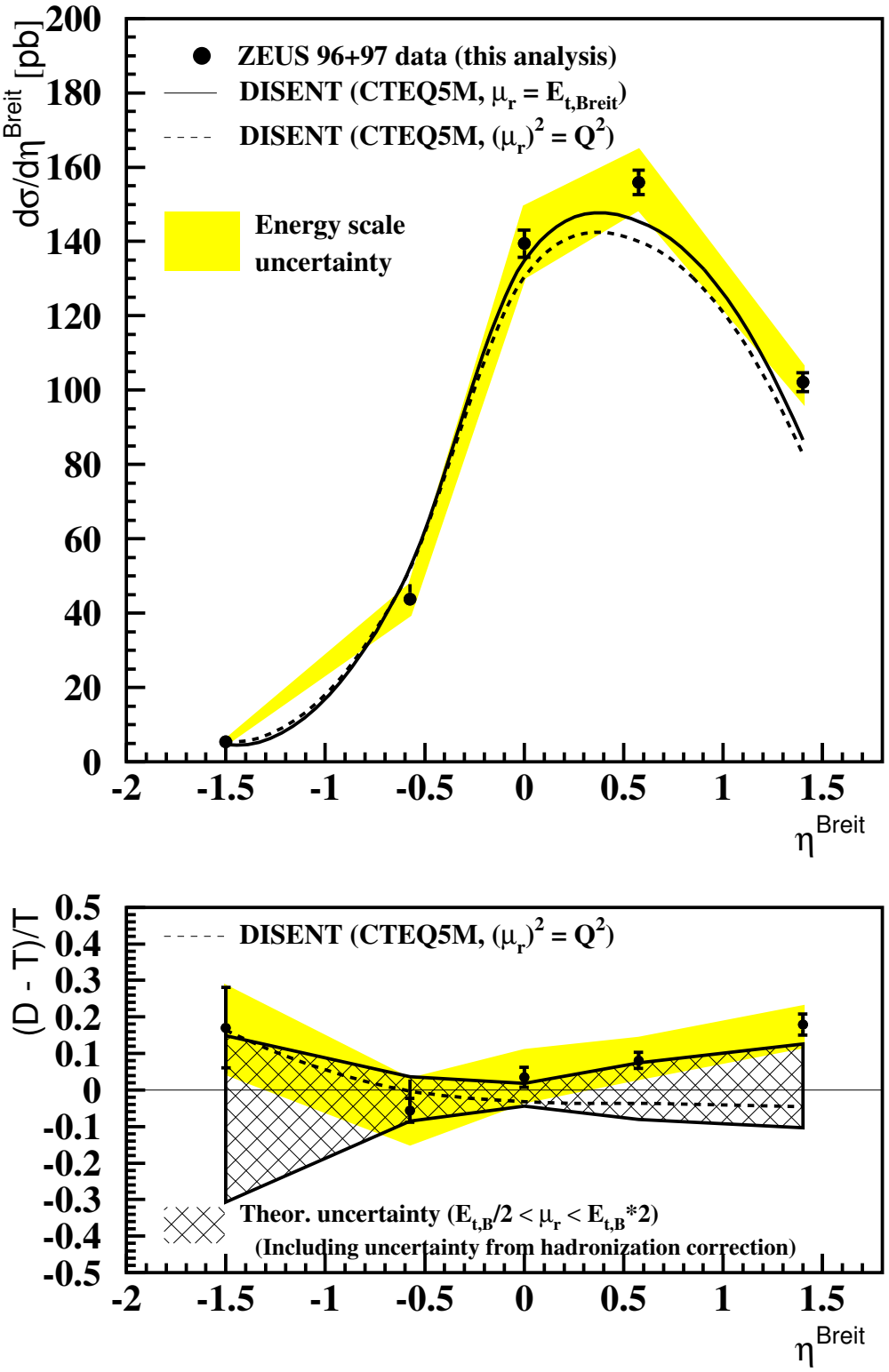

Figure 7.3: (top) Measured differential cross sections $d\sigma/d\eta^{Breit}$ for inclusive jet production (black dots), where η^{Breit} denotes the pseudorapidity of a jet in the Breit frame. The error bars represent the statistical errors and systematic uncertainties added in quadrature. The shaded band displays the uncertainty due to the absolute energy scale of the jets. The NLO QCD calculations using the CTEQ5M parametrizations of the proton PDFs are shown for two choices of the renormalization scale. (bottom) The quantity (Data - Theory)/Theory; the hatched band displays the uncertainty of the NLO QCD calculations.

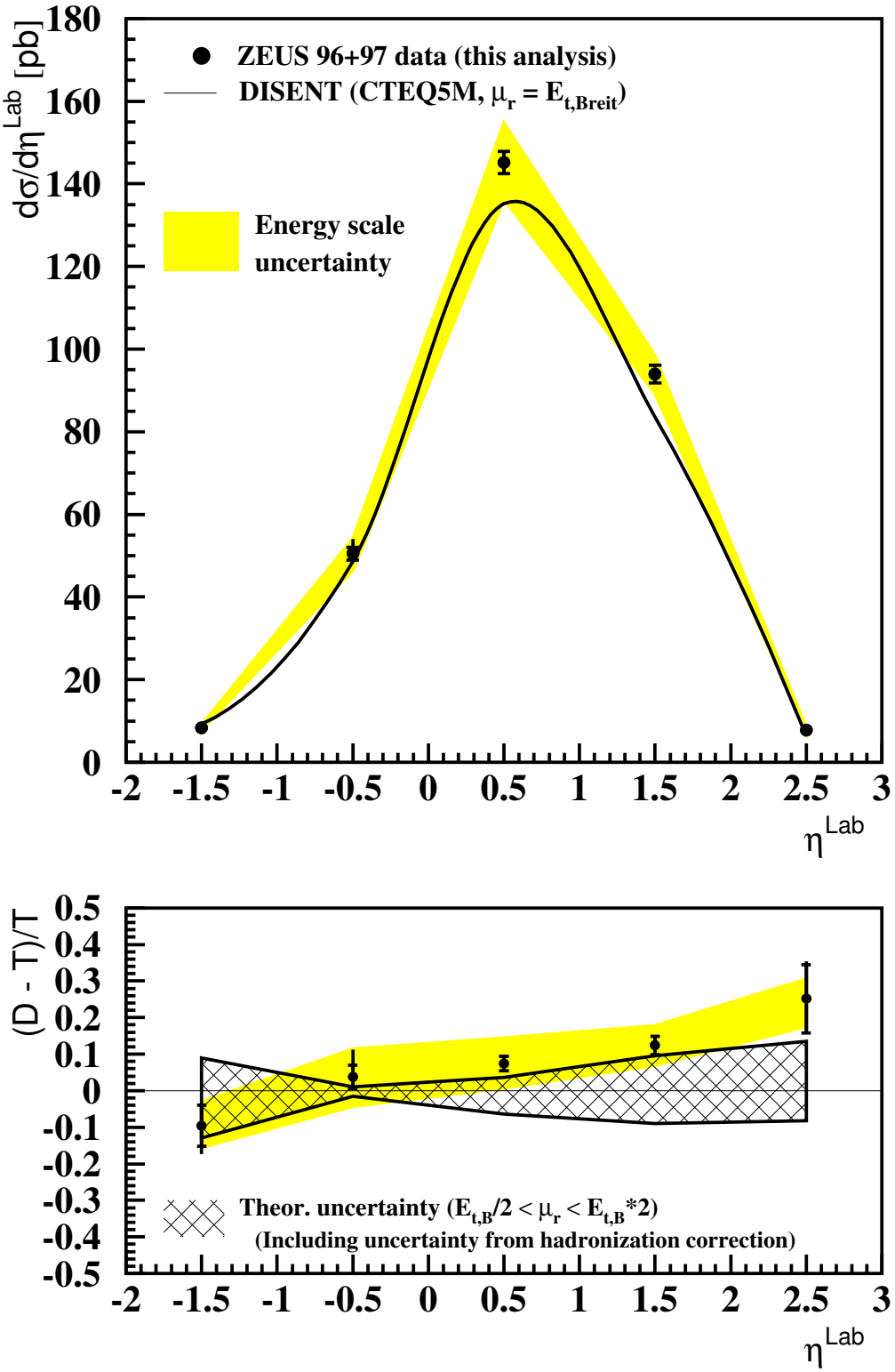

Figure 7.4: (top) Measured differential cross sections $d\sigma/d\eta^{Lab}$ for inclusive jet production (black dots), where η^{Lab} denotes the pseudorapidity of a jet in the Laboratory frame. The error bars represent the statistical errors and systematic uncertainties added in quadrature. The shaded band displays the uncertainty due to the absolute energy scale of the jets. The NLO QCD calculations using the CTEQ5M parametrizations of the proton PDFs ar shown. (bottom) The quantity (Data - Theory)/Theory; the hatched band displays the uncertainty of the NLO QCD calculations.

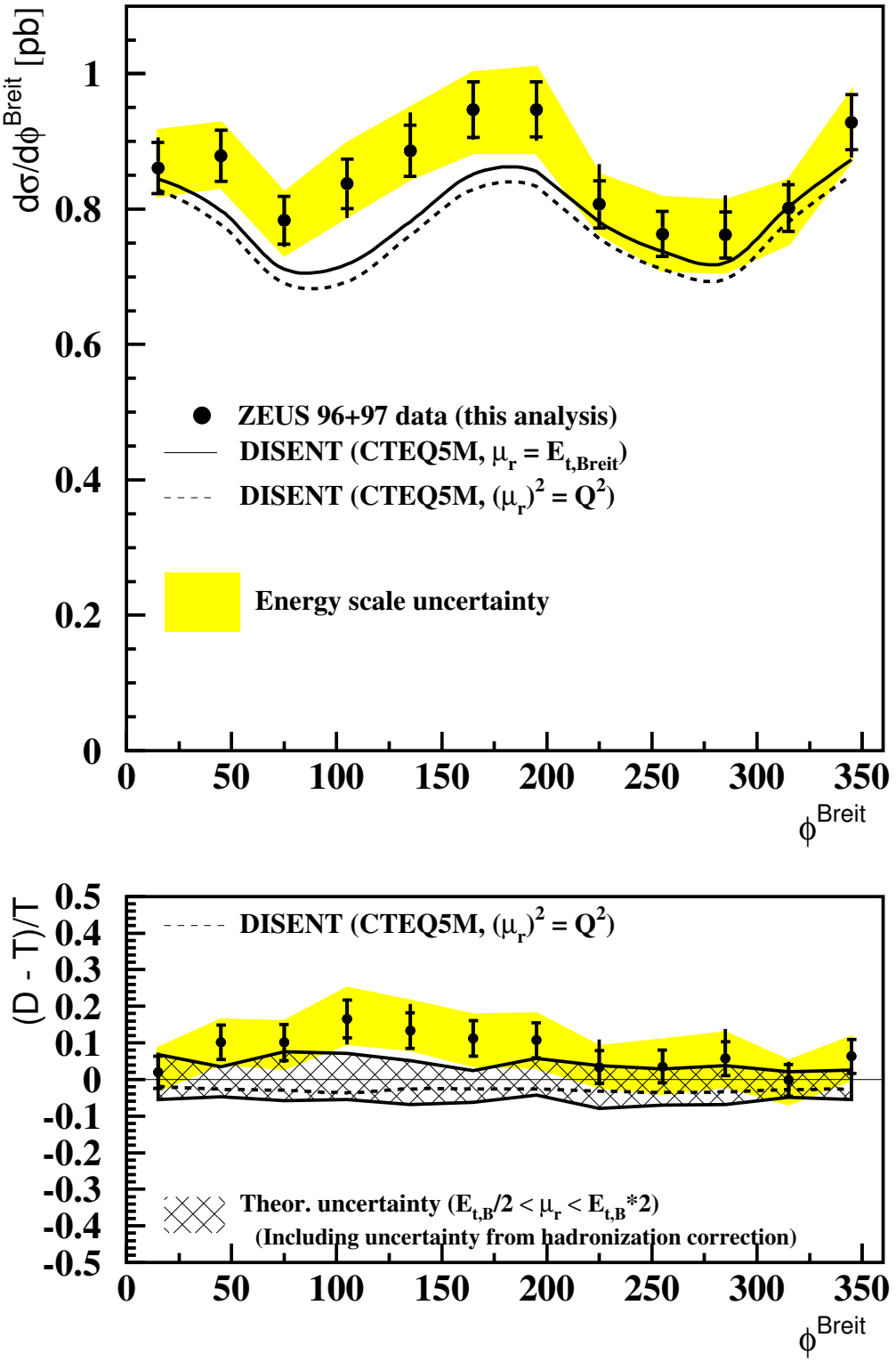

Figure 7.5: (top) Measured differential cross sections $d\sigma/d\phi^{Breit}$ for inclusive jet production (black dots), where ϕ^{Breit} denotes the azimuthal angle of a jet in the Breit frame. The error bars represent the statistical errors and systematic uncertainties added in quadrature. The shaded band displays the uncertainty due to the absolute energy scale of the jets. The NLO QCD calculations using the CTEQ5M parametrizations of the proton PDFs are shown for two choices of the renormalization scale. (bottom) The quantity (Data - Theory)/Theory; the hatched band displays the uncertainty of the NLO QCD calculations.

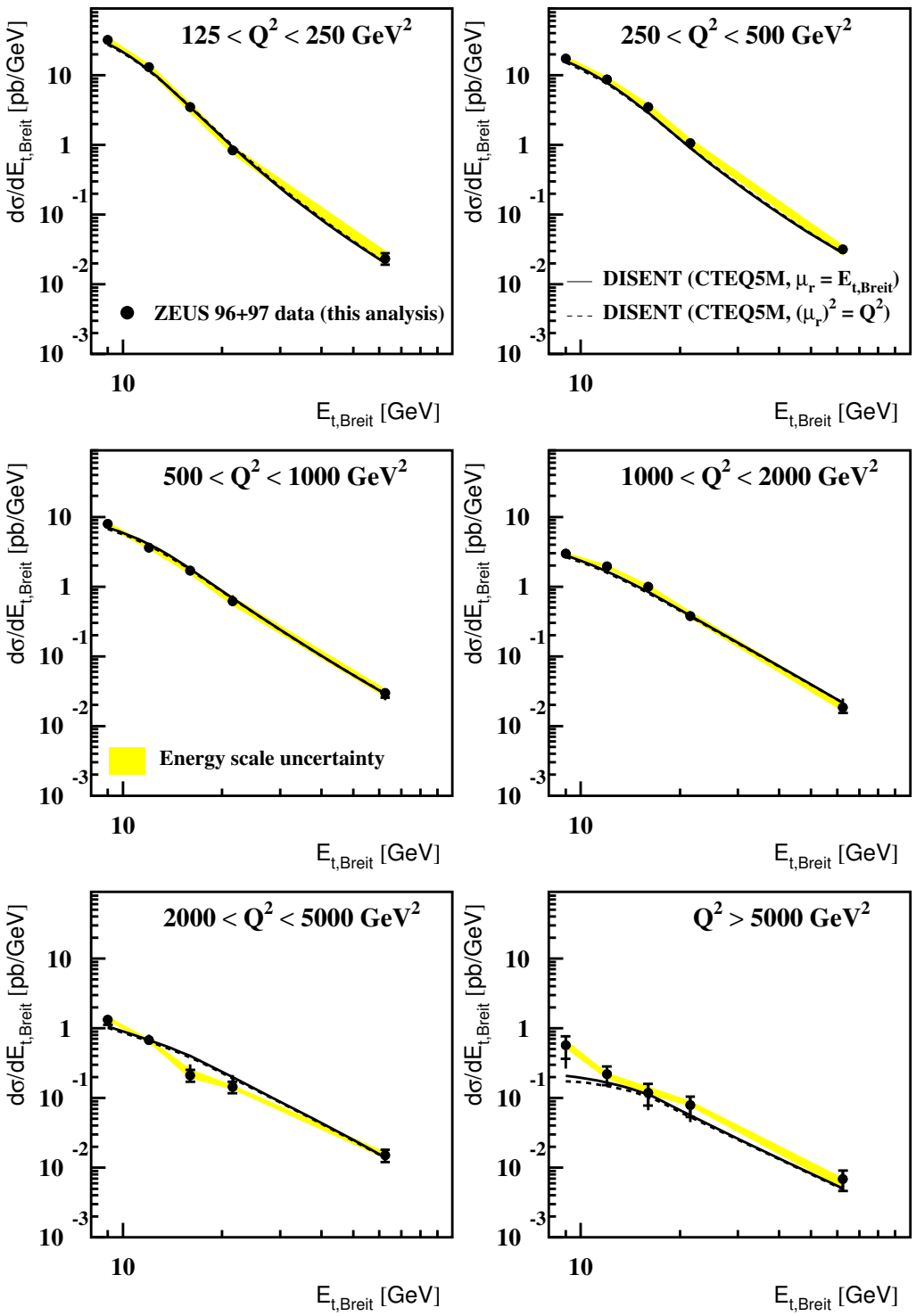

Figure 7.6: Measured differential cross sections $d\sigma/dE_{t,Breit}$ for inclusive jet production in differnt regions of Q^2 (black dots). The error bars represent the statistical errors and systematic uncertainties added in quadrature. The shaded band displays the uncertainty due to the absolute energy scale of the jets. The NLO QCD calculations using the CTEQ5M parametrizations of the proton PDFs are shown for two choices of the renormalization scale.

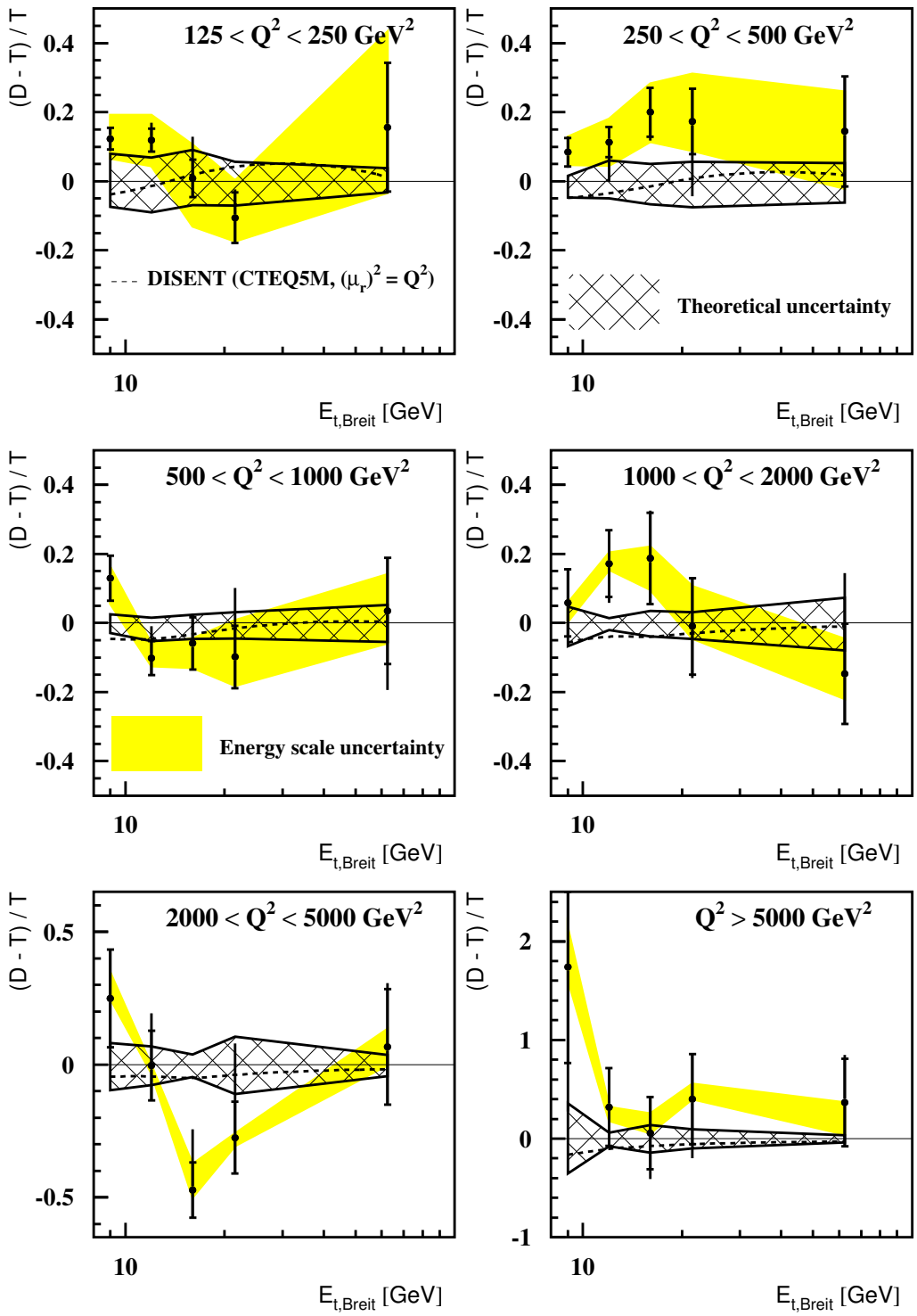

Figure 7.7: The quantity (Data - Theory)/Theory for $d\sigma/dE_{t,Breit}$ in different regions of Q^2 presented in Fig. 7.6; the hatched band displays the uncertainty of the NLO QCD calculations.

range $2 < \eta^{Lab} < 3$ is certainly due to the fact that there are very few jets selected with $\eta^{Lab} > 2.5$. The measured $d\sigma/d\phi^{Breit}$ is non constant and displays peaks at $\phi^{Breit} \sim 0°$ and 180°.

The comparison with the results of the NLO QCD calculations reveals that the agreement is good for high Q^2 ($Q^2 > 500$ GeV^2 or high $E_{t,Breit}$ ($E_{t,Breit} > 14$ GeV). The agreement observed at high Q^2 complements[1] and extends a similar comparison for the differential exclusive dijet cross sections at $Q^2 > 470$ GeV^2 [55]. At low Q^2 and low $E_{t,Breit}$ the measurements of inclusive jet cross sections are slightly above the calculations (by about 10%). The choice $(\mu_r)^2 = Q^2$ would provide a poorer description of the data in this region since the predicted cross sections are even smaller. Note that for $d\sigma/dQ^2$ the agreement with NLO would be in general better if the data were corrected with the factors obtained from Lepto. For $d\sigma/d\eta^{Breit}$ there is a discrepancy of about 15% at $\eta^{Breit} \sim 1.4$, whereas the theoretical uncertainty is about 10%. For $d\sigma/d\eta^{Lab}$ there is a difference of about 20% in the very forward region. However, the theoretical and statistical uncertainties are large in this region. The NLO QCD calculations describe the shape of the measured $d\sigma/d\phi^{Breit}$ well and show that the observed azimuthal dependence is compatible with that expected from QCD. This observation complements the measurement of the azimuthal dependence in neutral current DIS of charged hadrons with high transverse momentum [26].

The measurements of the differential cross section $d\sigma/dE_{t,Breit}$ in different regions of Q^2 are presented in Fig. 7.6. It is observed that the $E_{t,Breit}$ dependence becomes less steep as Q^2 increases. In Fig. 7.7 the ratios (Data - Theory)/Theory for these cross sections are shown. Within the errors the measured data are adequately described by NLO QCD.

7.2 Determination of α_s

After having measured the inclusive jet cross sections in the Breit frame it is only a relatively small further step to determine α_s from these values. In order to do this the cross sections for five proton PDFs (CTEQ4A1-A5) for five different values of α_s were calculated using DISENT:

$$\alpha_s(M_Z) = 0.110042, 0.113029, 0.116016, 0.118987, 0.122065$$

For each cross section there are five values depending on a certain value of α_s. A straight line fit was applied to these values. Thus a function was obtained, e.g.

$$\left(\frac{d\sigma}{dQ^2}\right)_i (\alpha_s(M_Z)),$$

[1] In the Breit frame the net transverse momentum of the hadronic final state is zero. Therefore, an event with a single jet, according to the jet selection criteria, must contain another jet(s) balancing its transverse momentum.

where the index i indicates that there is a function for each bin. Such a function had to be inverted to determine a certain value of $\alpha_s(M_Z)$ from a measured cross section. (Of course the results of the NLO QCD calculations as well as the measured cross sections first had to be corrected to the hadron level.) This procedure correctly handles the complete α_s-dependence of the NLO differential cross sections (the explicit dependence coming from the partonic cross sections and the implicict one coming from the PDFs) in the fit, while preserving the correlation between α_s and the PDFs. The NLO QCD calculations for this section as well as the parameters of the straight line fits were supplied to the author by Oscar Gonzalez.

Suppose that for the bin i a central value of $\alpha_s(M_Z)$ denoted by a_i has been obtained. Then suppose that another value of $\alpha_s(M_Z)$ has been determined for a measured cross section this time corrected to hadron level by Lepto. This value shall be denoted by a_i^L. Then the systematic error arising from this source, s_i^L, simply is $s_i^L = a_i^L - a_i$. This procedure is repeated for every source of systematic uncertainty. The deviations from the central value a_i are then added in quadrature to give the total experimental systematic error. To determine one part of the theoretical error the NLO QCD calculations were repeated with the renormalization scale, μ_r, set to $\mu_r = E_{t,Breit}/2$ and $\mu_r = E_{t,Breit} * 2$. A function for the cross section depending on $\alpha_s(M_Z)$ was again determined by a straight line fit. The result for $\alpha_s(M_Z)$ from these fits was again compared with the central value a_i and the difference regarded as one part of the theoretical error. The other part of the theoretical error was the uncertainty arising from the hadronization correction. The deviations from these two sources were added in quadrature to give the total theoretical error.

In Fig. 7.8 and Fig. 7.9 the values of $\alpha_s(M_Z)$ are shown obtained with the differential inclusive jet cross sections $d\sigma/dQ^2$ and $d\sigma/dE_{t,Breit}$, respectively. The inner error bar represents the statistical error, the outer error bar displays the statistical and experimental systematic error added in quadrature. The dashed line slightly underneath represents the theoretical error. The values are compared to the world average determined by S. Bethke [56]. As can be seen from these figures, for high Q^2 ($Q^2 > 500$ GeV^2) and high $E_{t,Breit}$ ($E_{t,Breit} > 14$ GeV) the values of $\alpha_s(M_Z)$ agree within the errors with the world average. For low Q^2 and low $E_{t,Breit}$ systematic errors dominate. In these regions the values of α_s are a bit higher than the world average.

In order combine the results for various bins, the quantity χ^2 was minimized. It is defined by

$$\chi^2(a) = \sum \frac{(a_i - a)^2}{{\Delta_i}^2}.$$

$$\frac{\partial \chi^2}{\partial a} = 0 \quad \Rightarrow \quad a = \frac{\sum \frac{a_i}{{\Delta_i}^2}}{\sum \frac{1}{{\Delta_i}^2}} \quad ; \quad \Delta a = \frac{1}{\sqrt{\sum \frac{1}{{\Delta_i}^2}}}$$

In the mathematical expressions above the sum is taken over all bins i considered. The symbol a denotes the value of α_s which is the result of the combination. The symbol Δ_i is the statistical error of the bin i which is con-

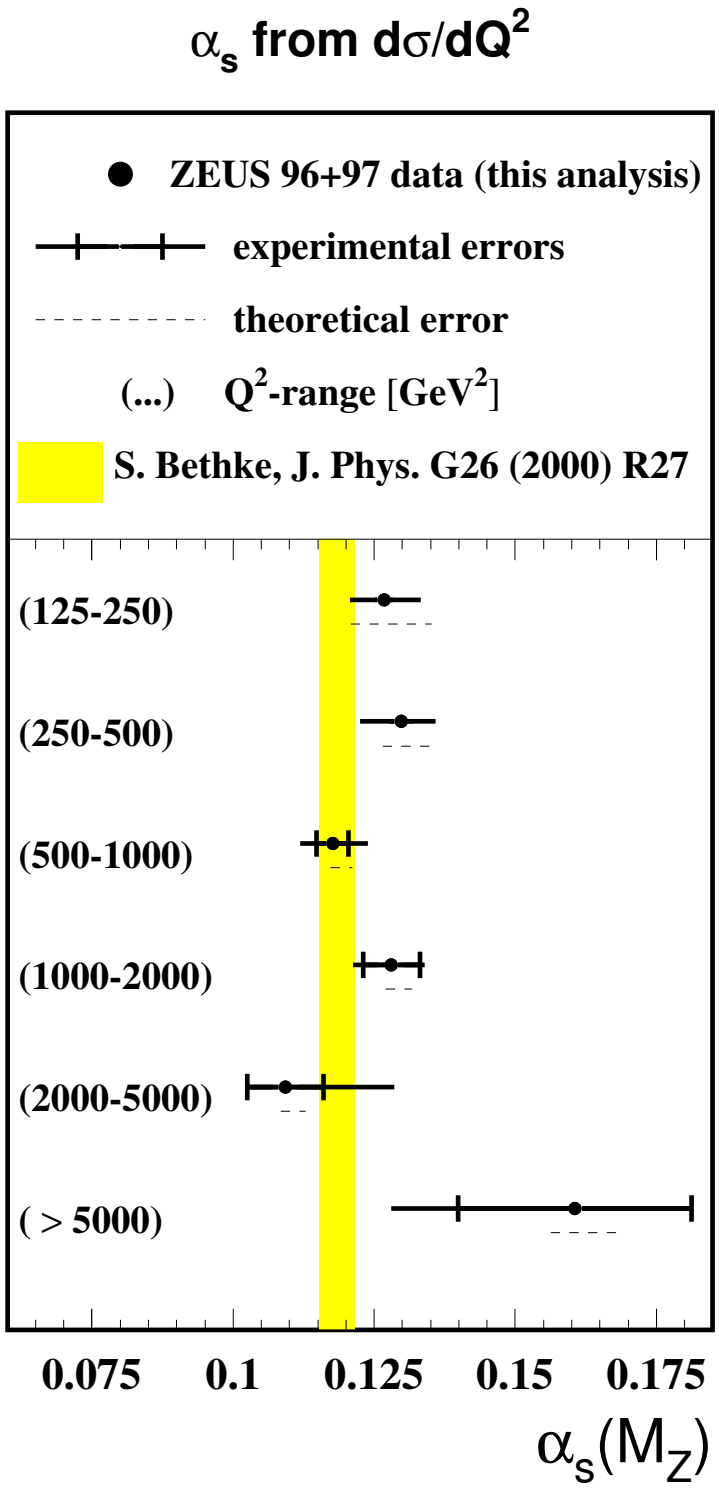

Figure 7.8: The values of $\alpha_s(M_Z)$ from $d\sigma/dQ^2$. The inner error bar represents the statistical error. The outer error bar displays the statistical error and experimental systematic error added in quadrature. The dashed line represents the theoretical error including the uncertainty of the hadronization correction. The shaded band shows the world average and its uncertainty as determined by S. Bethke.

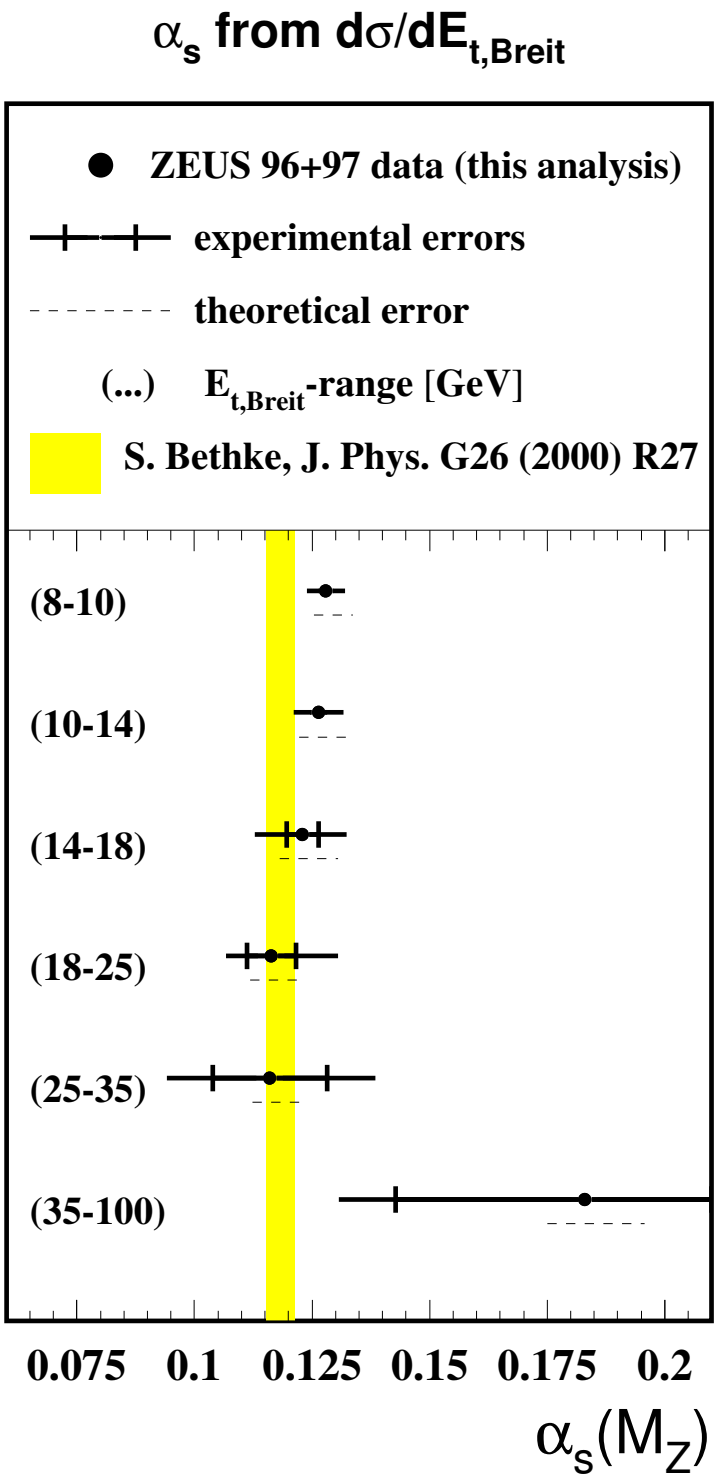

Figure 7.9: The values of $\alpha_s(M_Z)$ from $d\sigma/dE_{t,Breit}$. The inner error bar represents the statistical error. The outer error bar displays the statistical error and experimental systematic error added in quadrature. The dashed line represents the theoretical error including the uncertainty of the hadronization correction. The shaded band shows the world average and its uncertainty as determined by S. Bethke.

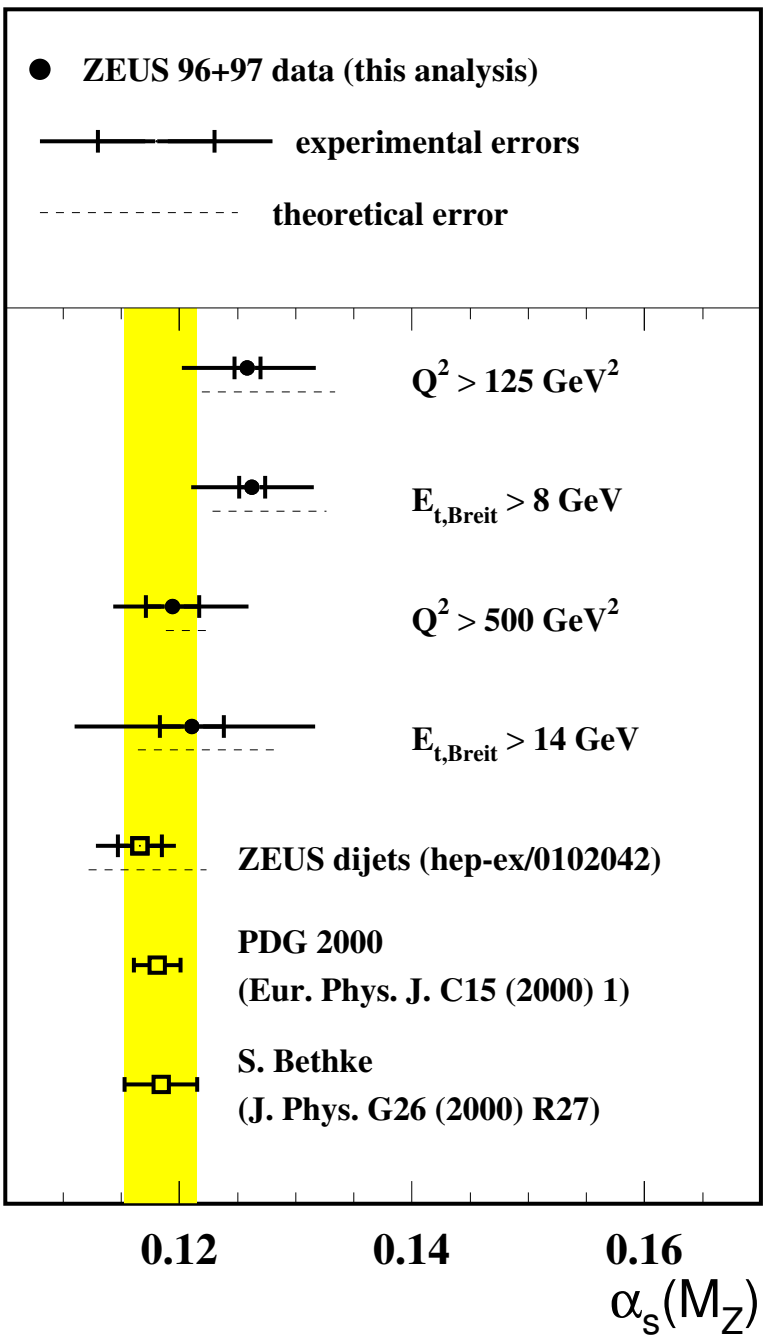

Figure 7.10: The values of α_s from combining values from Fig. 7.8 and Fig. 7.9. The inner error bar represents the statistical error. The outer error bar displays the statistical error and experimental systematic error added in quadrature. The dashed line represents the theoretical error including the uncertainty of the hadronization correction. Also shown is the result of a recently published dijet analysis. The shaded band refers to the world average determined by S. Bethke. The world average of the Particle Data Group is additionally displayed.

sidered to be the only uncorrelated error. Finally Δa is the statistical error of a. To understand how the experimental systematic error of a is determined, consider again the quantities a_i^L introduced above. In the definition of χ^2 the a_i are replaced by the a_i^L and a new result a^L is calculated. The difference $a^L - a$ is the systematic error for this source of uncertainty. The sum of all systematic uncertainties added in quadrature is quoted as the total experimental systematic error. To determine the theoretical error, the quantities a_i' and Δ_i' are calculated from the new theoretical input (e.g. for the theoretical values obtained with $\mu_r = E_{t,Breit}/2$) and from minimizing again χ^2 a new value for α_s, a', is obtained. The deviations of the various a' from a added in quadrature are the total theoretical error.

In Fig. 7.10 the results for $\alpha_s(M_Z)$ calculated from the previous values are shown. Again the shaded band indicates the world average and its uncertainty determined by S. Bethke. For $Q^2 > 125$ GeV^2 and $E_{t,Breit} > 8$ GeV the values of α_s are slightly above the world average. The experimental error for these points is dominated by systematic uncertainties. Theoretical errors for these points are relatively large. The value for $Q^2 > 500$ GeV^2 is in good agreement with the world average. The value and its errors are

$$\alpha_s(M_Z) = 0.1194 \pm 0.0023(stat.)^{+0.0061}_{-0.0045}(exp.)^{+0.0036}_{-0.0006}(th.).$$

Notice the small theoretical uncertainty. The value of α_s for $E_{t,Breit} > 14$ GeV is also in good agreement with the world average. However, in this case the experimental systematic error and the theoretical uncertainty is relatively large. Also shown in Fig. 7.10 is the world average of the Particle Data Group (PDG) [57]. The uncertainty of their value for α_s is smaller than the one given by Bethke. In the determination of the PDG the correlation of the errors of the various analyses is not taken into account.

7.3 Comparison with H1

This section refers to the Ph.D. thesis of Markus Wobisch [58] and two publications of the H1 Collaboration [59, 60]. (The thesis and the later H1 publication have the same title.) In these publications inclusive jet cross sections were presented measured with the H1 detector. The kinematic region in which the inclusive jet cross sections were measured is defined by

$$0.2 < y < 0.6 \quad \text{and} \quad 150 < Q^2 < 5000 \text{ GeV}^2,$$

where y is the inelasticity and Q^2 is the virtuality of the exchanged boson. The jets were selected with the criteria

$$-1 < \eta^{Lab} < 2.5 \quad \text{and} \quad 7 < E_{t,Breit} < 50 \text{ GeV},$$

where η^{Lab} is the pseudorapidity of a jet in the Laboratory frame and $E_{t,Breit}$ is the transverse energy of a jet in the Breit frame. Various jet algorithm were

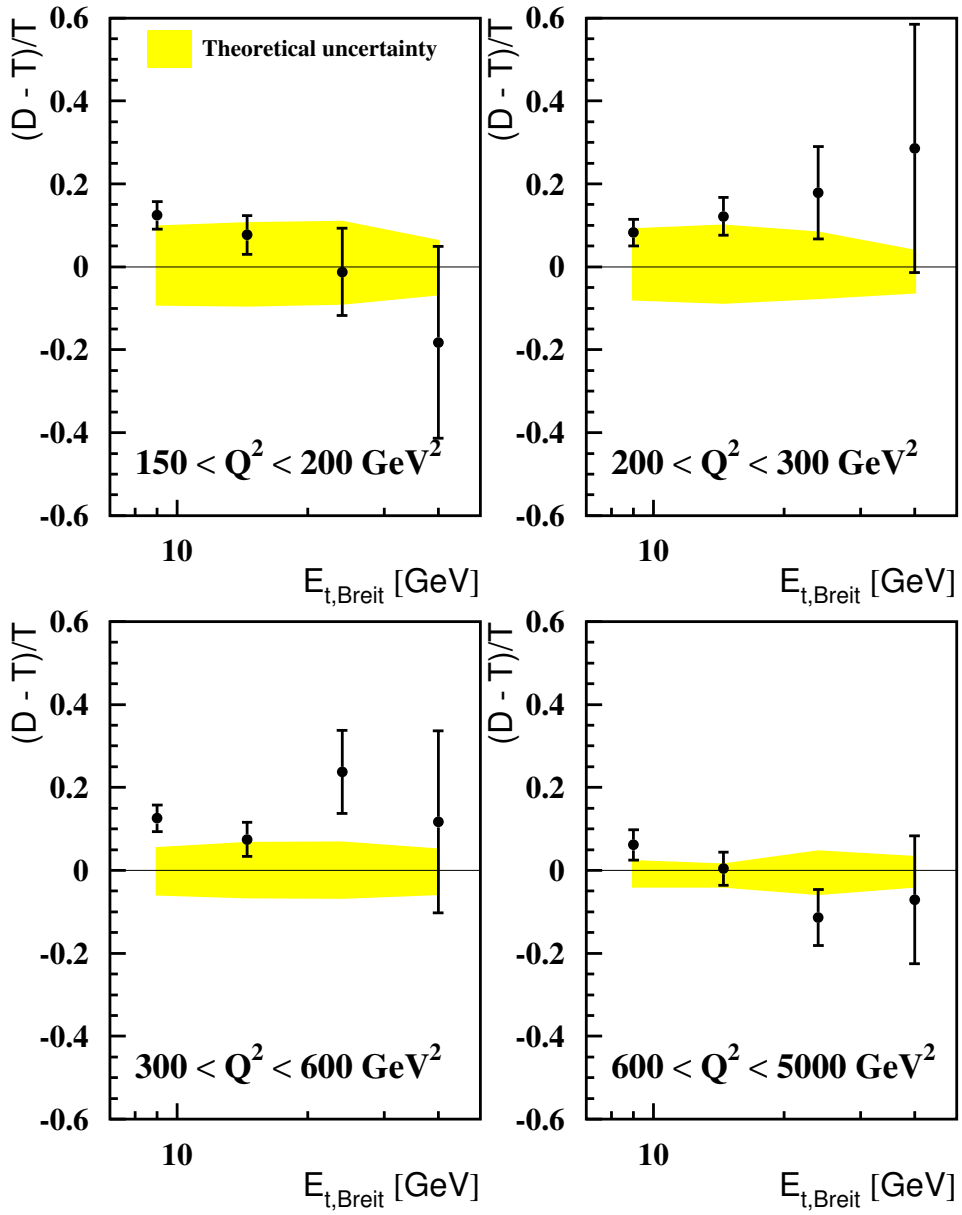

Figure 7.11: Comparison between the data and NLO QCD calculations for an analysis similar to one of H1. The ratio (Data - Theory)/Theory is shown for the double differential inclusive jet cross sections $d\sigma/dE_{t,Breit}dQ^2$. The error bars represent the statistical errors. The shaded band displays the theoretical error including the uncertainty due to the hadronization correction.

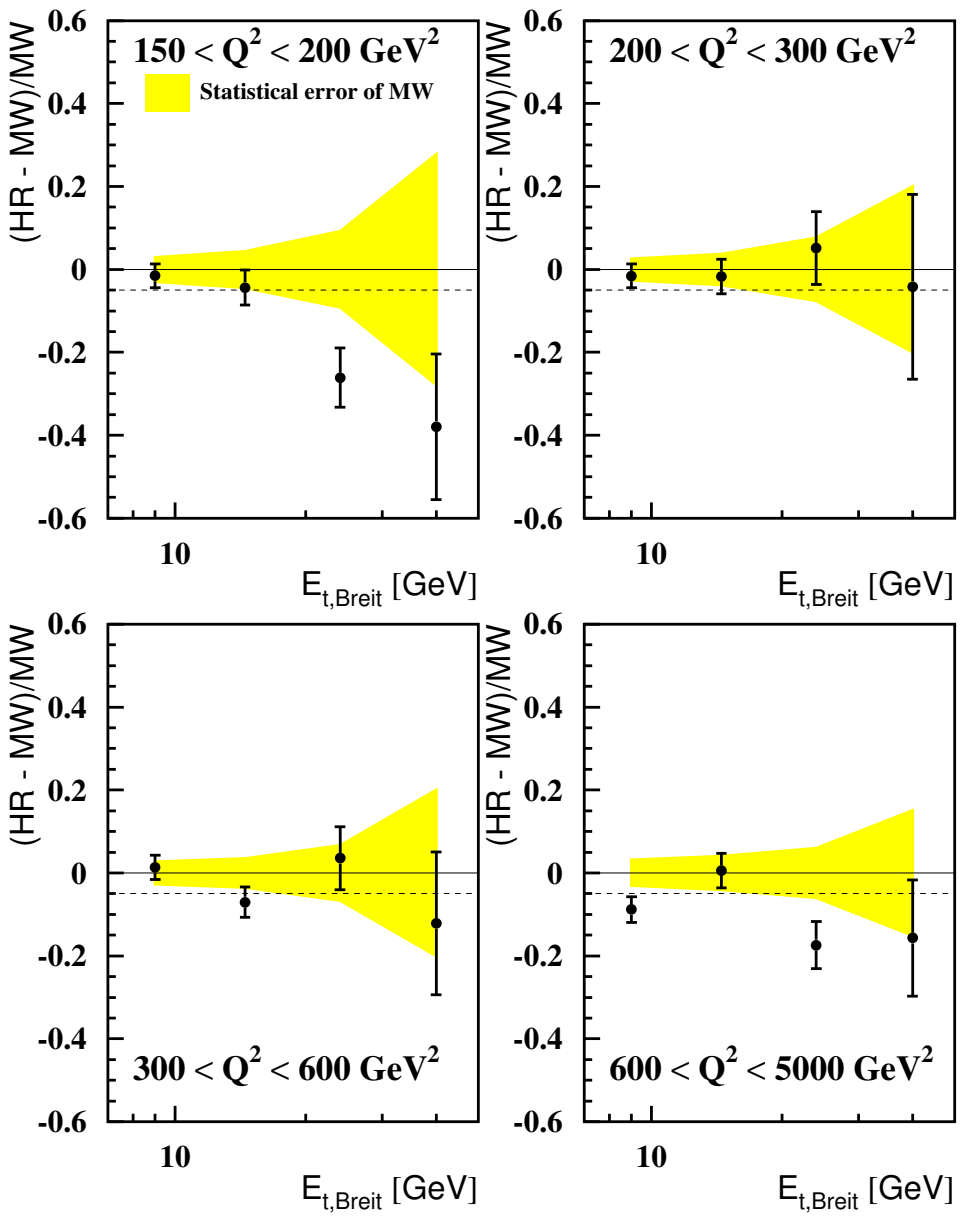

Figure 7.12: Comparison with the results of Markus Wobisch for the double differential inclusive jet cross sections $d\sigma/dE_{t,Breit}dQ^2$. The selection criteria for the phase space and the jets are those of Markus Wobisch. The error bars represent the statistical errors. The shaded band displays the statistical errors of Markus Wobisch. A dashed line is drawn at -5%. With this line the dots should be compared since the results of Markus Wobisch refer to a hadron level with a running electromagnetic coupling constant α whereas the results of the author have been obtained with α fixed.

used. This section refers only to the results obtained with the longitudinally invariant k_t-algorithm. An analysis with these selection criteria (without systematic studies) was performed. The cleaning cuts were those described in Chapter 5 with the only exception that instead of requiring $E_{t,Lab} > 2.5$ GeV the cut $E_{Lab} > 4$ GeV was applied (as was done in the analysis of Markus Wobisch), where E_{Lab} denotes the energy of a jet in the Laboratory frame. The conclusion of the publications cited above was that NLO QCD, as calculated by DISENT with $\mu_r = E_{t,Breit}$, gives a good description of the measured data. The aim is to check the results of H1.

In Fig. 7.11 the ratio (Data - Theory)/Theory is shown for the inclusive double differential jet cross sections $d\sigma/dE_{t,Breit}dQ^2$. The theoretical values were calculated with DISENT with $\mu_r = E_{t,Breit}$. For the central values 16 million events have been generated and analysed. For $\mu_r = E_{t,Breit}/2$ and $\mu_r = E_{t,Breit} * 2$ 8 million events were produced. The error bars in Fig. 7.11 represent the statistical error. The shaded band displays the theoretical error including the uncertainty of the hadronization correction. As can be seen from this figure, the measured cross sections agree fairly well with the results of NLO QCD. The only exception may be the lowest $E_{t,Breit}$-bin for $300 < Q^2 < 600$ GeV^2 where the data is about $2\sigma^{stat}$ away from the upper theory curve (Here σ^{stat} denotes the statistical error.). However, this may be caused by a statistical fluctuation.

Fig. 7.12 shows the comparison between the measured data of the author and the measured data of Markus Wobisch for the inclusive double differential jet cross sections $d\sigma/dE_{t,Breit}dQ^2$. The error bars represent the statistical error of the author. The shaded band displays the statistical error of Markus Wobisch. A dashed line marks the -5%-level to which the points should be compared to, since the values Markus Wobisch published in his thesis referred to a hadron level with a running electromagnetic coupling constant α whereas the values of the author have been obtained with α fixed. It can be seen from this figure that the analyses agree within the statistical errors.

So the conclusion of this section is that the experimental and theoretical results of H1 for inclusive jet cross sections can be reproduced within the statistical errors. (There is a slight difference between Fig. 7.11 and Fig. 7.12 in the binning. Whereas the bin boundaries in Fig. 7.11 are $E_{t,Breit} = 7, 11, 19, 30, 50$ GeV, in Fig. 7.12 they are $E_{t,Breit} = 7, 11, 18, 30, 50$ GeV.)

Conclusion

An analysis has been performed with the ZEUS data of the years 1996 and 1997 corresponding to an integrated luminosity of about 38.6 pb^{-1}. A very large range of Q^2 was examined and the jet selection was performed completely in the Breit frame. Events were taken into account in a Q^2-range from 125 GeV^2 up to $2 \cdot 10^4$ GeV^2 typically with $-0.7 < \cos\gamma < 0.5$. Only jets have been accepted with $E_{t,Breit} > 8$ GeV and $-2 < \eta^{Breit} < 1.8$.

A detailed view on the hadronic final state in deep inelastic positron-proton scattering was given by the measurement of the inclusive differential jet cross sections $d\sigma/dQ^2$, $d\sigma/dE_{t,Breit}$, $d\sigma/d\eta^{Breit}$, $d\sigma/d\phi^{Breit}$ and $d\sigma/d\eta^{Lab}$. Furthermore, $d\sigma/dE_{t,Breit}$ has been determined for six different regions of Q^2.

The validity of NLO QCD was tested. It turned out that for high values of Q^2 ($Q^2 > 500$ GeV^2) and large values of $E_{t,Breit}$ ($E_{t,Breit} > 14$ GeV) the agreement between data and NLO QCD calculations is good. At low Q^2 and small values of $E_{t,Breit}$ the measurements are slightly above the theoretical predictions by about 10%. The signaficance of these deviations is not high due to systematic experimental and theoretical uncertainties. The reduction of these errors is however beyond the scope of this thesis.

Since the jet selection was done completely in the Breit frame, it was possible to measure an azimuthal asymmetry mainly arising from boson-gluon fusion. The influence of events with more than two jets can be neglected, since their relative frequency was about 1%. The measured $d\sigma/d\phi^{Breit}$ displays peaks at $\phi^{Breit} \sim 0°$ and 180°. The shape of this distribution is well reproduced by NLO QCD. It is the first time that such an azimuthal asymmetry has been observed with jets.

Several values of α_s have been determined from the various bins of $d\sigma/dQ^2$ and $d\sigma/dE_{t,Breit}$. A χ^2 fit has been performed to combine these values. For

$Q^2 > 500$ GeV^2 the value and its errors are

$$\alpha_s(M_Z) = 0.1194 \pm 0.0023(stat.)^{+0.0061}_{-0.0045}(exp.)^{+0.0036}_{-0.0006}(th.).$$

This value is in agreement with the world average. Its uncertainties are compatible to those of other methods. It is the first time at ZEUS that α_s has been determined from inclusive jet production.

An additional analysis was performed to check the results of H1 for the inclusive double differential jet cross sections $d^2\sigma/dE_{t,Breit}dQ^2$. Their results were confirmed within the statistical errors.

Bibliography

[1] ZEUS Collaboration, The ZEUS Detector, Status Report 1993, Editor: U. Holm, DESY, Hamburg, Februar 1993

[2] S. Eisenhardt, Measurement of the Strong Coupling Constant α_S form Jet Rates Using the $K_\perp$ Jet Algorithm at ZEUS, DESY-THESIS-1998-038

[3] Henning Raach, Akzeptanzausdehnung des ZEUS-Detektors für diffraktive Streuung, Diplomarbeit, Universität Freiburg (1996)

[4] U. Wollmer, Measurement of Event Shape Variables in Deep Ineleastic ep Scattering with the ZEUS Detector at HERA and a Study of Power Corrections, DESY-THESIS-2000-007

[5] Jürgen Krüger, The Uranium Scintillator Calorimeter for the ZEUS Detector at the Electron-Proton Collider HERA, Habilitationsschrift, Universität Hamburg (1992)

[6] Gabriele Theisen, Untersuchung der hadronischen Schauerentwicklungen im ZEUS-Urankalorimeter, Dissertation, Universität Freiburg (1993)

[7] Claus Grupen, Teilchendetektoren, BI-Wissenschaftsverlag, 1993

[8] Richard Wigmans, Nuclear Instruments and Methods in Physics Research A259 (1987) 389-429

[9] G. Wolf, First Results from HERA, DESY 92-190

[10] Stan Bentvelsen, Optimal use of kinematical variables for x-Q^2 reconstruction in hard NC events, ZEUS-Note 91-14

[11] H. Abramowicz, A. Caldwell, HERA Collider Physics, DESY 98-192

[12] R.K. Ellis, W.J. Stirling and B.R. Webber, QCD and Collider Physics, Cambridge University Press, 1996

[13] Donald H. Perkins, Hochenergiephysik, Addison-Wesley, 1991

[14] Vernon D. Barger, Roger J.N. Phillips, Collider Physics (updated edition), Perseus Books, 1991

[15] R.G. Roberts, The structure of the proton, Cambridge University Press, 1990

[16] R.E. Taylor, Rev. Mod. Phys. 63 (1991) 573;
H.W. Kendall, Rev. Mod. Phys. 63 (1991) 597;
J.I. Friedman, Rev. Mod. Phys. 63 (1991) 615.

[17] S.L. Wu, Phys. Rep. 107 (1984) 59

[18] E. Rizvi, T. Sloan, $xF_3^{\gamma Z}$ in Charged Lepton Scattering, DESY 00-188, December 2000

[19] Yu. L. Dokshitzer, Sov. Phys. JETP 46 (1977) 641;
V.N. Gribov and L.N. Lipatov, Sov. J. Nucl. Phys. 15 (1972) 438 and 675;
G. Altarelli and G. Parisi, Nucl. Phys. 126 (1977) 297.

[20] S. Catani, Yu.L. Dokshitzer, M.H. Seymour and B.R. Webber, Nucl. Phys. B406 (1993) 187

[21] S.D. Ellis and D.E. Soper, Phys. Rev. D48 (1993) 3160

[22] M. Wobisch, T. Wengler, Hadronization Corrections to Jet Cross Sections in Deep-Inelastic Scattering, hep-ph/9907280

[23] B.R. Webber, J. Phys. G19 (1993) 1567

[24] H. Georgi and H.D. Politzer, Phys. Rev. Lett. 70 (1978) 3

[25] W. Buchmüller/G. Ingelman (Editors), Physics at HERA, Proceedings of the Workshop, Vol. 1 (1991)

[26] ZEUS Collaboration, Measurement of Azimuthal Asymmetries in Deep Inelastic Scattering, DESY 00-040, hep-ex/0003017, March 2000

[27] J. Chay et al., Phys. Rev. D45 (1992) 46,
J. Chay et al., Phys. Lett. B269 (1991) 175.

[28] E. Mirkes and S. Willfahrt, Phys. Lett. B414 (1997) 205

[29] Michael Kuhlen, QCD and the Hadronic Final State in Deep Inelastic Scattering at HERA, hep-ph/9712505

[30] G. Marchesini and B.R. Webber, Nuclear Physics B310 (1988) 461-526

[31] G. Gustafson, Phys. Lett. B175 (1986) 453,
Gösta Gustafson and Ulf Petterson, Nucl. Phys. B306 (1988) 746-758,
B. Andersson, G. Gustafson, L. Lönnblad, U. Petterson, Z. Phys. C43 (1989) 625-632.

[32] Leif Lönnblad, Comput. Phys. Commun. 71 (1992) 15

[33] Leif Lönnblad, Ariadne version 4 (Revision 10), December 1997, available on WWW: `http://www.thep.lu.se/~leif/`

[34] Leif Lönnblad, The Color Dipole Model and the Ariadne Program at High Q**2, hep-ph/9908368

[35] M. Riveline, Probing the Parton Evolution in DIS at Low X_{BJ} Using Jet Observables, DESY-THESIS-1999-005, February 1999

[36] B. Andersson, G. Gustafson, G. Ingelman and T. Sjöstrand, Phys. Rep. 97 (1983) 33

[37] G. Marchesini et al., Computer Phys. Commun. 67 (1992) 465

[38] Torbjörn Sjöstrand, International Journal of Modern Physics A. Vol. 3. No. 4 (1988) 751-823

[39] H. Spiesberger, HERACLES and DJANGOH, April 1998, available on WWW: `http://www.desy.de/~hspiesb`

[40] K. Charchula, G.A. Schuler and H. Spiesberger, Comp. Phys. Comm. 81 (1994) 381

[41] W. Buchmüller/G. Ingelman (Editors), Physics at HERA, Proceedings of the Workshop, Vol. 3 (1991)

[42] K. Kwiatkowski, H. Spiesberger and H.-J. Möhring, Comp. Phys. Comm. 69 (1992) 155

[43] G. Ingelman, A. Edin and J. Rathsman, LEPTO 6.5, DESY 96-057

[44] R. Brun et al., GEANT program manual, CERN program library (1992)

[45] T. Sjöstrand, Comp. Phys. Comm. 39 (1986) 347;
T. Sjöstrand and M. Bengtsson, Comp. Phys. Comm. 43 (1987) 367.

[46] Erwin Mirkes, Theory of Jets in Deep Inelastic Scattering, Habilitationsschrift, Universität Karlsruhe, 1997, hep-ph/9711224

[47] Future Physics at HERA, Proceedings of the Workshop 1995/96, Edited by G. Ingelman, A. De Roeck, R. Klanner, Volume 1

[48] S. Catani and M.H. Seymour, Nucl. Phys. B485 (1997) 291

[49] C. Duprel, Th. Hadig, N. Kauer, M. Wobisch, hep-ph/9910448

[50] D. Graudenz, hep-ph/9710244

[51] Thomas M. Trefzger, Messung der Kopplungskonstanten α_S der starken Wechselwirkung aus Jetraten in der tiefinelastischen ep-Streuung bei HERA, Dissertation, Universität Freiburg, 1996

[52] Olaf Christian Ruske, Measurement and Phenomenology of the Proton Structure Function F_2 using the 1996 and 1997 ZEUS Data at HERA, Ph.D. Thesis, University of Oxford, Trinity Term 2000

[53] H. Abramowicz, A. Caldwell, R. Sinkus, Nucl. Instrum. Methods, A365 (1995) 508;
R. Sinkus, T. Voss, Nucl. Instrum. Methods, A391 (1997) 360.

[54] ZEUS Collaboration, Inclusive Jet Cross Sections in Neutral Current DIS in the Breit Frame, submitted to the XXXth International Conference on High Energy Physics, 2000, Osaka, Japan, paper 890

[55] ZEUS Collaboration, Measurement of Dijet Production in Neutral Current Deep Inelastic Scattering at High Q^2 and Determination of α_s, DESY 01-018, hep-ex/0102042, February 2001

[56] S. Bethke, J. Phys. G26 (2000) R27

[57] Particle Data Group, D.E. Groom et al., Eur. Phys. J. C15 (2000) 1

[58] Markus Wobisch, Measurement and QCD Analysis of Jet Cross Sections in Deep-Inelastic Positron-Proton Collisions at $\sqrt{s}$ = 300 GeV, DESY-THESIS-2000-049, November 2000

[59] H1 Collaboration, Determination of the Strong Coupling Constant from Inclusive Jet Cross Sections in Deep-Inelastic Positron-Proton Collisions at HERA, submitted to EPS-HEP99, Tampere, paper 157

[60] H1 Collaboration, Measurement and QCD Analysis of Jet Cross Sections in Deep-Inelastic Positron-Proton Collisions at $\sqrt{s}$ = 300 GeV, DESY 00-145, October 2000

[61] W. Buchmüller/G. Ingelman (Editors), Physics at HERA, Proceedings of the Workshop, Vol. 2 (1991)

Acknowledgments

I would like to express my gratitude to my supervisor Professor Dr. Andreas Bamberger for the topic of this thesis and his guidance and support all along my time as Ph.D. student. I am also grateful to the postdocs of our group, Sabine Wölfle and Nicola Coppola for their valuable support and continuous discussion. I would like to address all members of the group, former and present, and thank them for the pleasant and supporting atmosphere.

Thanks also to the physics coordinators Juan Terron and Matthew Wing for their encouragements. At the final stage of the preparation of this work Matthew Wing and Nicola Coppola added useful suggestions for content and appearance. I am very grateful to Oscar Gonzalez, who did an independent second analysis, for the excellent cooperation and to my fellow analysers Enrico Tassi and Doug Chapin for their expertise.

Many thanks to DESY who supported me for five months with a Ph.D. fellowship.

Finally, my deepest gratitude to my parents Ursula and Ernst Raach and my grandmother Elisabeth Schreiner for their constant support throughout my studies.